Title
Magnetic Proximity Effect and Spin Transport in Heterostructures of Two-Dimensional Ferromagnets

Permalink
https://escholarship.org/uc/item/8150t7tk

Author
Lohmann, Mark Ian

Publication Date
2020

Peer reviewed|Thesis/dissertation

UNIVERSITY OF CALIFORNIA
RIVERSIDE

Magnetic Proximity Effect and Spin Transport in Heterostructures of Two-Dimensional
Ferromagnets

A Dissertation submitted in partial satisfaction
of the requirements for the degree of

Doctor of Philosophy

in

Physics

by

Mark Ian Lohmann

March 2020

Dissertation Committee:
        Dr. Jing Shi, Chairperson
        Dr. Nathaniel Gabor
        Dr. Yongtao Cui

The Dissertation of Mark Ian Lohmann is approved:

_____

_____

_____

<div align="right">Committee Chairperson</div>

University of California, Riverside

Acknowledgements

As I reach the pinnacle of my nearly 6-year journey to successfully earn my PhD in physics, I am filled with an overwhelming sense joy accompanied by a touch of sadness. I am joyful to be jumping into the next chapter of my life with a solid set of skills both learned and earned throughout the time I've spent in this program which will serve as a guide to success in all my future endeavors. At the same time, I will be moving on from a place that I have dedicated a large part of myself which leaves me with a small amount of sadness to leave such a wonderful collaborative environment. I am filled with gratitude for the department of physics at UC Riverside for giving me this opportunity to earn my PhD with them.

I would first off like to acknowledge my PhD advisor Dr. Jing Shi. His unwavering support and insightful wisdom throughout these years enabled me to reach above and beyond the goals I had set for myself. He was always available, day or night, to provide me guidance in my research and to make sure that I had all the resources I needed for success. Even beyond his support with my research and studies, he was always understanding of my need to spend time with my wife and children while also being successful with my academic goals. Thank you, Dr. Shi, for being a great mentor and for providing me with invaluable advice in both my research and life.

I wish to acknowledge the members of my thesis committee, Dr. Nathaniel Gabor and Dr. Yong-Tao Cui, for their insightful and positive comments on my research projects and dissertation. I have learned a lot and grown as a researcher through the collaborative

Last, but not least, I want to thank my wife Katy Bales Lohmann and my children Jack Alan Lohmann and Maxwell Alexander Lohmann. The love and support I received from you guys throughout my time at UCR motivated me to push myself as hard as I possibly could. I could have never got to this point with you guys behind me and I appreciate all of the sacrifices that you have made. Being the best husband and father as I can possibly be is my number one goal in life and I am grateful that I have the best wife and children to help me along as I worked to achieve my second highest goal: earning my PhD in physics.

Acknowledgement of previously published material

ABSTRACT OF THE DISSERTATION

Magnetic Proximity Effect and Spin Transport in Heterostructures of Two-Dimensional
Ferromagnets

by

Mark Ian Lohmann

Doctor of Philosophy, Graduate Program in Physics
University of California, Riverside, March 2020
Dr. Jing Shi, Chairperson

Utilizing van der Waals layered 2D ferromagnetic materials in spintronic devices
has become very attractive to the field as they offer the promise of a better understanding
of the underlying physical mechanisms involved in such systems. Also, the techniques
widely used in the field of spintronics offers the ability to probe the magnetic state of these
material.

The first chapter of this dissertation is an introduction to van der Waals layered
magnetic materials and spintronics with a focus on recent advances in the field of two-
dimensional spintronics.

The second chapter is a summary of the work I have done to understand the
magnetic state of CGT thin flakes by a proximity effect which allows us to use electronic
transport in a thin layer of platinum deposited on CGT's surface to probe the magnetism in

the highly insulating ferromagnetic semiconductor. This includes an unsuccessful attempt to induce magnetism in graphene sheets coupled to CGT.

The third chapter summarizes the work I have done to understand the spin-orbit torque exerted on the magnetization of thin flakes of FGT in heterostructures with platinum as the source of the injected spin current. This is

The final chapter summarizes the study I performed to gain a better understanding of the frustrated anti-ferromagnetism and search for transport signature of the quantum spin liquid state of $RuCl_3$ in $RuCl_3/Pt$ heterostructures through magneto-transport measurements. From the work presented in this dissertation it is clear that coupling 2D magnetic materials to heavy metals such as Pt is a valuable tool to probe and utilize this very interesting family of 2D materials.

Contents

List of Figures

Chapter 1 Introduction

1.1 Van der Waals Magnetic Materials

In 2004, Andre Geim and Konstantin Novoselov successfully isolated graphite into single atomic layer flakes of graphene and measured its electronic transport properties in the first ever experiment to measure the properties of truly two-dimensional material [1]. Due to its profound impact on the field of condensed matter physics their work earned them the Nobel prize in physics a mere 6 years after its publication. This spawned a new sub-field which is now the largest sub-field in condensed matter physics with numerous materials from superconductors to insulators including the materials which are the focus of this dissertation, two-dimensional magnetic materials.

Long-range ferromagnetic order was previously thought to be suppressed in a single atomic layer ferromagnet due to the large thermal fluctuations in dimensions, $d \leq 2$ as predicted by the Mermin-Wagner theorem. In 2017, this assumption was experimentally put to the test in two independent studies of the magnetic state of the van der Waals ferromagnetic semiconductors, $Cr_2Ge_2Te_6$ (CGT) and CrI_3, in the two-dimensional limit, by C. Gong, et al. and B. Huang, et al. respectively [2,3].

Since then there has been a lot of work done to understand the mechanisms responsible for the magnetism in these layered ferromagnets and how it evolves down to the single layer limit as well as to search for other layered materials which have magnetic ordering which persists in a single layer. There now exists a plethora of materials known to exhibit both ferromagnetic and anti-ferromagnetic ordering in two-dimensions. This

family of van der Waals magnets includes but is not limited to insulators such as $RuCl_3$, semiconductors such as CGT and CrI_3, metals such as Fe_3GeTe_2 (FGT), and even topological insulators such as $MnBi_2Te_4$.

These materials have opened the door to studying interesting physical phenomena that would be otherwise inaccessible in thin film magnets. For instance, FGT, a layered ferromagnetic metal, can be cleaved down to the single layer with precise control over the number of layers allowing for an understanding of how its ferromagnetic ordering decreases with reduced thickness which would be impossible to do in grown ferromagnets due to the inability to control the growth to single layers [4]. Another example is CrI_3 where a study of its magnetic ordering as a function of the number of layers reveals very interesting alternating ferromagnetism and anti-ferromagnetism dependent upon whether the number of layers is odd or even respectively [3].

This family of layered van der Waals magnetic materials in conjunction with the nearly infinite number of their non-magnetic partners are opening up opportunities for the study of novel physical phenomena and the interactions from which they arise by having control over how each layer is stacked with respect to the other as with the superconductivity and ferromagnetic ordering which can be acquired in twisted bilayer graphene at specific twist angles [5]. Such materials are also useful for forming van der Waals heterostructures with other nonmagnetic 2D as well as ordinary bulk materials for spintronics applications.

1.2   Hall Effect

1.2.1   Ordinary Hall Effect.

In his groundbreaking paper in 1879, Edwin Hall showed that when current flows through a device subject to a perpendicular magnetic field, it acquires a potential difference transverse to both the current and the applied magnetic field as illustrated in figure 1.1 (a) [6]. The Hall effect, as it was coined, is due to the Lorentz force which acts upon the charge carriers in the device deflecting them to the edges causing a net charge to accumulate. This gives rise to the transverse voltage, which is proportional to the strength of the applied magnetic field, the magnitude of the current which flows in the device, and the density of charge carriers. The sign of the Hall effect depends on the type of charge carriers responsible for the current flow which makes it an important tool for the determination of the type of carrier responsible transport in solid-state electronics.
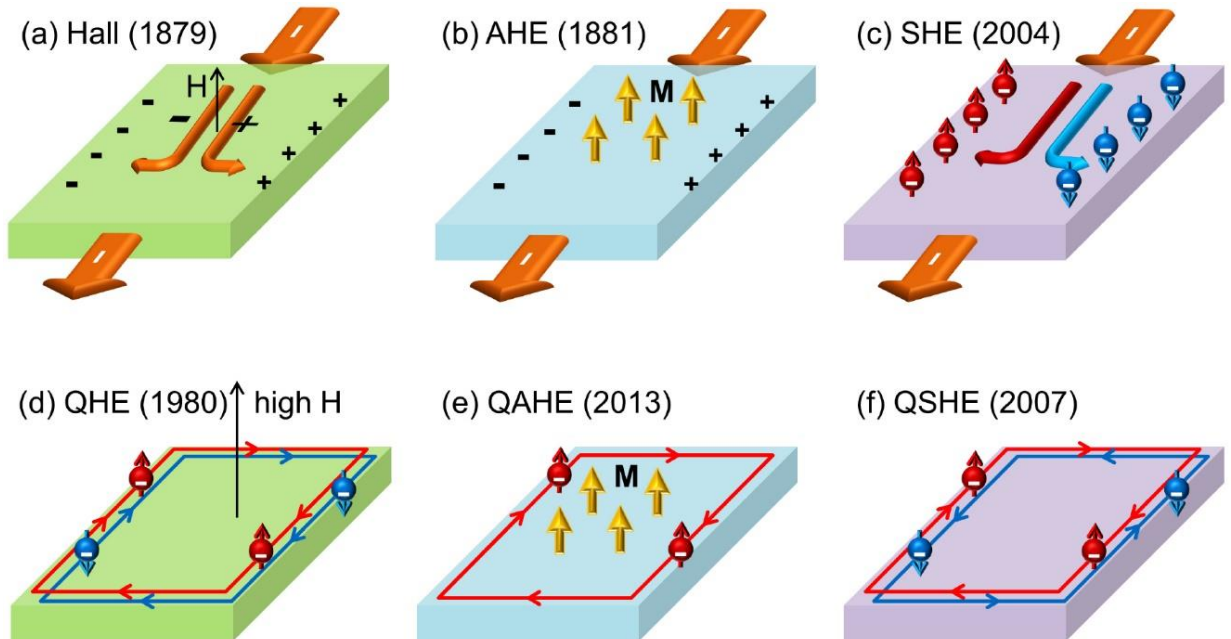
Figure 1.1. Hall Effects. (a) Ordinary Hall effect. (b) Anomalous Hall effect. (c) Spin Hall effect. (d) Quantum Hall effect. (e) Quantum anomalous Hall effect. (f) Quantum spin Hall effect. H and M denote the magnetic field and magnetization respectively. Adapted from C. -Z. Chang, J Phys-Condens Mat **28**, (2016).

1.2.2   Quantum Hall Effect

Throughout the more than a century since Hall's groundbreaking discovery, a lot of research has been undertaken to understand how the Hall effect manifests itself in different solid-state systems. One important case is the quantum Hall effect which occurs in two-dimensional systems including bulk materials in which the electrons are confined to motion in just two dimensions and subjected to large perpendicular magnetic fields. This integer Quantum Hall effect was first discovered Kiltzing in 1980, in the degenerate electron gas system at the inversion layer of a Si/SiO_2 MOSFET [7].

In such two-dimensional systems, the charge carriers, when subjected to a perpendicular magnetic field, move in cyclotron orbits which are circular due the electrons

confinement to a single plane of motion. Classically these orbits are defined by the strength of the applied field and oscillate with the frequency, $\omega_C = \frac{qB}{m}$, known as the cyclotron frequency in which any orbit is available from the continuous energy spectrum. In quantum mechanics the energy is quantized into discrete values known as the Landau levels, $E_n = \hbar\omega_C(n + \frac{1}{2})$, of the system where the cyclotron frequency defines the magnitude of the quantized levels. When the Fermi energy of the system takes on values in between any two of the Landau levels, which can be achieved either by tuning the Fermi energy via electrostatic gating or by increasing the field which increases the gap between discrete energy levels, the carriers in the bulk of the system undergo Anderson localization causing the longitudinal resistivity to go to zero while the carriers at the edges of the system are free to flow leading to a quantized transverse resistivity. While the quantum Hall effect (QHE) described above is valid for Landau levels with integer values of n, it was also determined experimentally that the value of, n, does not necessarily need to take on an integer value and can actually come in fractions of an integer in what is known as the fractional quantum Hall effect which along with the integer QHE is depicted in figure 1.2 [8].

Figure 1.2. Integer and Fractional Quantum Hall Effect. Low temperature longitudinal and transverse resistivity from a two-dimensional electron gas system revealing both the integer and fractional quantum Hall effect by the minima in longitudinal resistivity which correspond to the plateaus in the Hall resistivity. Adapted from H.L. Stormer, Physica B 177, 401 (1992).

1.2.3   Anomalous Hall and Quantum Anomalous Hall Effects

Roughly two years after publication of Hall's seminal work describing the ordinary Hall effect (OHE), he performed a similar experiment except in this case he ran a current through a ferromagnetic metal. The results were surprising as he noticed that the Hall effect measured in the ferromagnetic metals cobalt, iron, and nickel was much larger than the effect measured in non-magnetic metals [8]. Also when Hall increased the magnetic field

applied in the system he observed an anomaly in its response where the signal deviated from its expected linear response and, in one of the sample he presented, the signal seemed to saturate as the field was raised above a critical value. Since then the anomalous Hall effect (AHE), as it was coined, has served as one of many indispensable tools in the study of magnetism allowing the magnetic properties to be studied through electronic transport experiments.

While the theoretical underpinnings of the ordinary Hall effect were well understood when Hall's original findings were published, a theoretical understanding of the AHE evaded and perplexed physicists for nearly a century after Hall's 1881 work. In the 1930's an important link between the magnetization of a ferromagnet and the anomalous Hall resistivity was experimentally determined and given by the relationship, $\rho_{yx} = R_0 H_z + R_s M_z$, where, $R_0 H_z$, is the ordinary Hall effect contribution and, $R_s M_z$, is the additional contribution given by the AHE [10,11]. Although this was a helpful insight into the role that a material's magnetic properties play in the AHE, several concepts were still required to understand the underlying physical mechanisms. Most importantly the Berry-phase and Berry-phase curvature were not completely understood until the 1980's [12]. Even that was not enough to give a full understanding of the AHE as this only describes the intrinsic contribution to the anomalous Hall resistivity. There are also several extrinsic contributions that determine the anomalous Hall resistivity in different materials such as the skew scattering mechanism which arises from impurity scattering caused by the spin-orbit interaction and side jump from quasi-particles which scatter from spin-orbit coupled impurities [12]. The intrinsic as well as the two extrinsic mechanisms are

illustrated in figure 1.3. In next two chapters of this dissertation the AHE is used to study

magnetic proximity effects non-magnetic platinum thin films coupled to the insulating two-

dimensional ferromagnet $Cr_2Ge_2Te_6$ and as a probe of the magnetization in Fe_3GeTe_2 as it

is switched by current driven spin orbit torques.
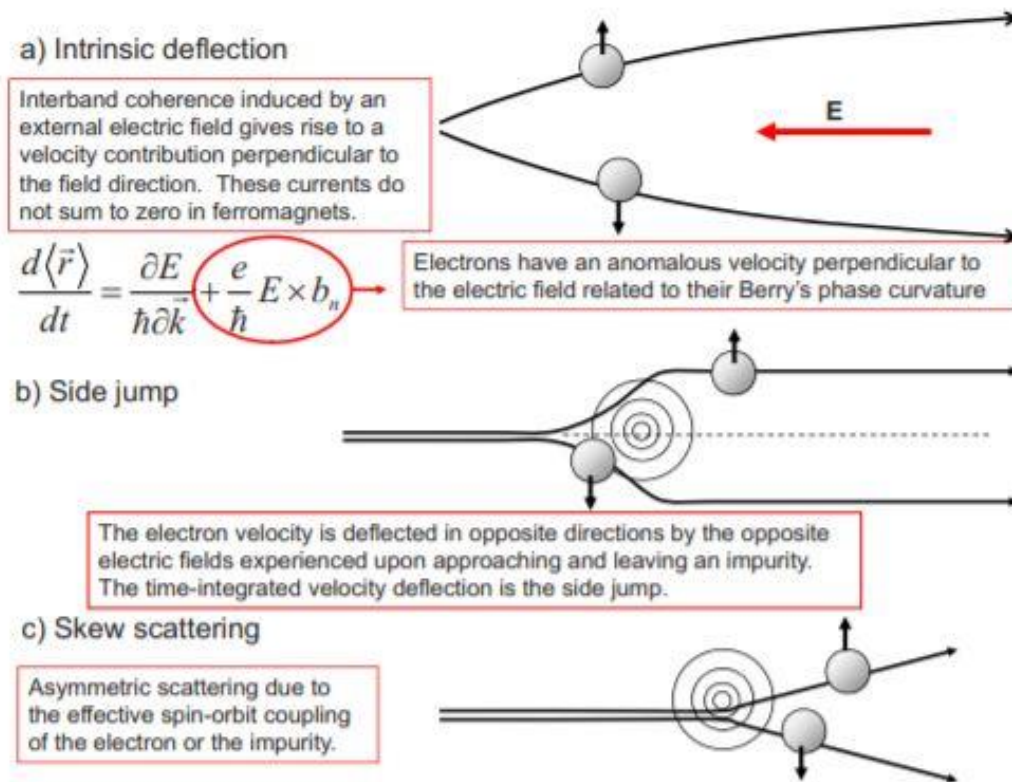
Figure 1.3. Mechanisms of the AHE. The three mechanisms which together give rise to the AHE. (a) The intrinsic contribution. (b) The extrinsic side jump contribution. (c) The extrinsic side jump mechanism. Adapted from Nagaosa, N., Sinova, J., Onoda, S., MacDonald, A. H. & Ong, N. P. Anomalous Hall effect. *Rev. Mod. Phys.* **82**, 1539–1592 (2010).

In ferromagnetically ordered two-dimensional electron systems an interesting state of matter, which is characterized by a quantized value of the anomalous Hall resistivity known as the quantized anomalous Hall effect (QAHE), is possible to be realized [13,14]. The broken time-reversal symmetry that the ferromagnetism offers in conjunction with strong spin-orbit coupling will lead to a small topological gap in the band structure and when the Fermi level sits in the gap this state will be present.

1.2.4   Spin Hall and Quantum Spin Hall Effect.

The last of the known incarnations of the Hall effect, central to the field of modern spintronics and plays a prominent roll throughout the third chapter of this dissertation, the spin Hall effect (SHE) was first predicted in 1971 and experimentally realized through Kerr rotation measurements in 2004. When a current is passed through a material with large spin orbit coupling (SOC) the charges will be deflected to its edges with the direction of the deflection determined by its spin state. In such a situation the charge distribution along the edges of the material will be equal on both sides so a transverse chargevoltage will not be present, but an accumulation of charges with opposite spin states will occur and thus a net spin chemical potential will generate a pure spin current transverse to the direction of the injected charge current [17]. Using the Onsager reciprocity relationship, the opposite of this effect, the inverse spin Hall effect (ISHE) is revealed. This effect, which also requires a material with strong SOC to take place, is where a pure spin current injected into a material generates a transverse charge current which can be easily detected via a measurement of the Hall potential.

A major difference between the SHE and the other Hall effects presented previously is that the SHE/ISHE do not require an external magnetic field in order to generate the effect. One caveat to the last statement is that the AHE and QAHE can give a transverse current in the absence of an external magnetic field provided that the ferromagnet used to detect the effect has perpendicular magnetic anisotropy (PMA) in which the z-component of the magnetization is always non-zero without the application of some kind of perturbation to force it to be exactly zero.

As is the case with the OHE and AHE, there is also a quantized version of the SHE. The quantum spin Hall effect (QSHE), was originally theorized in graphene although a large SOC would need to be induced into graphene for this effect to occur as its intrinsic SOC is orders of magnitude smaller than what would be required [18]. To date, no experiment has been able to realize the QSHE in graphene although many attempts have been made and continue to this day. Regardless of the lack of the QSHE in graphene this effect has been experimentally verified in different material systems such as HgTe quantum wells, where it was first realized, as well as the two-dimensional transition metal dichalcogenide (TMD) WTe_2 [19,20].

An important consequence of the quantized versions of the three Hall effects has to do with the nature of the current that is generated in the edges of the material as depicted in figures 1.1d, 1.1e, and 1.1f. In the case of the QHE and QSHE the contain counter propagating edge currents whose chirality is determine by the spin state of the carrier while the carries in the bulk are localized and do not contribute to the electronic transport. The situation is similar with regards to the QAHE although the broken time-reversal symmetry

provides just a single spin state available to the carriers in the material and thus the edge current flows free of dissipation by the fact that backscattering would require a spin flip which would be energetically unfavorable.

1.3   Overview of Spintronics

The field of spin electronics commonly referred to as spintronics is a relatively new subfield within condensed matter physics. Although this field of study can be traced back to the work of Mott in the 1930's when he described the phenomena of spin-polarized transport as he sought to explain the unusual magnetoresistance (MR) which was observed in ferromagnetic metals and expanded upon in the late 1960's with tunneling MR (TMR) measurements in N/F/N tunnel junction where N is a normal metal and F a ferromagnetic semiconductor/insulator, it really gained its own place within the larger field of condensed matter physics in the 1980's with the discovery of giant magnetoresistance (GMR) in F/N/F heterostructures and the implementation of these effects into practical applications, some of which are still used in modern electronics such as magnetoresistive random-access memory (MRAM) [21].

Since then the field has blossomed and many technologies have been proposed that could revolutionize the performance of modern electronics such as the spin field effect transistor (FET) proposed by Datta and Das which would utilize the two-degrees of freedom available from the electron spin to encode information which in theory can perform read/write operations without the necessity charge current or any pre-amplifiers as is the case in the current semiconductor based FETs [22]. The overall promise of the

field of spintronics, that has yet to be realized, is the complete replacement of all electronic devices which are currently dependent upon the transportation of charges with new technologies which rely on the transportation of information via the spin of localized carriers removing the parasitic contributions of charge transport such as Joule heating and tunneling of charges through the gaps that separate the different components in such devices as the components a packed closer together to make the devices smaller without sacrificing their performance capabilities.

1.3.1   Magnetism and SOC Induced Through Proximity Effects.

Proximity effects are attractive to the field of condensed matter physics as they allow for the realization of interesting physics in heterostructures of materials with properties that are very different from one another. For instance, a normal non-superconducting metal can become superconducting when formed into a heterostructure with a superconductor (SC) although the critical temperature at which its superconducting transition occurs will be lower in the normal metal layer than it is in the SC, also ferromagnetism and SOC can be induced into a material which lacks such properties when formed into heterostructures [23-25].

Predictions of very interesting physical states such as the QSHE and QAHE in single layer graphene have yet to be realized due to its intrinsically small SOC. Many attempts have been undertaken to realize these states in graphene. Most attempts which have be successful in enhancing the SOC in graphene have done so by hybridizing graphene with light adatoms such that its sp^2 carbon-carbon bonds reorganize into sp^3

carbon-adatom bonds [26]. This method has one major pitfall in that other important properties of the graphene such as its exceptionally high mobility amongst others are destroyed by the presence of the adatoms. The most promising of these attempts is through proximity induced SOC in heterostructures of graphene with other high SOC two-dimensional materials such as the TMD's WSe_2, WS_2, and MoS_2 [25,27]. Unlike the adatom absorption approach, this method preserves graphene's Dirac cone dispersion as well as its other desirable electronic transport properties while inducing SOC in graphene up to three orders of magnitude above its intrinsic value [28].

To realize the QAHE in graphene it is necessary that not only its SOC must be enhanced but also that it must somehow obtain ferromagnetic ordering which it lacks in its pristine form. The most promising way to achieve this goal is through the heterostructure approach. Using this approach, it has been shown that magnetic ordering can be induce into graphene which was demonstrated through AHE measurements in heterostructures with the magnetic insulator $Y_3Fe_5O_{12}$ (YIG) although the highest observed value is still only a fraction of the quantized value [29]. This type of magnetic proximity effect has been known about and studied for decades since it was first realized in heterostructures of non-magnetic heavy metals with ferromagnetic metals, but it was believed that the same effect would not be manifest itself in when the ferromagnet in the heterostructure is also an electronic insulator. Even today there is still an ongoing debate within the spintronics community as to whether the AHE realized in heterostructures with ferromagnetic insulators is due to a combination of the SHE and the ISHE or if proximity magnetic exchange coupling is the effect responsible. Also, understanding how such effects manifest

themselves is important to heterostructure based spintronic devices as proximity induced magnetism can be an undesired effect in some measurements such as a one in which the the goal is to study properties which rely on the SHE and ISHE in the device.

1.3.2 Spin Current and Spin-Orbit Torques

In a normal circuit charge is carried by current of either electrons or holes to transport information as well as to give power to electrical devices, but electrons(holes) also possesses another property, its spin angular momentum, which can replace the necessity of charge current, at least for the transportation of information, with a less volatile spin current.

Spin current is transported through solids by two possible mechanism which are spin polarized charge currents or by spin waves. Spin polarized current is the type of spin current that is transported exclusively in conductors as it is accompanied by the flow of charges although it is not necessary that the moving charges generate a flow of charge current. Figure 1.4 illustrates all the possible scenarios in which a flow of spin polarized charge currents can give rise to a flow of spin current in a conductor. The first scenario is just an ordinary spin unpolarized charge current. In this case there is an equal number of the carriers in each of the two possible spin states with all of the charges flowing in the same direction resulting in a net charge current without a net spin current. The next situation is one in which the charges all flow in the same direction, but there exists a net imbalance in the spin states of the carriers and thus a charge current is accompanied by a small spin current. The third case is similar to the one before it except in this case all of the

14

spins are aligned in the same direction and thus the spin current that accompanies this charge current is at its maximum value. The last is a case of a pure spin current without an accompanied charge current flow. In this situation there are equal quantities of carries in both of the spin states, but the direction of their flow is dependent upon the spin state they are in, so the charge current contribution from each of the spin species will cancel out with one another giving no net charge current but the imbalance of spins at each end will give rise to the net spin current flow.
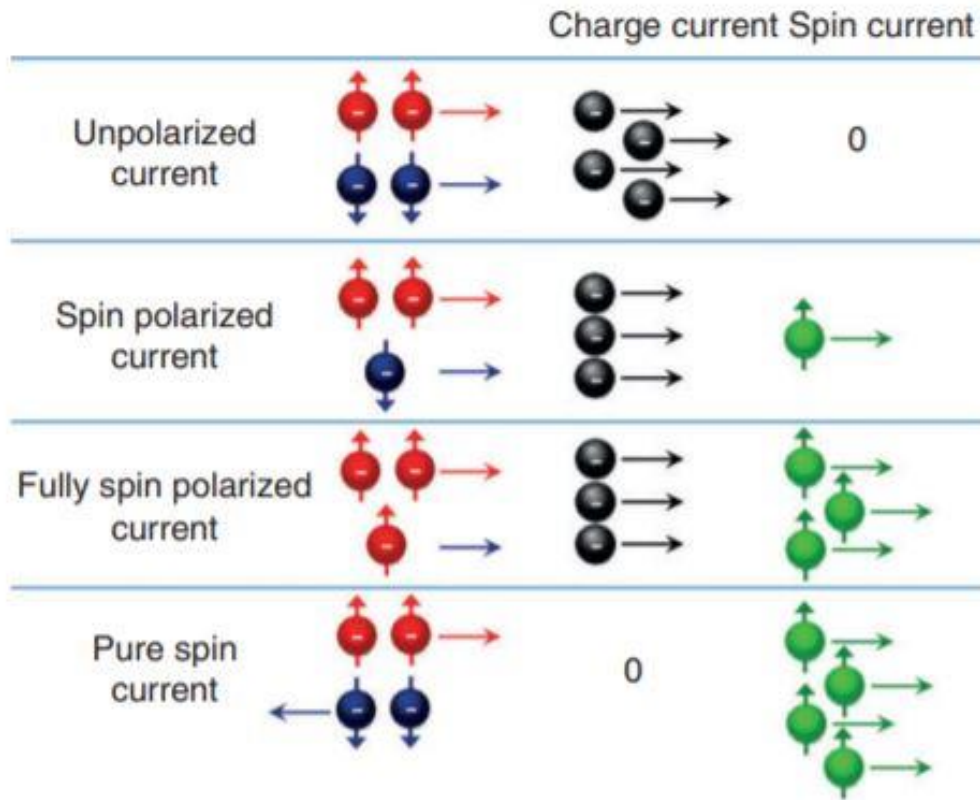
Figure 1.4. Spin Polarized Currents. Illustration of spin polarized current from completely unpolarized current (ordinary charge current) to fully polarized spin current without an accompanying charge current. The first column depicts the overall flow of the charges including the spin state of the carriers. The second column give the charge current in each of the states and the third column represents the spin current from each of the situations. Adapted from Y. P. Feng et al. Prospects of spintronics based on 2D materials. Wiley Interdiscip Rev Comput Mol Sci. 7, 1313 (2017).

Spin waves, the collective excitation of localized spins in a solid, can be excited in all materials which contain magnetic ordering, but as of now only materials with long-range magnetic ordering have been conclusively demonstrated to carry spin current via spin waves although there is some evidence of spin wave mediated spin current transport in one dimensional chains of the quantum spin liquid (QSL) Sr_2CuO_3 through spin Seebeck effect (SSE) measurements [30]. Spin waves are a product of the phase shifted precession

16

of neighboring electrons in a magnetically ordered solid about an external magnetic field, as depicted in figure 1.5, and the spin current of such waves are carried by the Bosonic quasiparticles known as magnons. An exception to this description is spin waves in QSL materials which only contain a short-range magnetic ordering without any long-range ordering down to zero Kelvin. In QSL systems, the spin current is mediated by fractionalized Fermionic excitations known as spinons. An interesting property of spin wave mediated spin current is that its transport is not limited to conducting materials as is the case for spin polarized currents as it propagates via localized electrons in a solid which allows for spin wave mediated spin current in insulators as well.
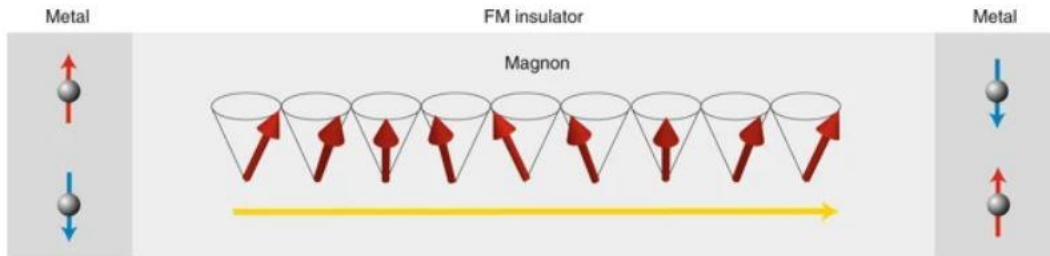
Figure 1.5. Illustration of Spin Wave (Magnon) Mediated Spin Current in a Ferromagnetic Insulator. In such a device the metal on the left end is used to inject spin current into the magnetic material via the SHE and transported through the magnet as a spin wave which is then detected by the meat on the right end via the ISHE. Adapted from Han, W., Maekawa, S. & Xie, X. Spin current as a probe of quantum materials. *Nat. Mater.* **19,** 139–152 (2020).

1.3.3   Antiferromagnetic Spintronics

A relatively new, but an exciting and promising subfield of spintronics, antiferromagnetic spintronics, is a rapidly growing field due to the many benefits that the

use of antiferromagnets (AFMs) as the active elements in spintronic devices has to offer. The frequencies at which AFM materials can switch between their magnetic states are in the terahertz range as opposed to ferromagnetic materials which operate at orders of magnitude low frequencies in the gigahertz range which make AFMs attractive for use in new devices with the potential to operate at ultra-fast speeds [31-33]. Another benefit offered by the use of AFM materials is the robust nature of AFM states to external fields and their ability to be utilized with no effect to other elements nearby due to the fact that they exhibit little to no magnetic moments and thus do not contain any parasitic magnetic fields [31,32].

Over the past several years many experiments have taken place to gain an understanding of the properties of AFM materials and their ability to be implemented in spintronic device structures. Studies have shown that AFM materials have the ability to store information utilizing electrical transport techniques to read and write data through the difference in resistance between their different spin configurations as has been done successfully for decades with the use of ferromagnets [34,35]. Also, recent spin pumping experiments at frequencies near the THz range have brought the field closer to the utilization AFM materials to make devices which rely on pure spin currents without the need of electrical injection [36].

References:

[1]   K. S. Novoselov, A. K. Geim, S. V. Morozov, D. Jiang, Y. Zhang, S. V. Dubonos, I. V. G. and A. A. F. Electric Field Effect in Atomically Thin Carbon Films. **306**, 666–669 (2016).

[2]   Gong, C. *et al.* Discovery of intrinsic ferromagnetism in two-dimensional van der Waals crystals. *Nature* **546**, 265–269 (2017).

[3]   Huang, B. *et al.* Layer-dependent ferromagnetism in a van der Waals crystal down to the monolayer limit. *Nature* **546**, 270–273 (2017).

[4]   Fei, Z. *et al.* Two-dimensional itinerant ferromagnetism in atomically thin Fe3GeTe2. *Nat. Mater.* **17**, 778–782 (2018).

[5]   Yankowitz, M. *et al.* Tuning superconductivity in twisted bilayer graphene. *Science* **363**, 1059–1064 (2019).

[6]   Hall, E. H. On a New Action of the Magnet on Electric Currents. *Am. J. Math.* **2**, 287 (1879).

[7]   Klitzing, K. V., Dorda, G. & Pepper, M. New method for high-accuracy determination of the fine-structure constant based on quantized hall resistance. *Phys. Rev. Lett.* **45**, 494–497 (1980).

[8]   Tsui, D. C., Stormer, H. L. & Gossard, A. C. Two-dimensional magnetotransport in the extreme quantum limit. *Phys. Rev. Lett.* **48**, 1559–1562 (1982).

[9]   Hall, E. H. XVIII. On the "Rotational Coefficient" in nickel and cobalt. *London, Edinburgh, Dublin Philos. Mag. J. Sci.* **12**, 157–172 (1881).

[10]   Pugh, E. M. Hall effect and the magnetic properties of some ferromagnetic materials. *Phys. Rev.* **36**, 1503–1511 (1930).

[11]   E. M. Pugh, T. W. Lippert, Hall emf and Intensity of Magnetization. **1503**, 1–5 (1932).

[12]   Nagaosa, N., Sinova, J., Onoda, S., MacDonald, A. H. & Ong, N. P. Anomalous Hall effect. *Rev. Mod. Phys.* **82**, 1539–1592 (2010).

[13]   Haldane, F. D. M. Model for a quantum hall effect without landau levels: Condensed-matter realization of the 'parity anomaly'. *Phys. Rev. Lett.* **61**, 2015–2018 (1988).

[14]   Chang, C. Z. *et al.* Experimental observation of the quantum anomalous Hall effect in a magnetic topological Insulator. *Science* **340**, 167–170 (2013).

[15]   Dyakonov, M. I. & Perel, V. I. Current-induced spin orientation of electrons in semiconductors. *Phys. Lett. A* **35**, 459–460 (1971).

[16]   Kato, Y. K., Myers, R. C., Gossard, A. C. & Awschalom, D. D. Observation of the spin hall effect in semiconductors. *Science* **306**, 1910–1913 (2004).

[17]   Sinova, J., Valenzuela, S. O., Wunderlich, J., Back, C. H. & Jungwirth, T. Spin Hall effects. *Rev. Mod. Phys.* **87**, 1213–1260 (2015).

[18]   Kane, C. L. & Mele, E. J. Quantum Spin hall effect in graphene. *Phys. Rev. Lett.* **95**, 1–4 (2005).

[19]   König, M., Molenkamp, L. W., Qi, X. & Zhang, S. Quantum Spin Hall Insulator State in HgTe Quantum Wells. *Science* **766**, 766–771 (2010).

[20]   Wu, S. *et al.* Observation of the quantum spin Hall effect up to 100 Kelvin in a monolayer crystal. *Science* **359**, 76–79 (2018).

[21]   Žutić, I., Fabian, J. & Sarma, S. D. Spintronics: Fundamentals and applications. *Rev. Mod. Phys.* **76**, (2004).

[22]   Datta, S. & Das, B. Electronic analog of the electro-optic modulator. *Appl. Phys. Lett.* **56**, 665–667 (1990).

[23]   Meissner, W. & Holm, V. R. Messungen mit Hilfe von flüssigem Helium. XII. *Zeitschrift für Phys.* **66**, 477–489 (1930).

[24]   Hauser, J. J. Magnetic Proximity Effect. *Phys. Rev.* **187**, (1969).

[25]   Yang, B., Lohmann, M. *et al.* Strong electron-hole symmetric Rashba spin-orbit coupling in graphene/monolayer transition metal dichalcogenide heterostructures. *Phys. Rev. B* **96**, 1–5 (2017).

[26]   Castro Neto, A. H. & Guinea, F. Impurity-induced spin-orbit coupling in graphene. *Phys. Rev. Lett.* **103**, 1–4 (2009).

[27]   Wang, Z. *et al.* Strong interface-induced spin-orbit interaction in graphene on WS 2. *Nat. Commun.* **6**, 1–7 (2015).

[28]   Wang, Z. *et al.* Origin and magnitude of 'designer' spin-orbit interaction in graphene on semiconducting transition metal dichalcogenides. *Phys. Rev. X* **6**, 1–15 (2016).

[29]   Tang, C. *et al.* Approaching quantum anomalous Hall effect in proximity-coupled YIG/graphene/h-BN sandwich structure. *APL Mater.* **6**, (2018).

[30]   Hirobe, D. *et al.* One-dimensional spinon spin currents. *Nat. Phys.* **13**, 30–34 (2017).

[31]   Gomonay, E. V. & Loktev, V. M. Spintronics of antiferromagnetic systems. *Low Temp. Phys.* **40**, 17–35 (2014).

[32]   Jungwirth, T., Marti, X., Wadley, P. & Wunderlich, J. Antiferromagnetic spintronics. *Nat. Nanotechnol.* **11**, 231–241 (2016).

[33]   Kampfrath, T. *et al.* Coherent terahertz control of antiferromagnetic spin waves. *Nat. Photonics* **5**, 31–34 (2011).

[34]   Loth, S., Baumann, S., Lutz, C. P., Eigler, D. M. & Heinrich, A. J. Bistability in Atomic-Scale Antiferromagnets. *Science* **335**, 196–200 (2012).

[35]   Wadley, P. *et al.* Spintronics: Electrical switching of an antiferromagnet. *Science* **351**, 587–590 (2016).

[36]   Li, J. *et al.* Spin current from sub-terahertz-generated antiferromagnetic magnons. *Nature* **578**, 70–74 (2020).

Chapter 2   Probing Magnetism in Insulating $Cr_2Ge_2Te_6$ by Induced Anomalous Hall Effect

2.1   Motivation

Understanding the magnetic properties of two-dimensional (2D) van der Waals ferromagnets such as CGT, CrI_3, amongst a plethora of others, has attracted a great deal of interest due to their ability to be exfoliated down to the monolayer allowing for studying magnetism in 2D systems [1,2] as well as their ability to easily form heterostructures with other 2D materials such as graphene and a wide range of transition metal dichalcogenides [3]. In CrI_3, for example, the intriguing interlayer antiferromagnetic coupling is uncovered when a few layers are involved. Recently, large tunneling magnetoresistance between the atomic layers in CrI_3 has revealed rich spin states as a result of the antiferromagnetic coupling [4].

To date, no tunneling experiment has been reported in the other 2D insulating ferromagnet, CGT, to study the magnetic properties such as the interlayer coupling. In conducting ferromagnets, transport measurements such as magnetoresistance and anomalous Hall effect (AHE) are routinely employed to probe the magnetic properties especially in small devices [5,6]. In insulating ferromagnets, however, such transport measurements are not directly applicable. In this study, we explore an alternative way to probe the magnetic properties of thin CGT flakes by electrical means. In principle, this method can be extended to devices made of monolayers of 2D magnets.

2.2 Introduction

Two-dimensional ferromagnet $Cr_2Ge_2Te_6$ (CGT) is so resistive below its Curie temperature that probing its magnetism by electrical transport becomes extremely difficult. By forming heterostructures with Pt, however, we observe clear anomalous Hall effect (AHE) in 5 nm thick Pt deposited on thin (< 50 nm) exfoliated flakes of CGT. The AHE hysteresis loops persist to ~ 60 K, which matches well to the Curie temperature of CGT obtained from the bulk magnetization measurements. The slanted AHE loops with a narrow opening indicate magnetic domain formation, which is confirmed by low-temperature magnetic force microscopy (MFM) imaging.

These results clearly demonstrate that CGT imprints its magnetization in the AHE signal of the Pt layer. Density functional theory calculations of CGT/Pt heterostructures suggest that the induced ferromagnetism in Pt may be primarily responsible for the observed AHE. Our results establish a powerful way of investigating magnetism in 2D insulating ferromagnets which can potentially work for monolayer devices.

Although bulk CGT crystal is conductive at high temperatures, its resistance becomes extremely high in the ferromagnetic phase below 60 K [7-9]. Under very large bias voltages, the two-terminal resistance and magnetoresistance of CGT crystal could be measured [10]. Large back gate electric field was used to lessen the insulating behavior of thin CGT flakes (~10-50 nm) so that the AHE could be detected [11]. In recent studies of three-dimensional (3D) magnetic insulators such as $Y_3Fe_5O_{12}$ and $Tm_3Fe_5O_{12}$, an effective way of probing their magnetic properties is to take advantage of the induced transport

properties in a metal layer such as Pd, Pt, Ta, etc. by forming heterostructures with the former [12-16].

The magnetic insulator properties are thus imprinted in the induced transport properties such as magnetoresistance and AHE in the metal layer. Similar proximity induced polarization-dependent photoluminescence was found in WSe_2 by forming heterostructure with CrI_3 [3]. Here we adopt the same approach by fabricating CGT/Pt heterostructures with exfoliated CGT flakes and detecting induced magneto-transport properties in Pt.

2.3   Transport and Magnetic Properties of Bulk CGT Flakes

2.3.1   Magnetic Properties of Bulk CGT Flakes

Before studying induced magneto-transport properties, we first characterize the intrinsic properties of CGT itself. Magnetization measurements are performed on bulk CGT crystals using a SQUID magnetometer. The Curie temperature, $T_c \sim 61$ K, was determined from the abrupt drop in magnetization in the temperature dependence from 5 K – 300 K when a 1 kOe magnetic field is applied parallel to the a-b plane of the crystal [9,10]. Magnetization measurements below T_c with an external magnetic field either parallel or perpendicular to the a-b plane reveal soft ferromagnetic behavior with perpendicular magnetic anisotropy determined by comparison of the field required to saturate all the spins in both geometries, i.e., $H^{\parallel}_{sat} > H^{\perp}_{sat}$ [9,10].

2.3.2 Fabrication of Thin Flake CGT Devices for Transport Measurements

To confirm the transport behavior in thin exfoliated CGT flakes, we improved the Hall bar device fabrication to minimize the contact resistance by avoiding lithographic process after the exfoliation. We first patterned 5 nm Pt electrodes onto an exfoliated flake of boron nitride (BN) on a SiO_2 substrate by electron beam lithography (EBL). A second flake of BN was used to pick up and transfer a CGT flake onto the pre-patterned Pt electrodes. The top BN is larger than the CGT so that the two BN flakes encapsulate the CGT flake as is illustrated in figure 2.1. All the transfer and exfoliation of CGT was performed in an argon filled glovebox with < 0.1 ppm H_2O and O_2 to protect the flakes from degradation. After transfer, no further fabrication steps took place and the device was exposed to ambient conditions for < 20 minutes during the device mounting before it was moved into an evacuated cryostat.
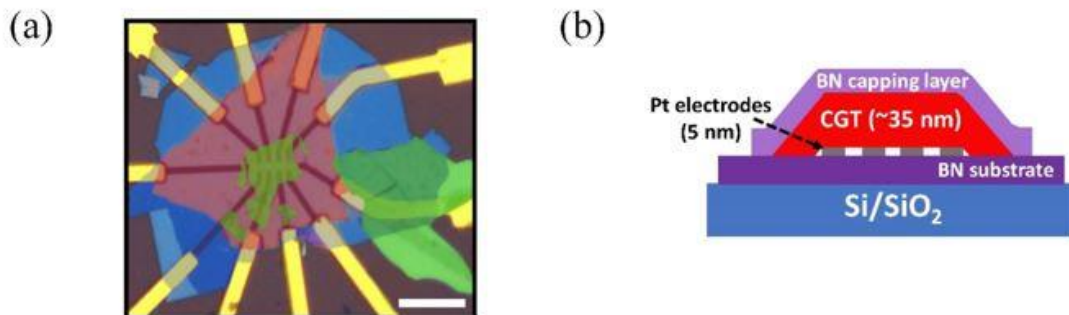
Figure 2.1. CGT Device Image. (a) Optical micrograph of CGT transport device with 10 μm scale bar. False coloring is used to distinguish the different material layers: bottom BN in blue, CGT in green, and top BN in red. (b) Schematic illustration of the side view of the device in (a).

2.3.3   Transport Measurement of Thin Flake CGT Devices.

We measured the transport properties of the device from 300 K down to 5 K through the I-V characteristics. Figure 2.2 (a) shows the current measured while sweeping bias voltage between the source and drain electrodes for representative temperatures between 5 K and 100 K. In the range of 5 K – 60 K, the measured current is negligibly small for $|V_{\text{Bias}}| < 5$ V. Inset shows the I-V curves obtained at higher temperatures, 200 K and 300 K, both well above the magnetic ordering temperature with vertical scale in µA. Over the temperature range of 100 – 300 K, the contact resistance is relatively small. We calculated the resistance in the linear I-V regime over this temperature range and determined the band gap, $E_G \sim 0.23$ eV, by fitting the thermal activation model, $\rho(T) = \rho_0 \exp\left(\frac{E_G}{2k_BT}\right)$, as shown in the inset of Figure 2.2 (b). This value is similar to the reported value of $E_G \sim 0.2$ eV [9,10]. Because of the very insulating behavior at and below T_c, it is very difficult to observe any AHE signal in the ferromagnetic phase.
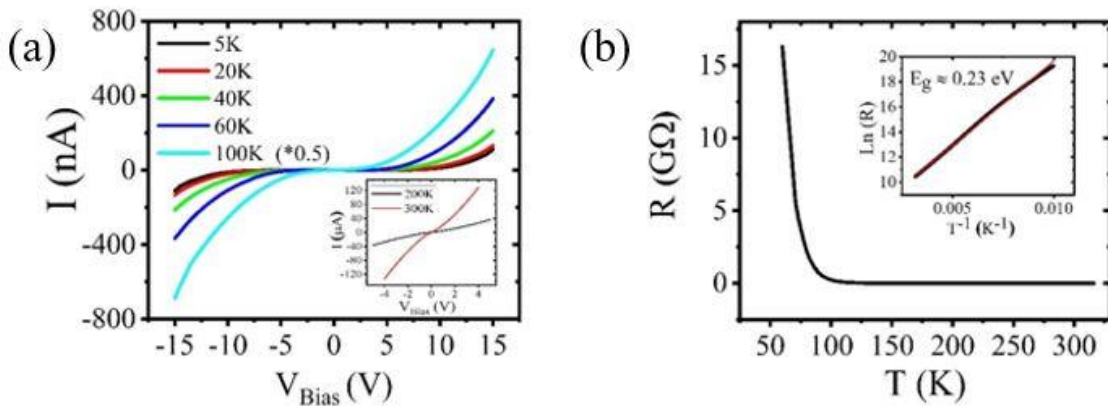
Figure 2.2. Transport Properties of CGT Device. (a) I-V characteristics of device in figure 2.1 measured at representative temperatures down to 5 K with 200 K and 300 K inset with vertical scale in µA. (b) Resistance vs. temperature measurement for the temperature range of 320 K to 60 K. Inset: Logarithmic plot of resistance vs. 1/T over the temperature range of 100-300 K with linear fit to extract the band gap.

2.4 Magneto-Transport in CGT/Pt Heterostructures

2.4.1　CGT/Pt Heterostructure Device Fabrication

To have strong induced magneto-transport properties in Pt, it is important to have a very clean interface in the CGT/Pt heterostructures [17]. Due to the air sensitivity of CGT flakes (more information on the degradation of CGT in ambient conditions can be found in the discussion at the end of the chapter), we also modified the standard fabrication steps for less air sensitive 2D materials to minimize the interface degradation. A schematic of this fabrication process is given in Figure 2.3a. In the existing setup, we could not transfer samples from the glovebox into the sputtering chamber without exposing to air; therefore, we performed the exfoliation in the load lock of the sputtering system, and immediately evacuated the chamber to greatly reduce the O_2 and H_2O exposure time to the freshly cleaved CGT surface, followed by Pt deposition. Once the load lock pressure reached below $5*10^{-6}$ torr, the samples were loaded into the main chamber which has a base pressure of 10^{-7} torr. We next heat the samples in chamber at above 100 ⁰C to remove water vapor which may have accumulated on the materials surface. Since the oxidation can take place on a very short time scale, the surface layer oxidation is unavoidable. To remove the likely oxidized surface layer, we etch the CGT flakes in the sputtering chamber with argon plasma at a power of 15 W with pressure of 40 mtorr, immediately followed by deposition of 5 nm Pt. The Pt layer is not only the active layer for sensing the induced AHE, but also serves as a capping layer to prevent further oxidation in the subsequent device fabrication.
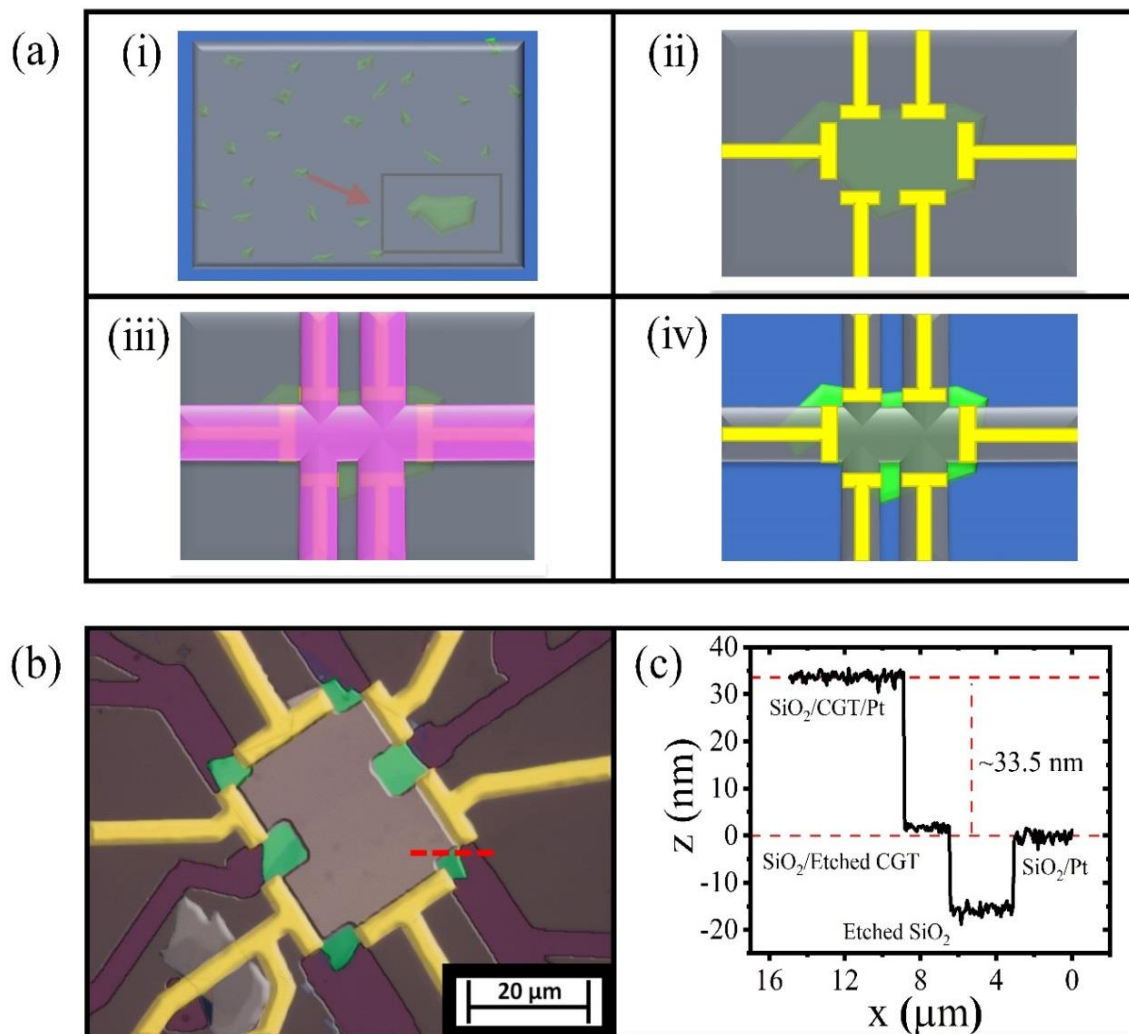
Figure 2.3 The Fabrication of CGT/Pt Hybrid Devices. (a) Schematic of the device fabrication process. (i) Exfoliated CGT flakes covered by 5 nm Pt. (ii) Au electrode deposition on the chosen CGT flake shown in the box in (i). (iii) E-beam resist mask (cyan) for defining a Hall bar. (iv) Pt etching and e-beam resist removal. (b) Optical micrograph of CGT/Pt heterostructure with false color to clarify different regions of the device. False coloring is used to distinguish the different material layers: Pt in gray, CGT in green, Au in yellow, and SiO$_2$ in dark red. (c) Line cut from AFM image of CGT/Pt device. The cut line is represented by the red dashed line in (b).

Once removed from the sputtering chamber, the sample with many exfoliated flakes was viewed under optical microscope to locate a desired piece for making device ((i) in Fig. 2.3a). EBL and lift-off process were performed to deposit 60 nm thick Au electrodes ((ii) in Fig. 2.3a). Inductively coupled plasma etching was then used to etch the Pt layer to form Hall bar structure ((iii) and (iv) in Fig. 2.3a). Figures 2.3b and 2.3c show a representative device on a ~ 35 nm thick CGT flake and the height profile of the same device obtained with atomic force microscopy (AFM). The fabrication steps adopted here allow for a high device yield and are critical to achieving a high-quality CGT/Pt interface enabling the AHE in all devices we studied.

2.4.2.   Results of the AHE and Magnetoresistance Measurements

Using this method, we successfully fabricated multiple CGT/Pt heterostructure devices in a range of CGT thickness down to ~ 35 nm. Thinner exfoliated CGT flakes are typically too small to be fabricated into the Hall bar device structure. The data presented in this this results section all came from the device pictured in Figure 2.3b. Results from some of the other devices are qualitatively similar and are included in the last part of this chapter of the dissertation.

Figure 2.4 shows the induced AHE data in Pt measured at selected temperatures from 5 to 65 K using a current of 2.0 mA in applied magnetic fields perpendicular to the cleaved plane, i.e., the 2D layers. These hysteresis loops are obtained after subtracting a linear ordinary Hall background (an example of full Hall hysteresis is shown in Fig. 2.6(a)) for all temperatures. Since Pt itself is paramagnetic and no hysteresis loop is expected for

standalone Pt, the fact that AHE in Pt only appears below T_c of CGT indicates that it is caused by the presence of the ferromagnetic CGT. Therefore, Pt AHE hysteresis merely reflects the magnetic hysteresis of the underlying CGT. In fact, similar slanted Kerr rotation hysteresis loops of ~ 19 nm CGT were recently reported [18] as well as in Fe_3GeTe_2 flakes >15 nm [19]. Note that the AHE hysteresis loops are significantly slanted and only a small fraction of the saturation value of AHE resistivity is retained at zero magnetic field. It suggests formation of non-uniform magnetization configurations such as domains.
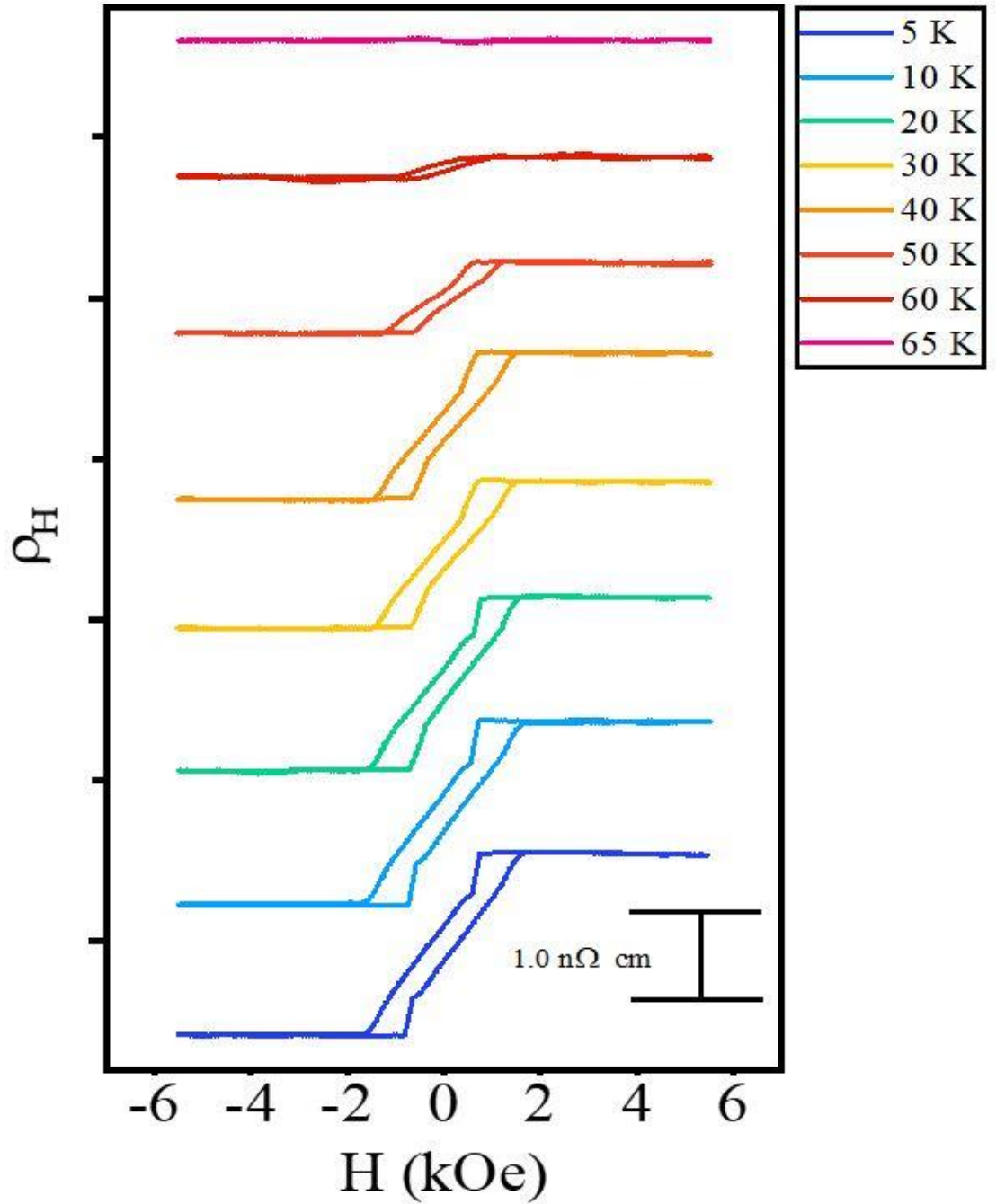
Figure 2.4. AHE. AHE hysteresis loops for select temperatures from 65 K to 5 K after subtraction of the linear ordinary Hall background.

The magnetoresistance data at T = 4 K are also consistent with the slanted AHE hysteresis loop, as shown in figure 2.5a. To obtain the spontaneous AHE resistivity, we extrapolate the high-field linear background to zero field and plot the intercept as a function of temperature in Figure 2.5b. Above 60 K, AHE signal falls below the noise level, and the only remaining Hall signal is from the ordinary Hall effect of the Pt layer.
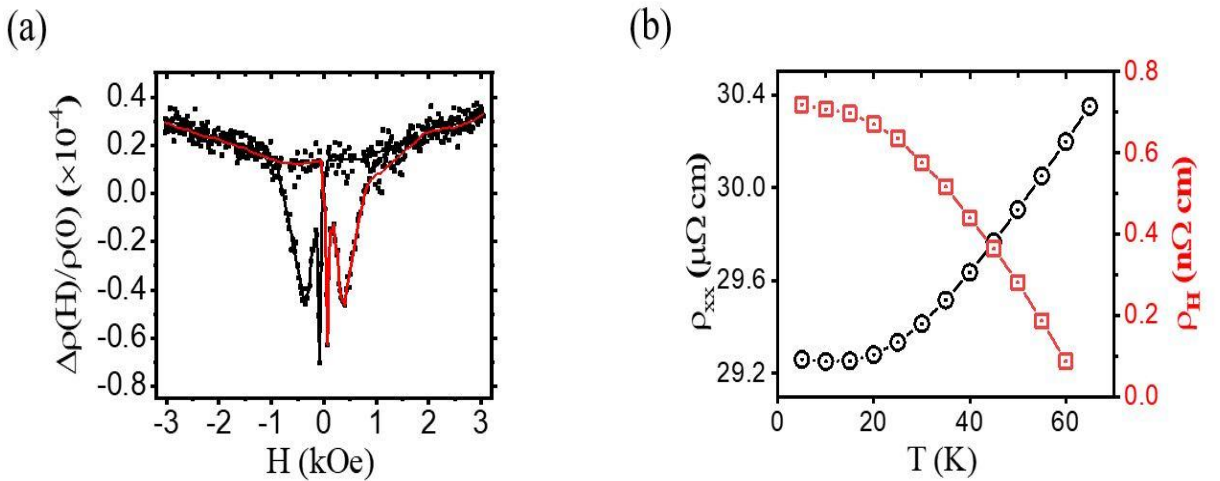
Figure 2.5. Magnetoresistance. (a) Magnetoresistance measured at 4 K. (b) Magnitude of the measured longitudinal resistivity and Hall voltage as a function of temperature.

2.4.3. Experimental Methods

The transport measurements were performed in a physical properties measurement system by Quantum Design at temperatures down to 4 K. A current of 2 mA is fixed in the device while the potential drop between source and drain is monitored with a Keithley 2400 sourcemeter. Two Keithley 2182A nanovoltmeters are used to monitor V_{xx} and V_H. The

measurement is setup with the detection direction of R_H determined by the "right-hand rule" to properly determine the sign of the AHC.

2.5 Magnetic Force Microscopy of CGT/Pt Heterostructures

2.5.1. Experimental Results

It is known that the multi-domain or vortex state is favored in thick patterned ferromagnetic films [20] due to the dipolar energy winning over the exchange energy. To understand the Hall hysteresis loops of Pt which mirrors the magnetization state of CGT, we performed low-temperature magnetic force microscopy (MFM) measurements under applied magnetic fields. Along with a 4 K AHE loop of Pt, figure 2.6 shows a series of MFM images taken on a different CGT/Pt device of a similar CGT thickness under perpendicular magnetic fields at 7 K. The applied magnetic fields during MFM imaging correspond to different points labeled in the hysteresis loop. In the present measurement geometry, the MFM signal characterizes the second order derivative of the out-of-plane component of the stray magnetic field, i.e., d^2H_z/dz^2. For samples with out-of-plane magnetization, MFM has responses both inside individual domains and at the domain walls. While it may not be straightforward to directly associate the MFM signal with the magnetization direction, the spatial variation of MFM signals qualitatively indicates the abundance of the domains which are seen in several images presented below.

For a 2 kOe applied field in the z-direction (state 1), the magnetization of CGT is fully saturated, and it should be in a single-domain state. It is indeed confirmed by the uniform MFM contrast. As the field is lowered, the single-domain state is preserved until

the field reaches ~ 0.5 kOe (state 2) at which point multiple domains emerge. It is in good correspondence to the reduced AHE signal from the saturation value. The sharp drop at point 2 in the AHE loop signals the domain nucleation. As the field is reduced further, the opposite domains expand, leading to stronger MFM contrast, and the AHE signal decreases accordingly. This trend continues until the field reaches -1.5 kOe at which field an oppositely oriented single-domain state is realized (state 4). Although the magnetization direction is reversed compared to state 1, the MFM contrast remains the same because the tip magnetization, having a relatively low coercive field of ~400 Oe, is also reversed thus generates a force gradient in the same direction as the opposite saturation field (state 1).

When the magnetic field is reversed, a similar trend is observed, and similar domain nucleation and expansion patterns are displayed at points 4 and 5. This sequence of MFM measurements shows close correspondence to the AHE loop and thus confirms that the AHE signal in the Pt layer tracks the behavior of the underlying CGT flake.
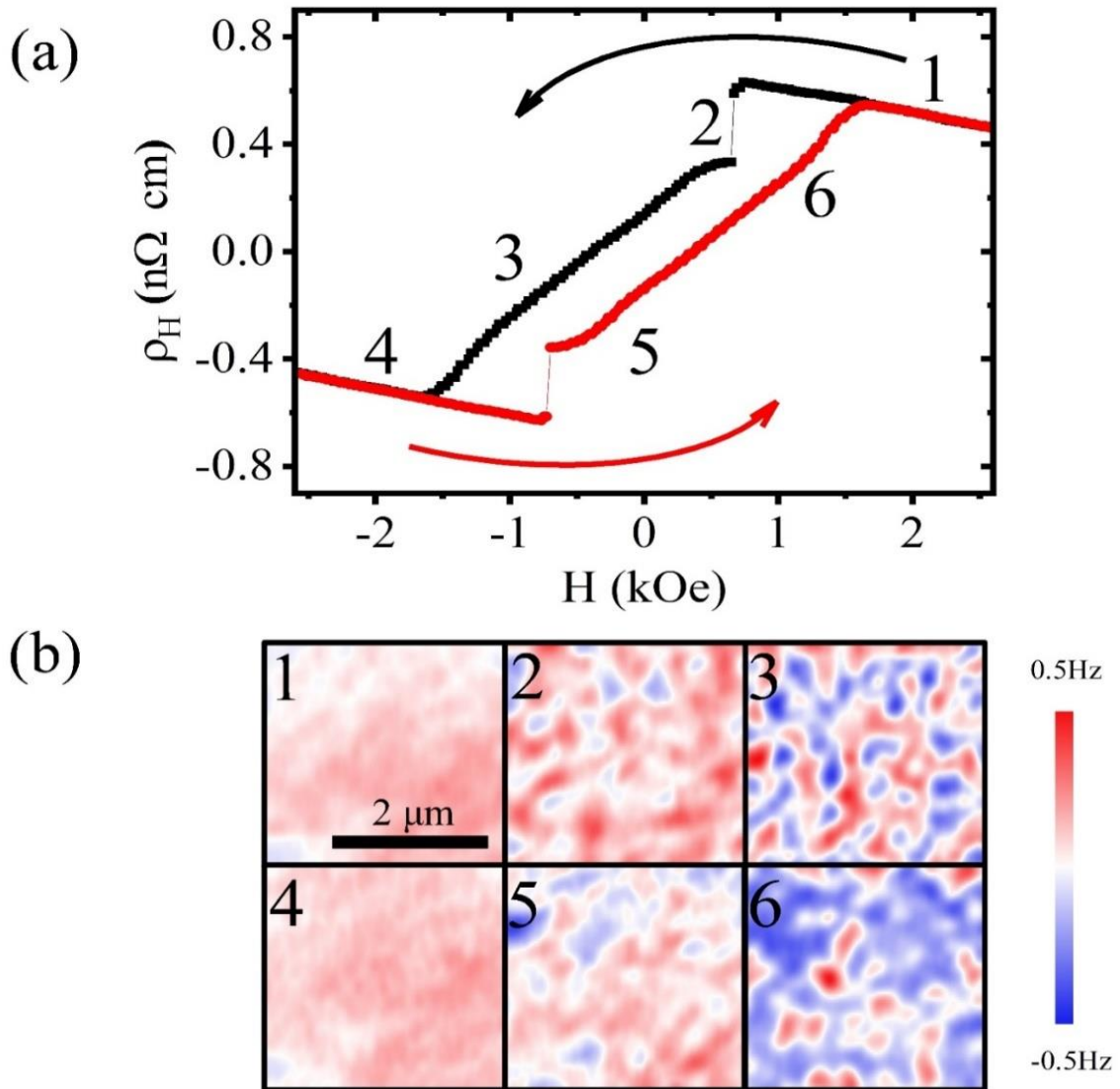
Figure 2.6. Correspondence Between AHE Measurement and MFM. (a) Anomalous Hall hysteresis loop measured at 4 K. (b) Frequency shift contrast images of CGT/Pt taken with low-temperature MFM at different magnetic fields that correspond with the points marked in (a).

2.5.2. MFM Measurement Details

The MFM measurements were performed in a home-built low temperature scanning probe microscope using commercial MFM probes (Bruker MESP-V2) with a spring constant of ~3 N/m, a resonance frequency at ~ 75 kHz, and a Co-Cr magnetic coating. MFM images were taken in a constant height mode with the tip scanning plane at ~80 nm above the sample surface. The MFM signal, the change in the resonance frequency, is measured by a Nanonis SPM Controller using a phase-lock loop.

2.6   Density Functional Theory Calculations

2.6.1. Details of the Calculation

Our DFT calculations are carried out by using VASP [25,26]. Electronic exchange-correlation is described by the generalized-gradient approximation with the functional proposed by Perdew, Berke, and Ernzerhof (PBE) [27]. We utilize projector-augmented wave pseudopotentials to describe core-valence interaction [28,29] and set the energy cutoff for plane-wave expansions to be 500 eV [27]. Atomic structures are fully optimized with a criterion that requires the force on each atom being less than 0.01 eV/Å. The LSDA+U method [30], with an effective $U_{eff}=1.0$ eV [1], is employed to take the correlation effect of Cr $3d$ electrons into account. We include the nonlocal vdW functional (optB86b-vdW) [31,32] to correctly describe the interaction across CGT and Pt layers.

Considering that CGT is a van der Waals material, a CGT monolayer is utilized in building up CGT/Pt heterostructures to reduce computational loads. Moreover, we use $\sqrt{7} \times \sqrt{7}$ supercell of (111)-Pt (lattice constant a=7.33 Å) and stretch the lattice constant

of CGT monolayer to match this supercell. Two heterostructures, one with 4-layer Pt (CGT/4L-Pt) and the other with 5 nm (22-layer) Pt (CGT/5 nm-Pt), are explicitly considered in this work. Note that we only calculate the former's AHC, since it is tractable to the current computation ability. A 13-Å vacuum layer is adopted to avoid artificial interactions between periodic slabs. We consider three representative atom alignments, namely, one of Pt atoms of the first-layer Pt sitting directly on the top of (i) Ge, (ii) Te and (iii) Cr, respectively (Figure S1). We find that the case (i) is most stable with a much lower energy than cases (ii) and (iii) (Figure S1). So, we focus on the AHC of case (i).
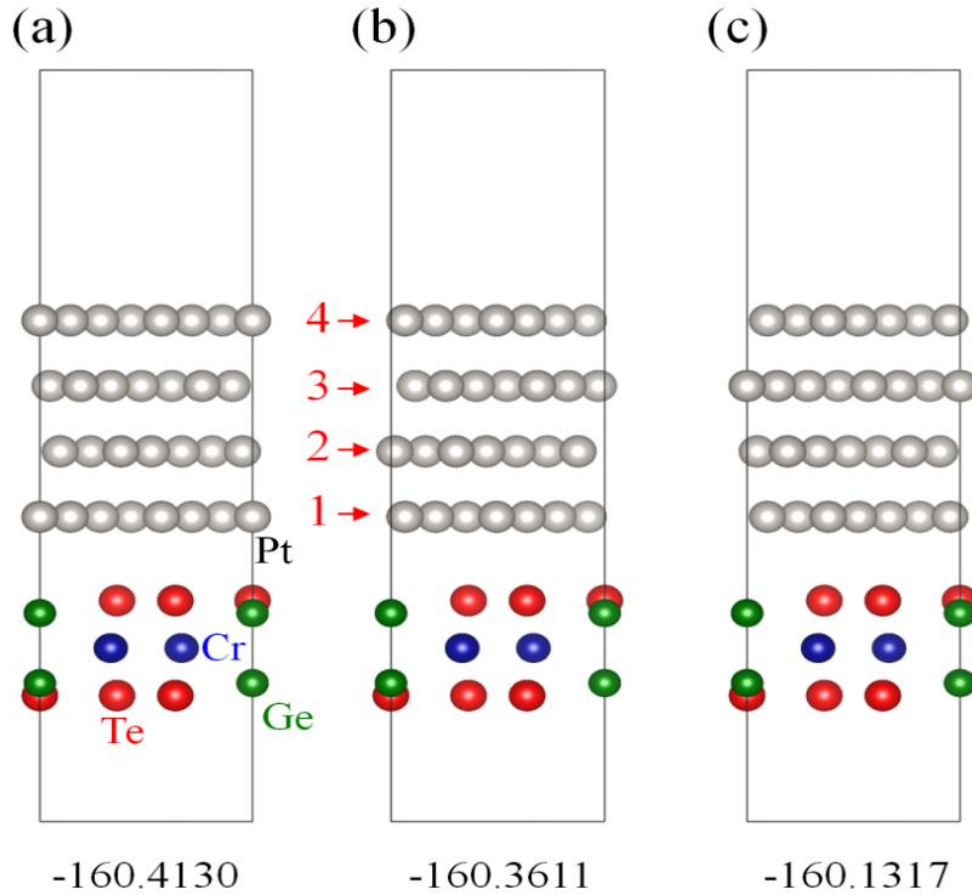
Figure 2.7. Atomic Alignments for 4L-Pt on CGT. Three representative atom alignments in CGT/4L-Pt. One of Pt atoms of the first layer of Pt slab sits directly on the top of (a) Ge, (b) Te and (c) Cr. The numbers in red show the layer index of Pt slab. The blue, green, red and gray balls represent the Cr, Ge, Te and Pt atoms, respectively. The numbers on the bottoms in (a), (b) and (c) are the DFT calculated total energies (in units of eV).

2.6.2. Result of the Calculations

In heterostructures containing 3D magnetic insulator and a heavy metal layer such as Pt, there is a debate about the mechanism of the induced AHE, i.e., whether it is due to induced magnetism in Pt or a spin current effect [10,20-22]. Either mechanism can imprint the magnetization states in the AHE of Pt. Although it is not the primary focus of this work,

we explore the origin of the induced AHE in CGT/Pt heterostructures by performing density functional theory (DFT) calculations.

The real-space distribution of spin density ($\Delta\sigma = \rho_\uparrow - \rho_\downarrow$, where $\rho_\uparrow$ and $\rho_\downarrow$ are spin-up and spin down charge densities, respectively) and its planar average of the CGT/4L-Pt heterostructure are shown in Fig. 2.7a and 2.7b. Clearly, ferromagnetic CGT introduces noticeable spin polarization in all Pt layers. Interestingly, $\Delta\sigma$ around Pt atoms in the first layer oscillates rapidly in the lateral plane, as they align differently with Cr atoms, and its planar average is small in the first Pt layer and maximizes in the second Pt layer. This is different from previous results for Pt films on traditional magnetic films such as Fe, Co and Ni, where the atomic alignment at the interface is much simpler [17]. Overall, the averaged induced magnetic moment in of CGT/4L-Pt is 0.0074 μ_B per Pt atom and parallel to the magnetic moments of Cr^{3+} ions.

To examine the range of induced spin polarization in Pt, we also calculated the CGT/22L-Pt (5 nm Pt, which is comparable to our experimental samples) heterostructure and found that the average magnetic moment drops to 0.0009 μ_B per Pt atom. Using the method proposed by Y. Yao et al [24], we determined the anomalous Hall conductivity (AHC) of CGT/4L-Pt heterostructure to be 2700 S/m. To estimate the AHC in CGT/Pt heterostructure with 5 nm thick Pt, we first studied the AHC in a toy model, i.e., AHC in monolayer Pt that is subjected to exchange interaction and consequently acquires a magnetic moment. By varying the exchange strength, we found that the AHC linearly decreases as the magnetic moment of Pt decreases from 0.01 μ_B per Pt atom to zero as

shown in Figure 2.7c. This linear relation allows us to estimate the AHC value in thicker Pt films if the magnetic moment of the Pt films is calculated. In fact, the fully calculated AHC and induced magnetic moment for the 4L-Pt fall right on the extended straight line. We calculated the average magnetic moment of the CGT/5 nm-Pt heterostructure and obtained 0.0009 μ_B per Pt atom.

Based on Figure 2.7c, we estimated the AHC in CGT/5-nm-Pt heterostructure to be 328.4 S/m, which is larger than the experimentally measured value of 82.3 S/m at 4 K. The discrepancy can be caused by several possibilities. First, the CGT/Pt interface in real device is by no means as perfect as that assumed in the calculations, which can reduce the magnitude of AHC. Second, the spin current contribution could produce an AHE signal with the opposite sign. Nevertheless, the good agreement in both sign and magnitude of the AHC for CGT/5 nm-Pt suggests that the induced ferromagnetism in Pt may be the main mechanism of the observed AHE.
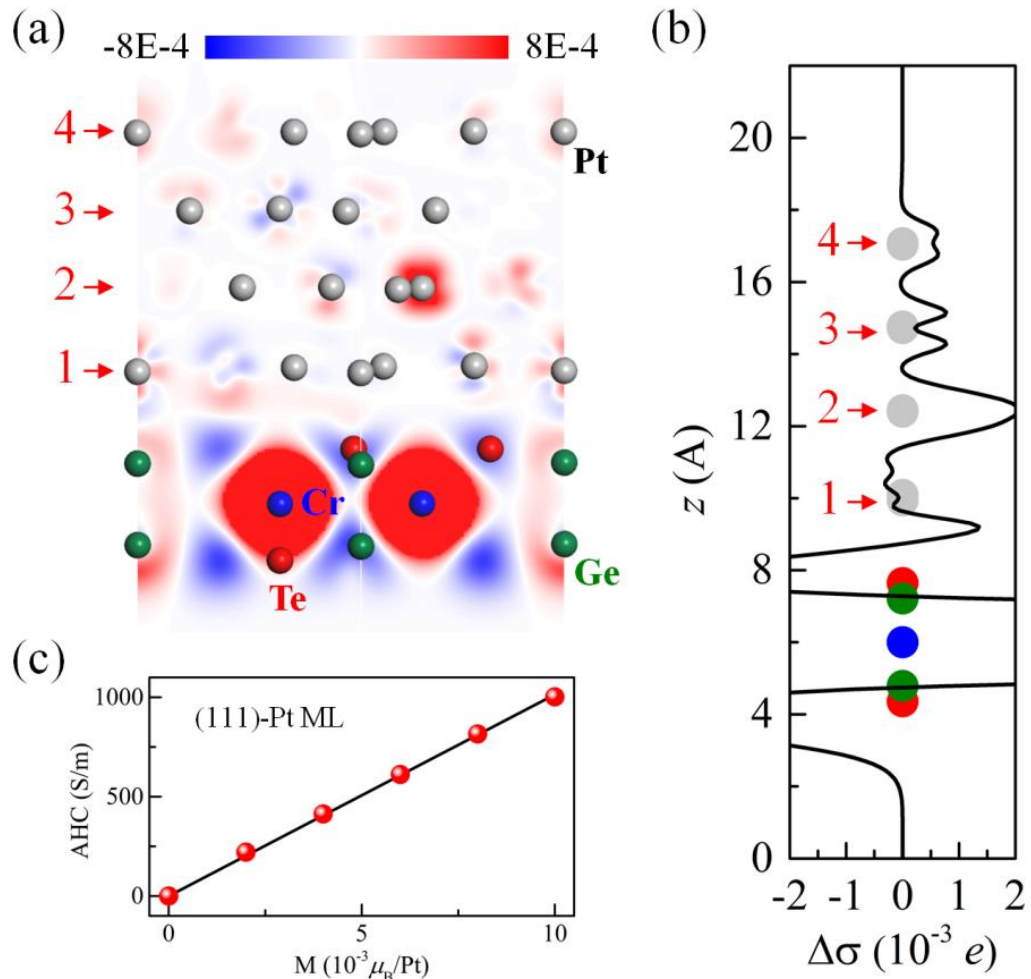
Figure 2.8. DFT Details and Results (a) Real-space distribution of the spin density difference $\Delta\sigma$ and (b) Planar-averaged spin density difference $\Delta\sigma$ in CGT/4L-Pt. In (a) and (b), Cr, Ge, Te and Pt atoms are represented by the blue, green, red and gray balls, respectively. The layer index of Pt layer is shown by the numbers in red. (c) Dependence of the AHC on the magnetic moments of Pt in Pt ML.

2.7   Summary

In conclusion, we have successfully measured the AHE in Pt by forming heterostructures of Pt with thin exfoliated flakes of CGT. The induced AHE as a function of temperature resembles the magnetization of CGT and the distinct features in the AHE hysteresis loops can be mapped to different magnetic domain states in CGT imaged by MFM. DFT calculations show that the observed induced AHE is consistent with the induced moment in Pt arising from the hybridization between Cr 3d electrons and Pt. These results indicate that CGT can be useful in heterostructures with graphene as well as other two-dimensional materials in order to realize the QAHE.

2.8   Discussion

2.8.1. Oxidation of CGT Flakes when Heated in Ambient Environment

To ensure a clean interface with good proximity between CGT and Pt it is important that CGT is not heated to a temperature above 120 ⁰C during the fabrication. To illustrate this, we performed a study of the effects of heating on the oxidation of the CGT flakes. We a chose a large CGT flake to get a better resolution in the dark field images. The CGT flake sat on a hot plate for 30 seconds at temperatures from 80 ⁰C to 180 ⁰C, in 10 ⁰C intervals. Dark field images were taken both before and after heating for each temperature. The first image was obtained right after exfoliation was performed at room temperature. The flake showed no obvious signs of degradation for temperatures up to 120 ⁰C as can be seen in the comparison of the 23 ⁰C and 120 ⁰C images. After the flake was heated at 130 ⁰C, it began to degrade, and small dots appeared on its surface which were only visible in dark

field images. The image taken after heating at 140 ⁰C shows a slightly rougher surface than the 120 ⁰C image indicating that the oxidation was enhanced. The remaining images taken after being heated at 150 ⁰C, 160⁰C, and 180 ⁰C, show the oxidation increase dramatically such that the surface roughness is at least larger than the cleaved edges of the areas of constant thickness. Bright field images, shown in the right column of figure 4.9, taken directly after exfoliation and after all the heating steps show signs of degradation, especially in the thin region near the bottom right of the images, but not as obvious as in the dark field images.
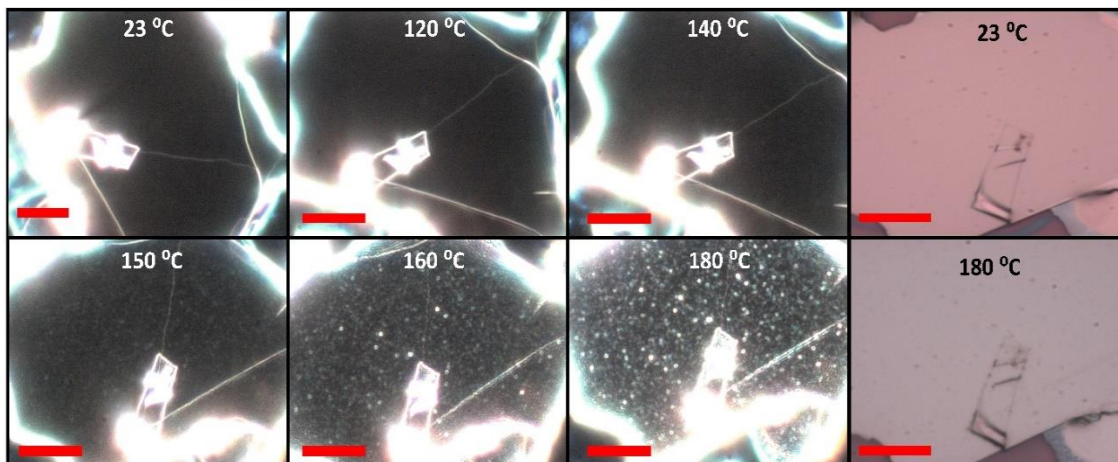
Figure 2.9. Oxidation of CGT Flakes. Temperature series of dark field images of ~80 nm exfoliated CGT flake taken in 30 second intervals from 23 ⁰C to 180 ⁰C along with bright field images. The lines of the flake's surface visible in all images are reflected light at the edge of an area of constant thickness due to the layers cleaving off during exfoliation. A small piece of the flake folded on the surface during exfoliation but does not affect the results of this study. The scale bar in all images is 20 μm.

2.8.2. Reproducibility of AHE in CGT/Pt

We performed low temperature transport measurements of CGT/Pt in multiple device to prove the reproducibility of our results. In all devices measured the magnitude of the 4K AHC was similar. The loop shape is somewhat different due to variations in the CGT thickness as well as the structure of the CGT flake used in that device.
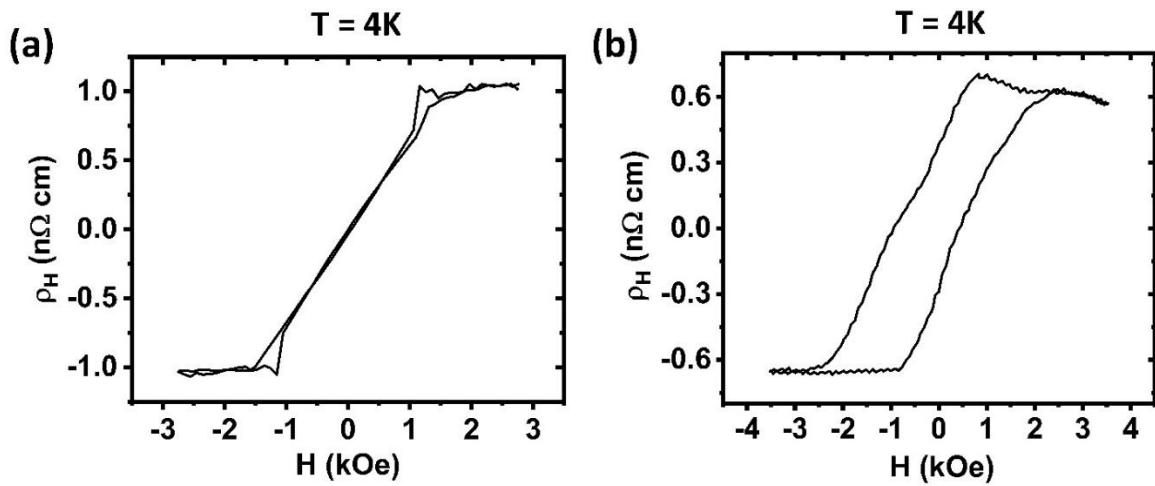
Figure 2.10. AHE in Additional Devices. (a,b) 4 K AHE hysteresis loops obtained from two additional devices confirming the reproducibility of our results. The device thickness is ~150 nm in for the device measured for graph (a) and ~50 nm for the device measured for (b).

References:

[1]   Gong, C.; Li, L.; Li, Z.; Ji, H.; Stern, A.; Xia, Y.; Cao, T.; Bao, W.; Wang, C.; Wang, Y.; Qui, Z. Q.; Cava, R. J.; Louie S. J.; Xia, J.; Zhang, X. Discovery of intrinsic ferromagnetism in 2D van der Waals crystals. *Nature* **2017**, *546* (7657), 265–269.

[2]   Huang, B.; Clark, G.; Navarro-Moratalla, E.; Klein, D. R.; Cheng, R.; Seyler, K. L.; Zhong, Di.; Schmidgall, E.; McGuire, M. A.; Cobden, D. H.; Yao, W.; Xiao, D.; Jarillo-Herrero, P.; Xu, X. Layer-dependent ferromagnetism in a van der Waals crystal down to the monolayer limit. *Nature* **2017**, *546* (7657), 270–273.

[3]   Zhong, D.; Seyler, K. L.; Linpeng, X.; Cheng, R.; Sivadas, N.; Huang, B.; Schmidgall, E.; Taniguchi, T.; Watanabe, K.; McGuire, M. A.; Yao, W.; Xiao, D.; Fu, KM. C.; Xu, X. Van der Waals engineering of ferromagnetic semiconductor heterostructures for spin and valleytronics *Sci. Adv.* **2017**, *3* (5), 1–7.

[4]   Song, T.; Cai, X.; Tu, M. W.-Y.; Zhang, X.; Bevin Huang, Nathan P. Wilson, K. L. S.; Lin Zhu, Takashi Taniguchi, K. W.; McGuire, M. A.; Cobden, D. H.; Xiao, D.; Yao, W.; Xu, X. Giant tunneling magnetoresistance in spin-filter van der Waals heterostructures. *Science* **2018**, *360, 1214-1218*.

[5]   Tan, C.; Lee, J.; Jung, S. G.; Park, T.; Albarakati, S.; Partridge, J.; Field, M. R.; McCulloch, D. G.; Wang, L.; Lee, C. Hard magnetic properties in nanoflake van der Waals Fe_3GeTe_2. *Nat. Commun.* **2018**, *9* (1554).

[6]   Ohno, H.; Chiba, D.; Matsukura, F.; Omiya, T.; Abe, E.; Dietl, T.; Ohno, Y.; Ohtani, K. Electric-field control of ferromagnetism. *Nature* **2000**, *408*, 944–946.

[7]   Carteauxts, V.; Brunet, D.; Ouvrardt; André, G. Crystallographic, magnetic and electronic structures of a new layered ferromagnetic compound $Cr_2Ge_2Te_6$. *J. Phys. Condens. Matter* **1995**, *7*, 69–87.

[8]   Ji, H.; Stokes, R. A.; Alegria, L. D.; Blomberg, E. C.; Tanatar, M. A.; Reijnders, A.; Schoop, L. M.; Liang, T.; Prozorov, R.; Burch, K. S.; Ong, N. P. Petta, J. R. Cava R. J. A ferromagnetic insulating substrate for the epitaxial growth of topological insulators. *J. Appl. Phys.* **2013**, *114* (114907).

[9]   Zhang, X.; Zhao, Y.; Song, Q.; Jia, S.; Shi, J.; Han, W. Magnetic anisotropy of the single-crystalline ferromagnetic insulator $Cr_2Ge_2Te_6$. *Japanese J. Appl. Phys. To* **2016**, *55* (033001).

[10]   Lin, Z.; Lohmann, M.; Ali, Z. A.; Tang, C.; Li, J.; Xing, W.; Zhong, J.; Jia, S.; Han, W.; Coh, S.; Beyermann, W.; Shi, J. Pressure-induced spin reorientation transition in layered ferromagnetic insulator $Cr_2Ge_2Te_6$. *Phys. Rev. Mater.* **2018**, *2* (5), 051004.

[11]   Xing, W.; Chen, Y.; Odenthal, P. M.; Zhang, X.; Yuan, W.; Su, T.; Song, Q.; Wang, T.; Zhong, J.; Jia, S.; Xie, X. C.; Li, Y. Han, W. Electric field effect in multilayer $Cr_2Ge_2Te_6$: a ferromagnetic 2D material. *2D Mater.* **2017**, *4*.

[12]   Huang, S. Y.; Fan, X.; Qu, D.; Chen, Y. P.; Wang, W. G.; Wu, J.; Chen, T. Y.; Xiao, J. Q.; Chien, C. L. Transport magnetic proximity effects in platinum. *Phys. Rev. Lett.* **2012**, *109* (10), 1–5.

[13]   Lin, T.; Tang, C.; Alyahayaei H. M.; Shi, J. Induced magneto-transport properties at palladium/yttrium iron garnet interface. *Phys. Rev. Lett.* **2014**, *113* 037203.

[14]   Yang, Y.; Wu, B.; Yao, K.; Shannigrahi, S.; Zong, B.; Wu, Y. Investigation of magnetic proximity effect in Ta/YIG bilayer Hall bar structure. *J. Appl. Phys.* **2014**, *115* (17).

[15]   Tang, C.; Sellappan, P.; Liu, Y.; Xu, Y.; Garay, J. E.; Shi, J. Anomalous Hall hysteresis in $Tm_3Fe_5O_{12}$/Pt with strain-induced perpendicular magnetic anisotropy. *Phys. Rev. B* **2016**, *94* (14), 1–5.

[16]   Meyer, S.; Schlitz, R.; Geprägs, S.; Opel, M.; Huebl, H.; Gross, R.; Goennenwein, S. T. B. Anomalous Hall effect in YIG|Pt bilayers. *Appl. Phys. Lett.* **2015**, *106* (13).

[17]   Pütter, S.; Geprägs, S.; Schlitz, R.; Althammer, M.; Erb, A.; Gross, R.; Goennenwein, S. T. B. Impact of the interface quality of Pt/YIG(111) hybrids on their spin Hall magnetoresistance. *Appl. Phys. Lett.* **2017**, *110* (1).

[18]   Wang, Z.; Zhang, T.; Ding, M.; Dong, B.; Li, Y.; Chen, M.; Li, X.; Huang, J.; Wang, H.; Zhao, X.; Li, Y.; Li, D.; Jia, C.; Sun, L.; Guo, H. Ye, Y.; Sun, D.; Chen, Y.; Yang; T.; Zhang, J.; Ono, S.; Han, Z.; Zhang, Z. Electric-field control of magnetism in a few-layered van der Waals ferromagnetic semiconductor. *Nat. Nanotechnol.* **2018**, *13* (7), 554–559.

[19]   Fei, Z. Huang, B. Malinowski, P. Wang, W. Song, T. Sanchez, J. Yao, W. Xiao, D. Zhu, Z. May, A. F. Wu, W. Cobden, D. H. Chu, J. H. and Xu, X. Two-dimensional itinerant ferromagnetism in atomically thin Fe_3GeTe_2. *Nat. Materials*, **2018**, 17, 778–782.

[20]   Shi, J.; Tehrani, S.; Scheinfein, M. R. Geometry dependence of magnetization vortices in patterned submicron NiFe elements. *Appl. Phys. Lett.* **2000**, *76* (18), 2588–2590.

[21]   Li, J.; Yu, G.; Tang, C.; Liu, Y.; Shi, Z.; Liu, Y.; Navabi, A.; Aldosary, M.; Shao, Q.; Wang, K. L.; Lake, R.; Shi, J. Deficiency of the bulk spin Hall effect model for spin-orbit torques in magnetic-insulator/heavy-metal heterostructures. *Phys. Rev. B* **2017**, *95* (24), 1–5.

[22]   Shao, Q.; Grutter, A.; Liu, Y.; Yu, G.; Yang, C.-Y.; Gilbert, D. A.; Arenholz, E.; Shafer, P.; Che, X.; Tang, C.; Aldosary, M.; Navabi, A.; He, Q. L.; Kirby, B. J.; Shi, J.; Wang, K. L. Exploring interfacial exchange coupling and sublattice effect in heavy metal/ferrimagnetic insulator heterostructures using Hall measurements, x-ray magnetic circular dichroism, and neutron reflectometry. *Phys. Rev. B* **2018**.

[23]   Chen, Y. T.; Takahashi, S.; Nakayama, H.; Althammer, M.; Goennenwein, S. T. B.; Saitoh, E.; Bauer, G. E. W. Theory of spin Hall magnetoresistance (SMR) and related phenomena. *J. Phys. Condens. Matter* **2016**, *28* (10).

[24]   Yao, Y.; Kleinman, L.; MacDonald, A. H.; Sinova, J.; Jungwirth, T.; Wang, D. Sheng; Wang, E.; Niu, Q. First principles calculation of anomalous Hall conductivity in ferromagnetic bcc Fe. *Phys. Rev. Lett.* **2004**, *92* (3), 4.

[25]   Kresse, G.; Furthmuller, J. Efficient iterative schemes for ab initio total-energy calculations using a plane-wave basis set. *Phys. Rev. B* **1996**, *54* (16).

[26]   Kresse, G.; Furthmuller, J. Efficiency of ab-initio total energy calculations for metals and semiconductors using a plane-wave basis set. *Comput. Mater. Sci.* **1996**, *6*, 15–50.

[27]   Perdew, J. P.; Burke, K.; Ernzerhof, M. Generalized gradient approximation made simple. *Phys. Rev. Lett.* **1996**, *77* (18).

[28]   Blöchl, P. E. Projector augmented-wave method. *Phys. Rev. B* **1994**, *50* (24), 17953–17979.

[29]   Kresse, G.; Joubert, D. From ultrasoft pseudopotentials to the projector augmented-wave method. *Phys. Rev. B* **1999**, *59* (3), 1758.

[30]   Dudarev, S. L.; Botton, G. A.; Savrasov, S. Y.; Humphreys, C. J.; Sutton, A. P. Electron-energy-loss spectra and the structural stability of nickel oxide: An LSDA+U study. *Phys. Rev. B* **1998**, *57* (3), 1505.

[31]   Klimeš, J.; Bowler, D. R.; Michaelides, A. Chemical accuracy for the van der Waals density functional. *J. Phys. Condens. Matter* **2010**, *22* (2).

[32]   Klimeš, J.; Bowler, D. R.; Michaelides, A. Van der Waals density functionals applied to solids. *Phys. Rev. B* **2011**, *83* (195131), 1565–1573.

Chapter 3 Highly Efficient Spin-Orbit Torque and Switching of Layered Ferromagnet Fe_3GeTe_2

3.1 Motivation

Fe_3GeTe_2 (FGT), a layered conducting ferromagnet, is an important member of the van der Waals (vdW) material family that has attracted a great deal of attention [1,2]. Similar to other known vdW ferromagnets such as $Cr_2Ge_2Te_6$ and CrI_3, FGT possesses the magnetic anisotropy perpendicular to the atomic layers which is retained down to monolayers. Different from the others, FGT stands out due to the following attractive properties. First, not only do FGT bulk crystals have the highest Curie temperature T_c (~225 K), but monolayer FGT also has the highest T_c, (130 K), when compared to their vdW ferromagnetic counterparts [1,3,4]. Furthermore, the T_c of thin FGT can be dramatically elevated to room temperature using electrostatic gating [2]. Second, few-layer thick FGT films have been successfully grown by molecular beam epitaxy [5], which makes ultimate wafer-scale monolayer all-vdW heterostructure fabrication possible. Third, while the other vdW magnets are semiconductors or insulators, FGT is a ferromagnetic metal which allows for studying its magnetism via magneto-transport measurements.

In conventional devices using conducting ferromagnets with perpendicular magnetic anisotropy (PMA) such as CoFeB, spin-orbit torques (SOT) have been exploited for switching the magnetization [6]. SOT efficiency, the figure-of-merit for this application, contains both intrinsic properties such as the spin Hall angle of the heavy metals serving as the spin current source and extrinsic properties such as the transmission coefficient. The latter depends on the ferromagnet/heavy metal interface quality. Because of the vdW nature

that provides atomically flat interface, FGT has the potential of having high SOT efficiency for switching its magnetization, especially in all-vdW heterostructures.

3.2 Introduction

In this study, we fabricate heterostructures of FGT/Pt with 5 nm of Pt sputtered onto the atomically flat surface of ~ 15 – 23 nm exfoliated FGT flakes. The spin current generated in Pt exerts a damping-like SOT on FGT magnetization. At ~$2.5\text{x}10^{11}$ A/m^2 current density, SOT causes the FGT magnetization to switch, which is detected by the anomalous Hall effect of FGT.

To quantify the SOT effect, we measure the second harmonic Hall responses as the applied magnetic field rotates the FGT magnetization in the plane. Our analysis shows that the SOT efficiency is comparable with that of the best heterostructures containing three-dimensional (3D) ferromagnetic metals and much larger than that of heterostructures containing 3D ferrimagnetic insulators. Such large efficiency is attributed to the atomically flat FGT/Pt interface, which demonstrates the great potential of exploiting vdW heterostructures for highly efficient spintronic nanodevices.

In this work, we investigate the SOT effects in FGT/Pt heterostructure devices containing thin exfoliated FGT and sputtered Pt. In such devices, the spin Hall effect in Pt produces a pure spin current which enters the FGT layer and exerts on it both field-like and damping-like torques [7]. Different from magnetic insulator devices in which the magnetization state is read out by the induced anomalous Hall effect (AHE) in Pt via

proximity coupling [8,9], the large AHE response in FGT lends itself a sensitive detector of its own magnetization state.

To quantify the effects of SOT, we carry out two types of measurements: pulsed current switching and second harmonic anomalous Hall measurements. From both measurements, we demonstrate that the SOT efficiency in FGT/Pt is significantly larger than that in devices containing conventional three-dimensional (3D) magnetic insulators and comparable with that in the best devices containing 3D ferromagnetic metals. In addition, we have observed SOT-induced switching of FGT magnetization with high switching efficiency.

3.3 Crystal Structure and Magneto-Transport Properties of Bulk FGT Flakes

3.3.1 Crystal Structure of FGT

Fe_3GeTe_2 crystals were grown by solid-state reaction of the elements at 800 $^{\circ}$C within 5 days. After mixing the elements Fe, Ge and Te in their stoichiometric molar ratio, the mixture was pressed into a pellet, sealed in a quartz glass ampoule under vacuum and loaded into the furnace for reaction. Figure 3.1 shows the X-ray diffraction (XRD) pattern of a bulk FGT single crystal which agrees with the literature [10-14]. The XRD pattern contains only the (0 0 2n) Bragg peaks (n=1, 2, 3, 4, 5, 6), indicating that the exposed surface is the *ab*-plane of the FGT crystal. Indexation of the peaks led to the *c* lattice

parameter of 16.376 Å, which is consistent with previously reported value [10].
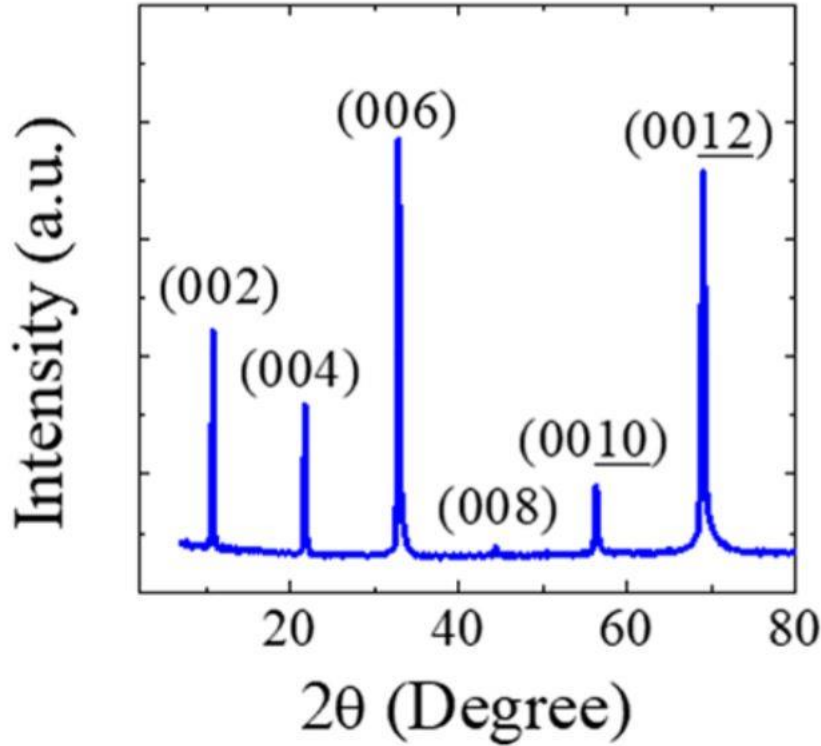
Figure 3.1. X-ray Diffraction. XRD pattern obtained from measurements taken of bulk FGT crystal.

3.3.2 Magneto-Transport Properties of FGT

3.3.2.1 Fabrication Process for FGT Thin Flake Devices

To characterize the magnetic properties of FGT, we have carried out AHE measurements. The fabrication consists of the following steps. We start with FGT crystals. After exfoliation, we locate a desired flake and perform electron beam lithography (EBL) and lift-off to fabricate Pt (30 nm) contacts to the chosen FGT flake. The process for the

FGT-only devices is similar to what will be illustrated in Fig. 3.3 for FGT/Pt heterostructure devices except that there are fewer steps here.

3.3.2.2   Magneto-Transport Results

The hysteresis loops of the anomalous Hall resistivity ρ_H for a FGT device with thickness of 53 nm are displayed in Figs. 3.2 (b) and (c) for different temperatures ranging from 2 K to 230 K (device image is shown in the inset of Fig. 3.2 (d)). Below 180 K, the ρ_H loops are squared with monotonically increasing coercive field H_c as the temperature is decreased. H_c reaches ~ 7.5 kOe at 2 K, indicating very strong PMA. At 180 K, where we perform all SOT measurements to be presented later, H_c is ~0.65 kOe. In hard-axis Hall measurements, we find the saturation field, denoted as H_k, to be ~30 kOe, which is 46 times larger than H_c. Above 180 K, the ρ_H loops deviate from the squared shape, collapse at ~210 K, and finally disappear at ~230 K. In the meantime, the magnitude of ρ_H loops, i.e., the height between the two saturated values, decreases as the temperature is raised, and vanishes at the Curie temperature T_c as illustrated in Fig. 3.2 (c). T_c of this FGT device is found to be ~225 K. A more accurate determination of T_c from the Arrott plot gives T_c =224.5 K for the same device (See Fig. 3.7). The overall temperature dependence of ρ_H resembles but slightly steeper than the mean-field magnetization of FGT (see Fig. 3.9). We note that the low-temperature M_s value ranges from 285 to 393 emu/cm^3 [11,15-19]. Since most of our SOT experiments are carried out at 180 K, we take M_s=170 emu/cm^3 at 180 K [11], which is the lower-bound M_s value for FGT. Using this M_s value and the measured anisotropy field H_k, we obtain the minimum uniaxial PMA energy of 1.1×10^7 erg/cm^3 at

180 K, which is nearly two orders of magnitude greater than that of CGT of 1.4×10^5 erg/cm^3 at ~ 4 K [20].
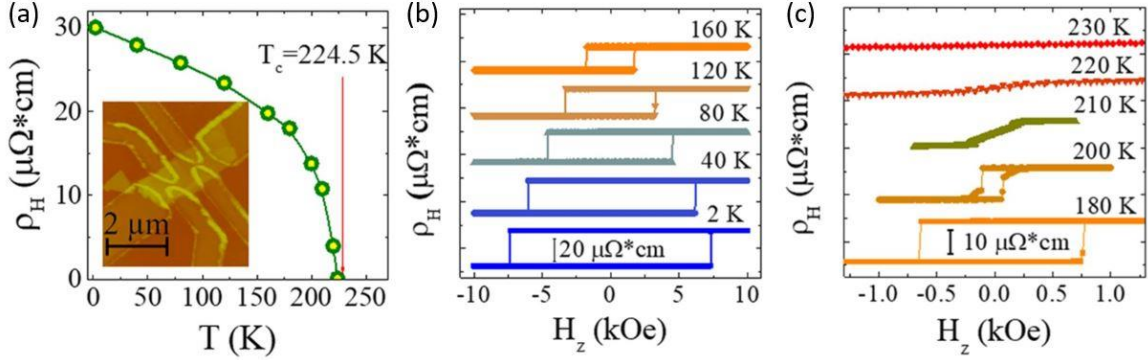
Figure 3.2. Magneto-Transport Measurement of Thin Flake FGT Device. (a) AHE amplitude of thin flake FGT device at different temperatures with T_C determined from the temperature where the AHE amplitude goes to zero. Inset is an AFM image of the device that the data is acquired from. (b,c) The acquired AHE signal at selected temperatures.

3.4   Process of FGT/Pt Device Fabrication

To fabricate FGT/Pt bilayer devices for the SOT study, we adopt the fabrication processes as represented in Fig. 3.3. FGT flakes are first exfoliated from a small crystal shown in Fig. 3.3 (a) and placed on a Si/SiO$_2$ wafer. As schematically shown from Fig. 3.3 (b) to 3.3 (e), a suitable flake is chosen (Fig. 3.3 (b)) and covered with a 5 nm layer of Pt (Fig. 3.3 (c)) by sputtering. Cr (5 nm)/Au (85 nm) electrodes are formed by EBL, e-beam evaporation, and liff-off (Fig. 3.3 (d)). The continuous Pt film covering the flake is etched by inductively coupled plasma to form isolated Cr/Au electrodes (Fig. 3.3 (d)). The scanning electron micrograph of a final device is shown in Fig. 3.3 (f). Atomic force microscopy (AFM) imaging of both FGT and FGT/Pt (See Fig. 3.8) indicates atomic level

flatness with the root-mean-square roughness of 0.2 nm, which is smaller than the atomic

step height of FGT (0.8 nm) [2].
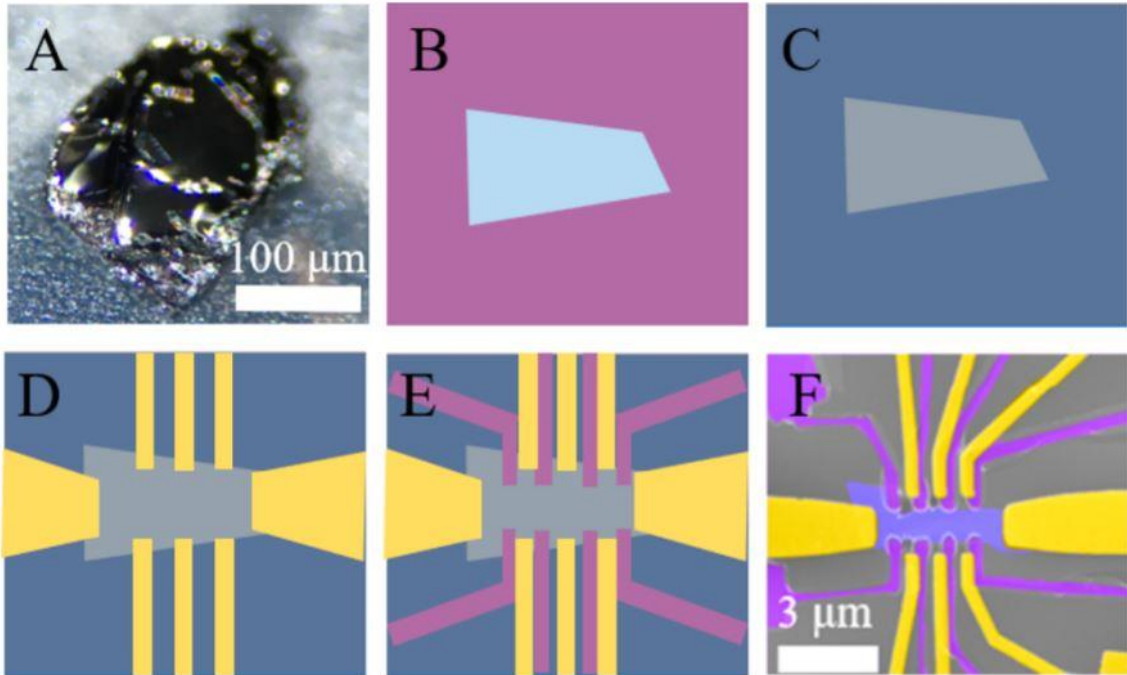
Figure 3.3. Schematic of the FGT/Pt Device Fabrication Process. The process starts with a bulk flake of FGT as pictured in (a). Next the bulk crystal is cleaved into thinner pieces with scotch tape and then placed onto an Si/SiO$_2$ substrate. Once the tape is removed many thin flakes are left on the surface of the substrate (b). 5nm Pt is then sputtered onto the substrate covering all thin flakes as well as the substrate (c). 50nm Au electrodes are then deposited by e-beam evaporation on a suitable FGT/Pt flake (d) after the electrodes are defined by EBL. One more EBL pattern is used to define a pattern in between the electrodes then ICP etching remove the Pt in that pattern (e). The resulting device is pictured in the SEM image (f). False coloring is applied in (f) to clearly indicate the different regions.

3.5 Pulsed Current Magnetization Switching and Second Harmonic Hall Measurements

3.5.1 Switching FGT Magnetization with SOT

Fig. 3.4 (a) is the schematic illustration of our FGT/Pt device for the SOT study. When a charge current passes in both Pt and FGT layers, the former generates SOTs to act on the magnetization of the latter. In the pulsed current switching experiments, we pass current pulses increasing in amplitude and interrogate the FGT magnetization state by measuring the AHE resistivity, ρ_H, after each pulse through a small constant current bias. As the current reaches a threshold, the magnetization state of FGT switches and produces a sign reversal of ρ_H. We measure the critical currents for different in-plane fields. To more accurately determine the current flowing in Pt which is responsible for the SOT acting on FGT, we use a parallel resistor model with resistivities measured separately for 5 nm Pt on SiO$_2$ and 53 nm FGT flake (See Fig. 3.9).

Before turning on sizable SOT, we first prepare the initial state of the FGT magnetization by applying an in-plane field H_x. Fig. 3.4 (b) is the AHE response of the FGT(15 nm)/Pt(5 nm) device to an H_x sweep measured at 180 K with a 50 μA current, which produces negligible SOT. This is a typical hard-axis hysteresis loop for materials with PMA.
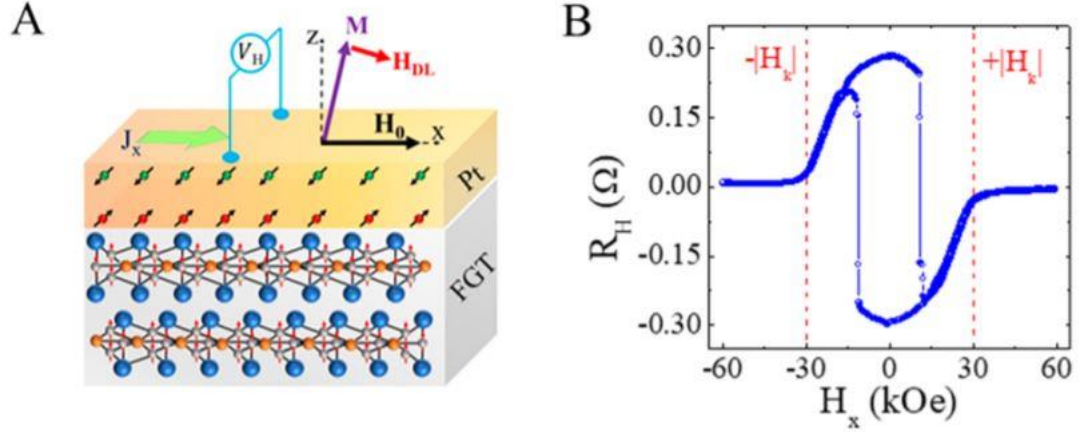
Figure 3.4. Device Schematic and Hard Axis AHE Loop. (a) Schematic of the FGT/Pt device including the measurement geometry with green and red electrons representing the opposite spin species separated in Pt by the spin Hall effect. The current direction, applied field, magnetization, and damping-like torque are represented by green, black, purple, and red arrows respectively. (b) AHE loop acquired from the FGT/Pt device used for the data in the study with the field sweep along the hard axis.

The easy-axis ρ_H hysteresis loops are very similar to those of the FGT-only device shown in Fig. 3.1 except that the presence of the Pt layer provides a shunting channel which reduces the ρ_H magnitude. At $H_x=0$, ρ_H retains the full saturation value of FGT/Pt for the easy-axis field sweeps, indicating that the initial magnetization is perpendicular to the *ab*-plane of the FGT. With a sufficiently strong H_x field, the magnetization is aligned to H_x which results in a vanishing ρ_H. This saturation field H_k is related to the strength of PMA field H_u by $H_k = H_u - 4\pi M_s$. At an intermediate in-plane field $H_x = \pm 10$ kOe, the perpendicular component of the magnetization is reversed, which is caused by the incidental z-component of the applied magnetic field due to the misalignment of the applied field with the *ab*-plane. In our pulsed current switching experiments, we set the H_x field bias below this threshold and then apply current pulses to generate additional SOT fields

to induce switching. Clearly, the effective field from the damping-like SOT, i.e., $H_{DL} \sim \boldsymbol{\sigma} \times m$, is responsible for the switching, here $\boldsymbol{\sigma}$ being the spin polarization direction of the spin current and $\boldsymbol{m}$ being the unit vector of the FGT magnetization. The critical current density J_c required to switch the magnetization depends on the magnitude of H_x. The full H_x-current switching phase diagram is shown in Figs. 3.5 (c) and 3.5 (d). Figs. 3.5 (a) and 3.5 (d) are the line cuts for three selected H_x fields: ±3, ±6, and ±9 kOe. At $H_x = -9$ kOe, switching occurs at $J_c \sim 1.5 \times 10^{11}$ A/m^2. Here the J_c value is the critical current density in Pt, which is the 73.2% of the total current passing through the FGT/Pt device. This ratio is estimated based on the resistivity values of FGT and Pt (see Fig. 3.9) using the parallel resistor model. If the strength of H_x is decreased to 3 kOe in the negative direction, J_c increases to $\sim 2.0 \times 10^{11}$ A/m^2. We extrapolate J_c linearly to $H_x=0$ along the line shown in Fig. 3 (e) and find $J_c(H_x=0) = 2.5 \times 10^{11}$ A/m^2. A similar J_c value is found for the positive H_x side, by performing the same extrapolation in Fig. 3.5 (d). To compare the effectiveness of the SOT in switching, we calculate the switching efficiency parameter η using $\eta = \frac{2eM_s t H_c}{\hbar J_c(H_x=0)}$ [8], representing the ability of switching the magnetization with SOT. H_c is ~ 0.65 kOe for FGT at 180 K, much smaller than H_k (30 kOe), indicating that switching is by domain nucleation and domain wall depinning. If again taking the lower-bound value for M_s of 170 emu/cm^3 for our FGT/Pt device, we obtain a minimum η value of 1.66. η can be as high as 2.2 if M_s is taken to be 225 emu/cm^3 at 180 K [15]. These η values are higher than those reported in Tm$_3$Fe$_5$O$_{12}$/W (0.95) [8] and Tm$_3$Fe$_5$O$_{12}$/Pt (0.014) [9] and suggest highly efficient SOT switching of FGT magnetization via local domain wall depinning.
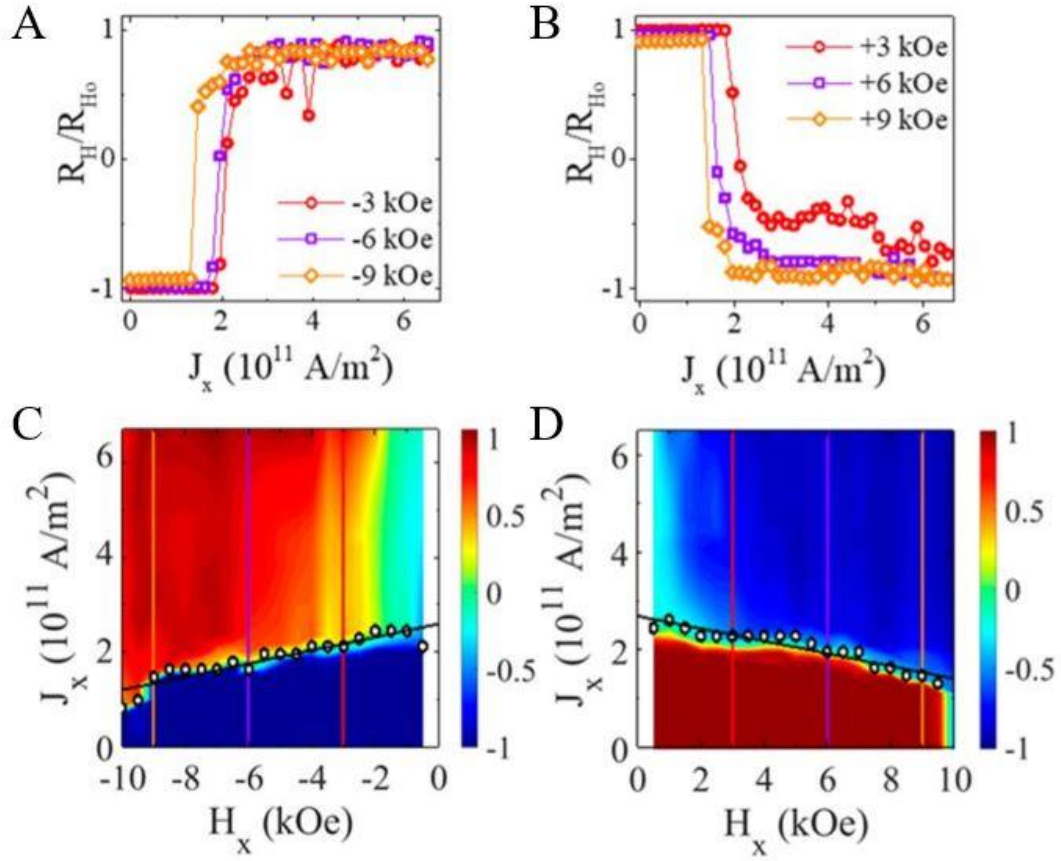
Figure 3.5. Current and Biased Field Dependence of SOT Magnetization Switching.
Effective switching current as a function of applied in-plane negative, (C), and positive, (D), bias field. The color scale represents the switching resistance as a percentage of the absolute value of the anomalous Hall resistance at zero current R_{H0}. (A,B) correspond to the line cuts in (C,D).

3.5.2 Determination of SOT Efficiency from Second Harmonic Hall Effect Measurements

To further quantify SOT, we perform second harmonic (2ω) Hall measurements on FGT/Pt devices with the measurement geometry shown in Fig. 3.6 (a). More details and application of the method were described in refs. 21 and 22. We measure the 2ω responses

in the Hall resistance, here ω being the frequency of the AC current passing through the device. The 2ω signal is present only if there is a SOT acting on the magnetization. This harmonic signal is recorded as a function of a rotating in-plane magnetic field. We rotate the magnetization with an in-plane magnetic field of fixed magnitudes that are higher than H_k and measure the second harmonic Hall signal $R_H^{2\omega}$. As indicated in Eq. 1 below, $R_H^{2\omega}$ consists of both $cos\varphi$ and $cos(3\varphi)$ terms, here φ being the azimuthal angle between the magnetic field and current direction,

$$R_H^{2\omega} = \left[R_{DL}^{2\omega} + R_{TH}^{2\omega} + \frac{R_{Oe}^{2\omega} + R_{FL}^{2\omega}}{2} \right] * cos\varphi + \frac{R_{Oe}^{2\omega} + R_{FL}^{2\omega}}{2} cos(3\varphi). \qquad (1)$$

In Eq. 1, the $cos\varphi$ term contains the damping-like SOT contribution $R_{DL}^{2\omega}$ via AHE, thermoelectric contribution $R_{TH}^{2\omega}$ via anomalous Nernst effect, Oersted field contribution $R_{Oe}^{2\omega}$ and the field-like SOT contribution $R_{FL}^{2\omega}$ via the planar Hall effect. The $cos(3\varphi)$ term contains the Oersted-field and the field-like SOT contributions $R_{Oe}^{2\omega} + R_{FL}^{2\omega}$. Fig. 3.6 (b) and 3.6 (c) display the total $R_H^{2\omega}$ signals from FGT(23 nm)/Pt(5 nm) device for different magnetic fields with the AC current amplitudes of 2.2 mA and 2.4 mA in Pt, respectively. These results can be fitted very well by the $cos\varphi$-function only, indicating the negligible effect from the field-like SOT and the Oersted field, which is usually the case for ferromagnetic metal/heavy metal heterostructures. In FGT/Pt devices, the planar Hall resistance is found to be nearly two orders of magnitude smaller than the anomalous Hall resistance (Fig. 3.10), which is the primary reason that the contributions from the field-like SOT and the Oersted field are negligibly small compared to the damping-like SOT. Further analysis of the external field strength dependence allows us to separate the damping-like

SOT effect from the thermal effect, as shown in Fig. 3.6 (d), which yields an effective SOT field H_{DL} for each current. Using the smallest M_s value of 170 emu/cm^3 for FGT at 180 K, we calculate the lower-bound damping-like torque efficiency ξ_{DL} in FGT/Pt bilayer and obtain ξ_{DL}=0.11±0.01 for 2.2 mA and ξ_{DL}=0.14±0.01 for 2.4 mA. In our ξ_{DL} calculations, we only use the current in Pt based on the parallel resistor model; therefore, it should be valid to compare this ξ_{DL} for FGT/Pt with the available ξ_{DL} values for both ferrimagnetic insulator/heavy metal and ferromagnetic metal/heavy metal heterostructures. We note that even the minimum ξ_{DL} value for FGT/Pt is significantly larger than ξ_{DL} in $Tm_3Fe_5O_{12}$/Pt (0.058 [9] and 0.015-0.02 [23]). Interestingly, our minimum ξ_{DL} compares very well with the highest value of ≈ 0.15 for CoFeB/Pt in literature [24].
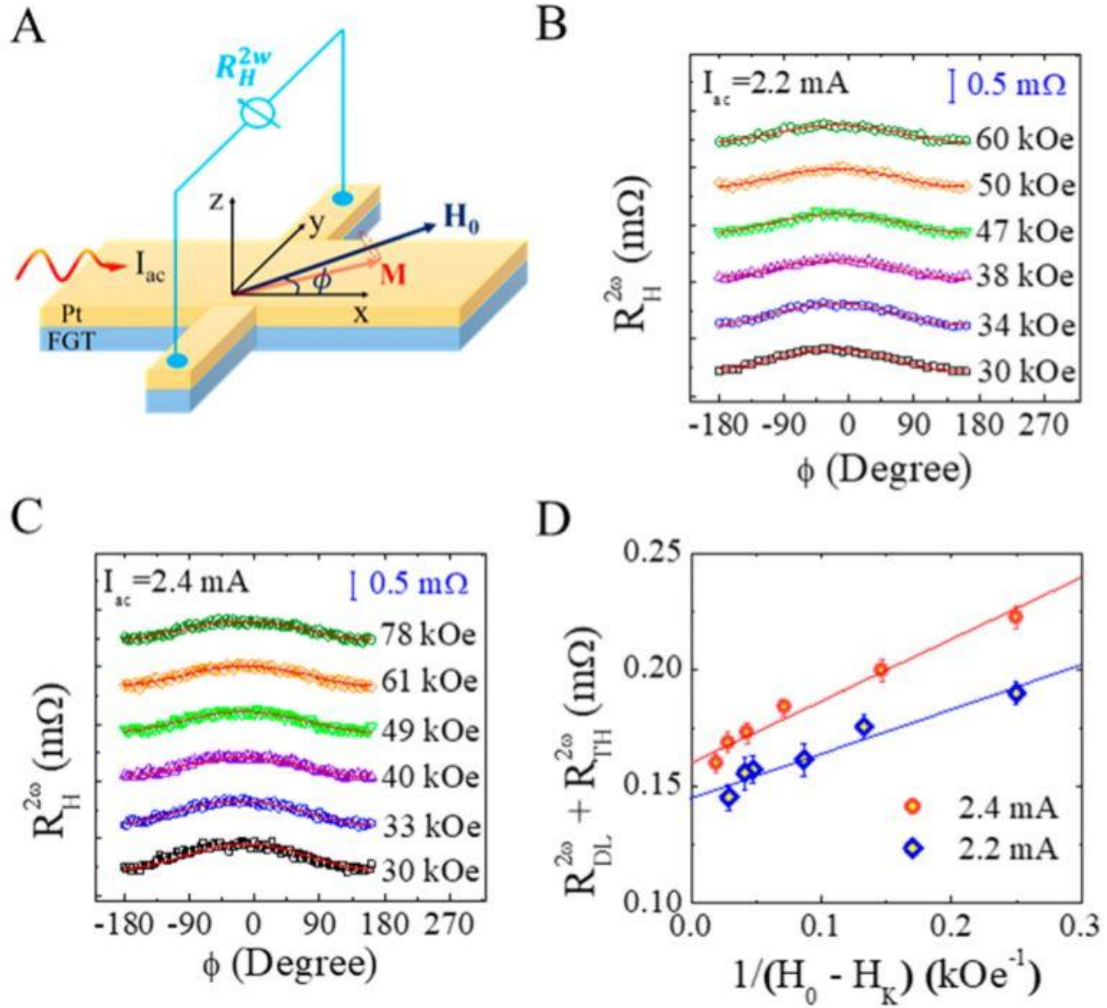
Figure 3.6. Second Harmonic Hall Measurements and SOT Efficiency. (a) Measurement geometry used for 2ω Hall effect measurements. (b,c) Data acquired from 2ω Hall measurements at various fields above H_k for an A.C. RMS current of 2.2mA (b) and 2.4mA (c). (d) 2ω Hall for damping-like SOT and thermal contributions determined from fits to the data from (b,c). The slope is used to determine the SOT efficiency of the FGT/Pt devices.

3.5.3   Comments on Switching Efficiency and SOT Efficiency

Both the switching efficiency η and SOT efficiency ξ_{DL} in FGT/Pt are higher than or comparable with those in conventional SOT devices fabricated with 3D magnetic materials. It is worth pointing out that the single-domain requirement for Eq. 1 is fulfilled

in the second harmonic Hall measurements, so that ξ_{DL} extracted from our experiments is reliable. By using the minimum M_s, this ξ_{DL} represents the lower bound value for SOT efficiency. The reason for this very high SOT efficiency in FGT/Pt is currently not completely understood. Here we believe that the excellent interface resulting from atomically flat FGT surface plays an important role; therefore, the high SOT efficiency may be common to heterostructures fabricated with other vdW ferromagnets.

3.6 Device Fabrication and Electrical Transport Measurement Details

3.6.1   Device Fabrication Details

For the FGT device, the flake is exfoliated onto a Si/SiO$_2$ substrate followed directly by spin coating 200 nm of PMMA and baking on a hotplate in air at 120 ºC for 3 minutes. This low temperature helps protect the FGT flake from degradation and oxidation. Electrode patterns are then formed by EBL followed by sputtering a 30 nm of Pt. Before deposition of the electrodes, the contact region is plasma cleaned in the sputtering chamber with 15W Ar plasma at a pressure of 30 mTorr for 30 sec. Directly after liftoff, the device is mounted and loaded into an evacuated cryostat where the transport measurements are performed.

For the FGT/Pt devices, the flakes are exfoliated onto a Si/SiO$_2$ substrate and instantly transferred into the loadlock of our sputtering system which is evacuated to a base pressure of 10^{-7} Torr. Once the base pressure is reached, the entire substrate is plasma cleaned with 15 W Ar plasma at a pressure of 30 mTorr for 30 sec. Then a 5 nm layer of Pt is sputtered forming a continuous Pt film on the substrate. Once removed from the sputtering chamber,

an optimal FGT/Pt flake is chosen by optical microscope and then EBL is performed to define an electrode pattern followed by immediate deposition of Cr(5 nm)/Au(85 nm) by electron beam evaporation. One last EBL step is then performed to define a mask to etch the FGT/Pt flake into the Hall geometry and remove all Pt connections between the electrodes. Inductively coupled plasma etching with Ar is then performed on the device and the completed device is placed into an acetone bath to remove the PMMA mask.

3.6.2 Electrical Transport Measurement Details

All transport measurements for the FGT and FGT/Pt devices are performed in the Physical Properties Measurement System by Quantum Design in a temperature range of 300 K to 2 K. For the FGT device we kept a fixed current of 50 μA in the flake with a Keithley 2400 source meter which also monitored the two-terminal resistance. To monitor the longitudinal and Hall resistances two Keithley 2182A nanovoltmeters were used. For the DC switching measurements in the FGT/PT heterostructures, a similar setup was used to monitor the response of the Hall and longitudinal resistances while a Keithley 6221 AC current source was used to pulse a square 0.5 micro second DC current through the device. For the 2ω Hall measurement, we fixed a constant AC current at a frequency of 13.113 Hz in the device with the Keithley 6221 AC current source. The 1ω and 2ω Hall responses were monitored with two Stanford Research SR830 AC lock-ins.

3.7 Summary

In summary, using both pulsed current switching and harmonic Hall measurements, we have demonstrated highly efficient SOT effects and magnetization switching in heterostructures containing a few-layer vdW ferromagnet and Pt. Since the atomic flatness of the vdW ferromagnets is an inherent property of the materials, it is expected that the high-quality interface can be retained even down to monolayers. Due to the strong PMA, switching of monolayer FGT can be potentially achieved with a much lower critical current density, which leads to much more efficient spintronic nanodevices.

2.7 Discussion

3.8.1 Determination of Curie Temperature of FGT Flake by Arrott Plot
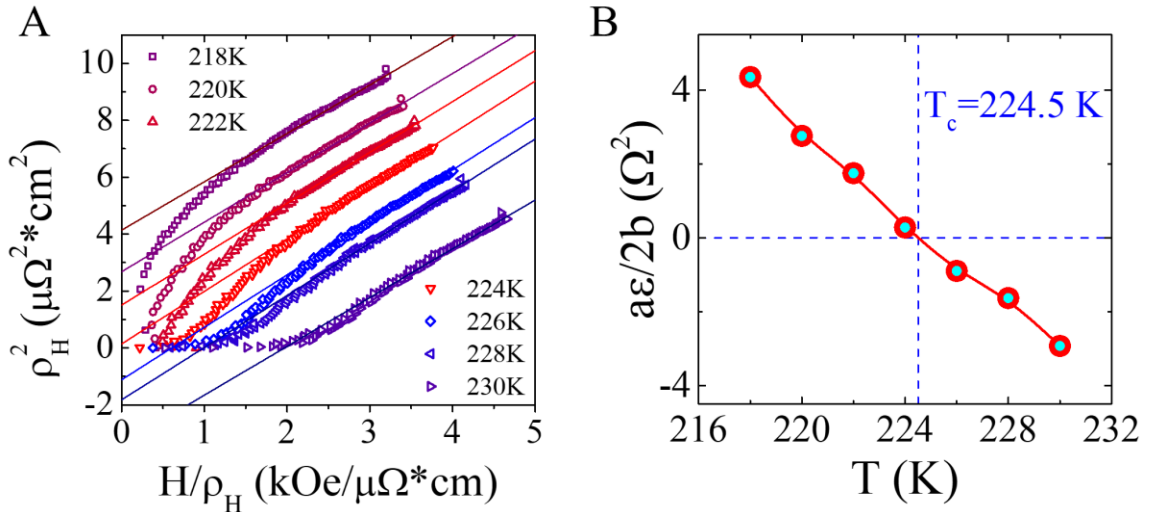
Figure 3.7. Determination of the Curie Temperature of an FGT Flake. (a) Arrott plot for determining the Currie temperature of the 53 nm thick FGT flake. (b) The y-intercept of the Arrott plot in (a) as a function of the temperature, where, $\frac{a}{2b}$, is a constant and $\varepsilon = \frac{(T-T_C)}{T_C}$. The zero-crossing point is the Curie temperature.

3.8.2   Surface Morphology Determined from Atomic Force Microscopy
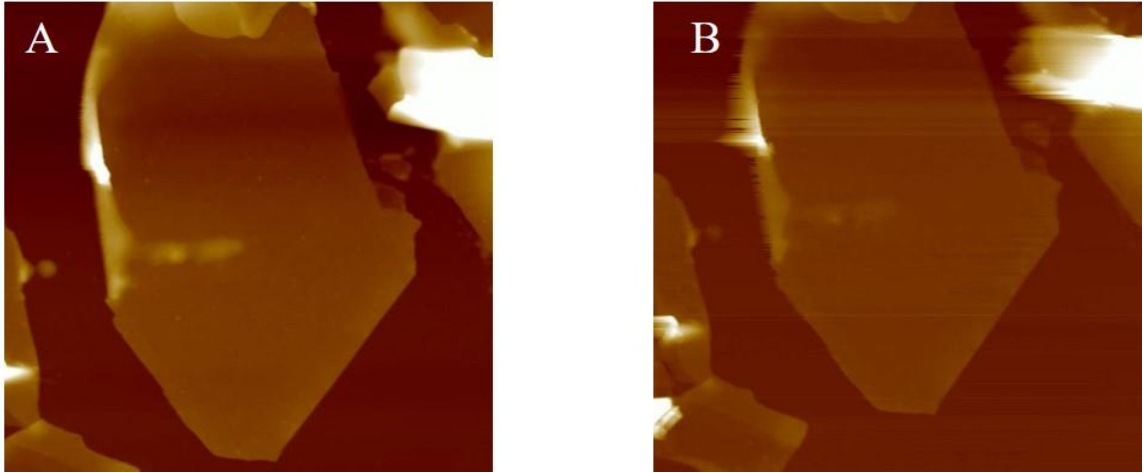
Figure 3.8. Surface Morphology of FGT Flake. (A) AFM image of an exfoliated 16 nm FGT flake. (B) AFM image of the same flake after deposition of 5 nm of Pt. The rms roughness in the area within the 1 μm^2 box is 0.19 nm in (B) and 0.21 nm for the same area in (B). Since the single atomic step height of FGT is about 0.8 nm [2], we conclude that the FGT surface is atomically flat allowing for a good interface to form between FGT and Pt.

3.11.3 Longitudinal Resistivity of FGT Flake and Pt Film

A

B
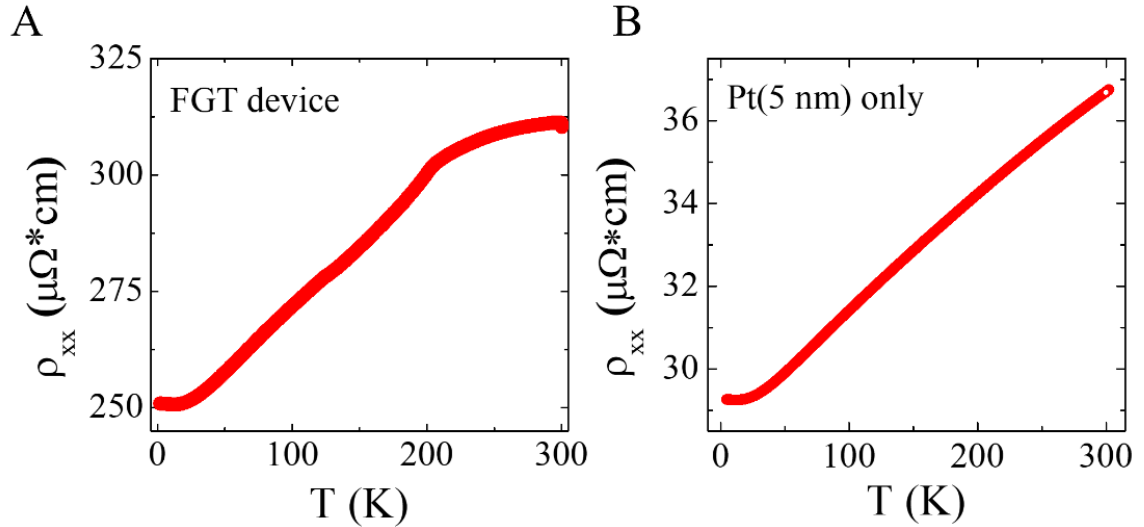
Figure 3.9. Resistivity Versus Temperature of FGT and Pt. (A) Temperature dependence of the longitudinal resistivity ρ_{xx} of a 53 nm thick FGT device. (B) Temperature dependence of ρ_{xx} of a 5 nm thick Pt device. These two sets of resistivity data are used to estimate the current that is shunted into the FGT layers.
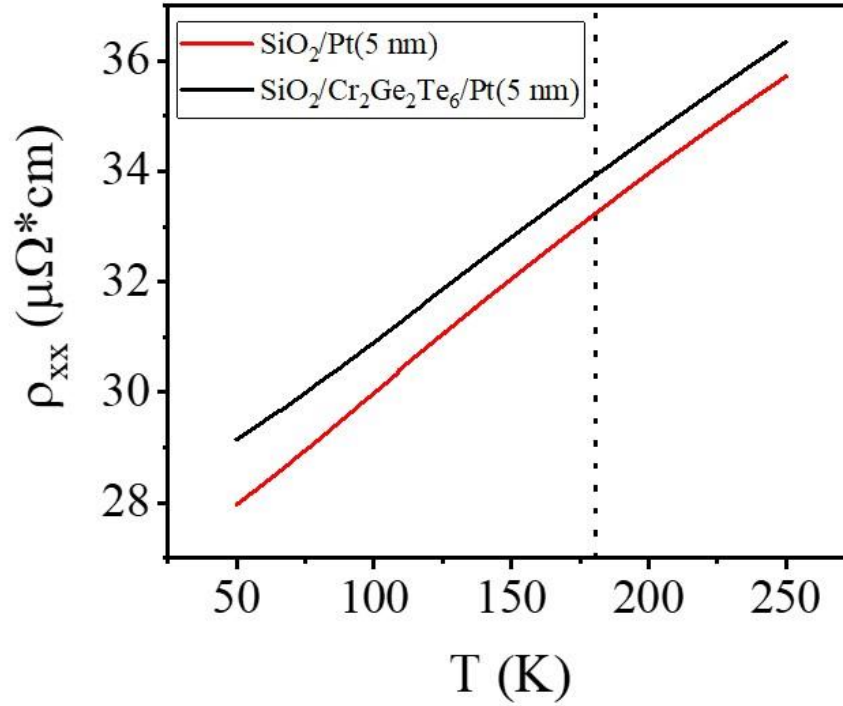
Figure 3.10. Comparison of Resistivity for 5nm Pt Hall Bar Devices on SiO₂ and CGT. Longitudinal resistivity ρ_{xx} as a function of temperature for 5 nm Pt on SiO₂ and on CGT. The SiO₂/Pt(5 nm) device has a channel width of 6 µm and the distance between the contacts used to measure resistivity is 4 µm. The SiO₂/CGT/Pt(5 nm) device has a channel width of 5.5 µm and the distance between the contacts used to measure resistivity is 11 µm. Both devices were measured at the same bias current of 0.2 mA while the system was cooled down.

The resistivity of 53 nm FGT flake in Fig. 3.9 (A) shows a slight decrease from 310 µΩ.cm at 300 K to 305 µΩ.cm at 230 K and a more rapid decrease to 250 µΩ.cm at 2 K. The steep drop at 230 K coincides with the ferromagnetic phase transition. The FGT resistivity value we measured is relatively lower than the previously reported values, e.g., 615 µΩ.cm [1], 395 µΩ.cm [17] at 180 K. This lower variation is attributed to impurities and defects in FGT. The resistivity of 5 nm Pt shown in in Fig. 3.9 (a) decreases from 37 µΩ.cm at 300 K to 29.5 µΩ.cm at 2 K. We used the FGT resistivity of 285 µΩ.cm and Pt

resistivity of 33.5 $\mu\Omega$.cm at 180 K to estimate the current shutting in FGT. This allows us to estimate the percentage of the current that flows in Pt which is responsible for the SOT.

$Cr_2Ge_2Te_6$ (CGT) is a layered van der Waals ferromagnet which is similar to FGT but a semiconductor. Atomically smooth interface can be obtained in freshly cleaved CGT flakes. Because of the high resistivity, the current in CGT/Pt heterostructures is nearly completely circuited by the Pt layer. Therefore, the resistivity of Pt in FGT/Pt is expected to be similar to that in CGT/Pt, which offers a good way of estimating the resistivity of Pt in FGT/Pt. Our measurement shows that Pt(5 nm) on CGT has the similar resistivity to Pt(5 nm) on SiO_2, which allows us to estimate the effective current flowing in Pt in FGT/Pt using the parallel resistor model.

3.8.4 Anomalous Hall Resistivity and Planar Hall Resistivity of FGT Flake
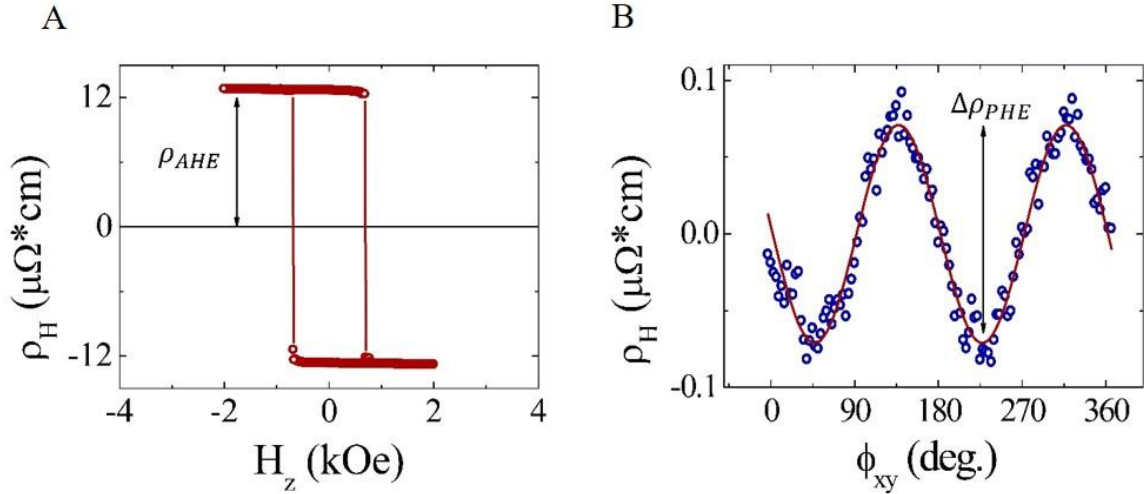
Figure 3.11. Comparison of AHE and PHE Resistivities of 53 nm FGT Flake. (A) Hall resistivity as a function of the magnetic field applied along the z axis. We determine the AHE resistivity to be, ρ_{AHE} = 12.7 μΩ*cm. (B) Hall resistivity as a function of the azimuthal angle with a fixed magnetic field, H = 80 kOe. A cos(φ) term due to the slight misalignment was removed. We determine the PHE resistivity to be, $\Delta\rho_{PHE}$ = 0.178 μΩ*cm. Both measurements were performed on the FGT device pictured in the inset of Fig. 1(D) with a fixed bias current, I = 0.1 mA, at T = 180 K.

3.8.5 Precise Determination of In-Plane Magnetic Field Orientation by Anomalous Hall Signal

Here we demonstrate how to align the magnetic field with respect to the FGT/Pt device plane by monitoring the anomalous Hall signal. As shown in Fig. 3.12, the anomalous Hall signal of FGT/Pt device changes sign once the magnetic field tilt an angle (1° or 2°) above and below the device plane. The precise field angle is determined by the saturated Hall signal value with respect to the full Hall signal when the field is applied along the z-axis. When the magnetic field is aligned perfectly in the device plane, multidomains are formed when the field is reduced from 6 T to 0 T. Nearly zero anomalous

Hall signal is observed due to the equal distribution of the up- and down-domains (Fig. 3.12 (d)).
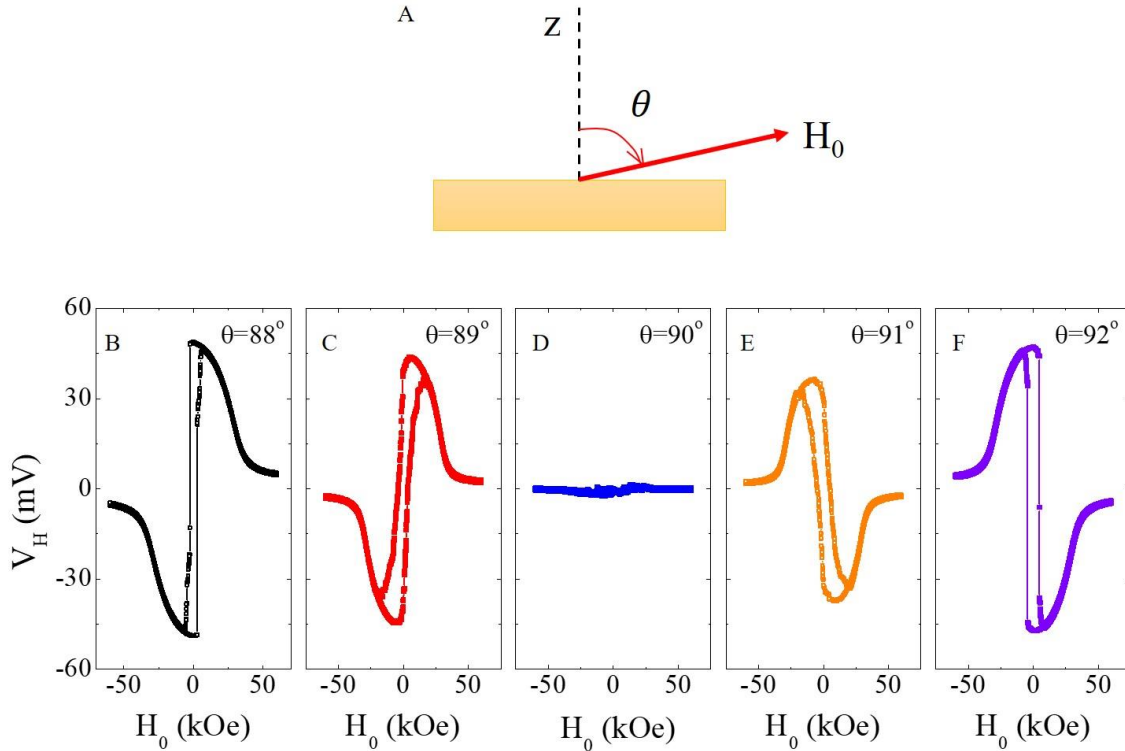
Figure 3.12. Demonstration of the Magnetic Field Alignment in the Film Plane. (A) Definition of the field orientation using angle θ. The anomalous Hall signal of one FGT/Pt device as a function of the applied magnetic field with $\theta = 88^o$ (B), 89° (C), 90° (D), 91^o(E) and 92° (F), the DC current is 0.1 mA.

3.8.6   Magnetization Switching via Domains Under Pulsed Current and Bias Magnetic Field

Here we demonstrate that the current-induced magnetization switching highly involves magnetic domain formation and movement. Fig. 3.13 (a) shows the anomalous Hall signal of a FGT(19 nm)/Pt(5 nm) device. The squared loop indicates strong

perpendicular magnetic anisotropy (PMA). This device is different from the device shown in Fig. 3.12. There is a longitudinal magnetoresistance signal mixed in the Hall signal, which can be clearly seen in the field-symmetric background Fig. 3.13 (b). Fig. 3.13 (c)-(f) present the current-induced magnetization switching under different in-plane magnetic field strengths. First of all, the change of anomalous Hall signal under pulsed currents is smaller than its full magnitude (as shown in Fig. 3.13 (a)). Only 8.9~29% of the magnetic domains are switched, which may be due to the fact that this FGT flake is too thick (~ 19 nm) and a larger critical current is needed to switch all domains. We did not apply very large current to avoid damaging the device. The critical current density required to switch the magnetization is ~3.2x10^{11} A/m^2 if we assume that all the current flows in the Pt layer (width is 0.5 μm and thickness is 5 nm), but the real value of current density is much lower than that because of the current-shunting effect of the relatively thick FGT layer. Second, the nearly symmetric V_{xy} vs. current loop can be observed under a fixed magnetic field. Third, the anomalous Hall loop changes its chirality when we reverse the magnetic field, which is consistent with the physical picture of SOT-induced magnetization switching.

Above all, here we demonstrate that the current-induced magnetization switching in a thick FGT is a highly multi-domain process. Although only partial domain switching is shown in this figure for a relatively thick device, the physical picture of SOT for thinner devices should still be applicable.
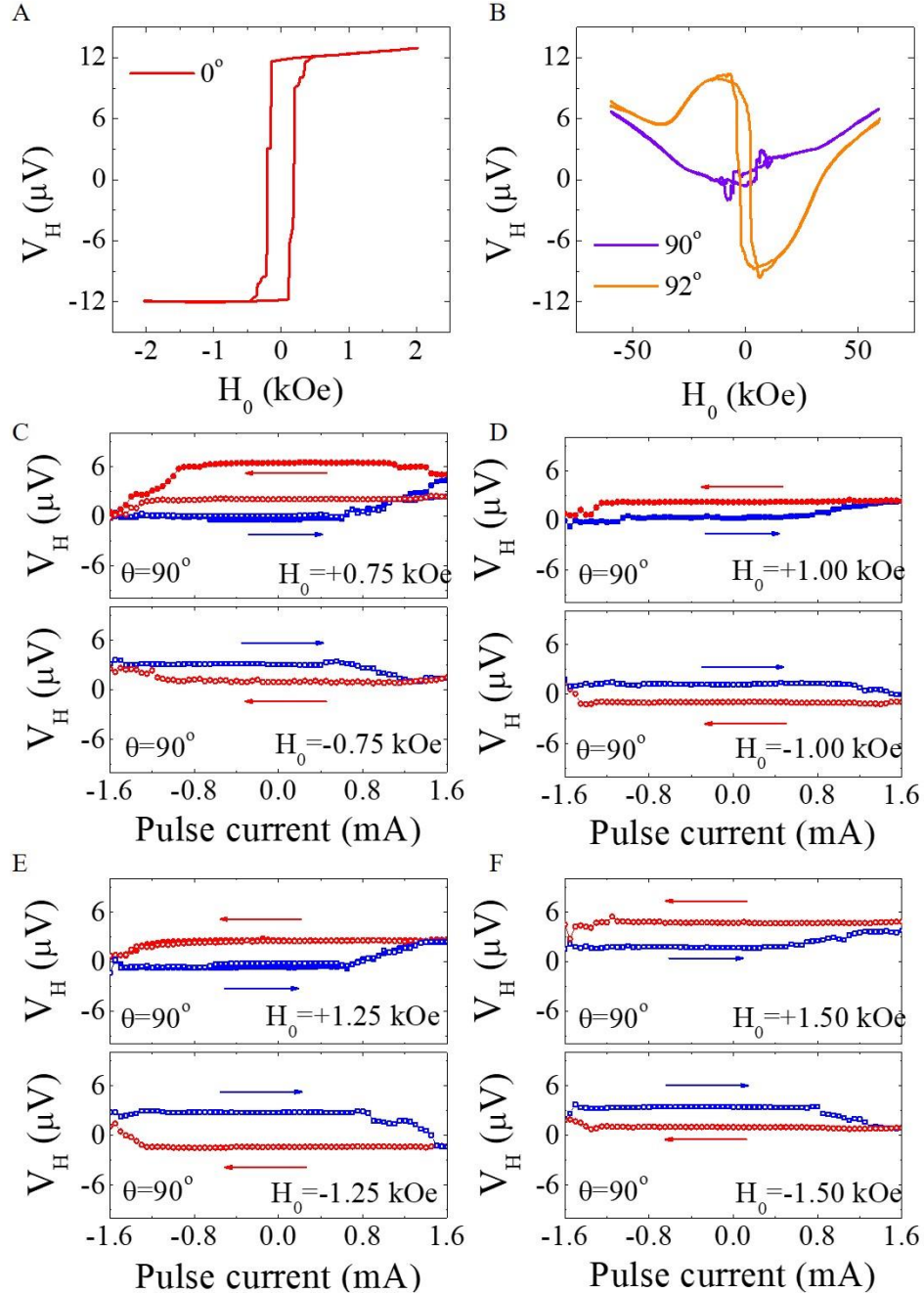
Figure 3.13. Current Induced Magnetization Switching for the FGT(19 nm)/Pt (5 nm) Bilayer Device at 180 K. (A) Anomalous Hall signal as a function of an out-of-plane magnetic field. (B) Anomalous Hall signal as a function of magnetic field with angles of 90 and 92 degrees to the z-axis. The symmetric background is from mixture of the longitudinal magnetoresistance. Current induced magnetization switching under in-plane ($\theta = 90^o$) magnetic fields of ∓ 0.75 kOe (C), ∓ 1.00 kOe (D), ∓ 1.25 kOe (E) and ∓ 1.50 kOe (F). Arrows indicate the current scan directions. The in-plane magnetic field is aligned along the current direction. The width of the Pt Hall bar is 0.5 µm.

3.8.7 Effect of Tilting Angle of Magnetic Field on Current Induced Magnetization Switching

Here we study the effect of field-orientation on current-induced magnetization switching. As we know, there is always a small H_z component when the field is not perfectly aligned in the sample plane. This H_z component may favor or disfavor the switching process and act like a bias. However, without help of a DC current, if the in-plane field is below a threshold value, the small H_z field alone cannot switch the magnetization. Since in our Fig. 3.4 (b), the tilting angle is around 1.48°, so here we also check the current-induced magnetization switching under a tilted magnetic field. As shown in Fig. 3.14, the effect of tilting angle on switching current is not obvious in this partial switching experiment. Clearly, the domain nucleation process is not so sensitive to the small tilting angle of the applied magnetic field.
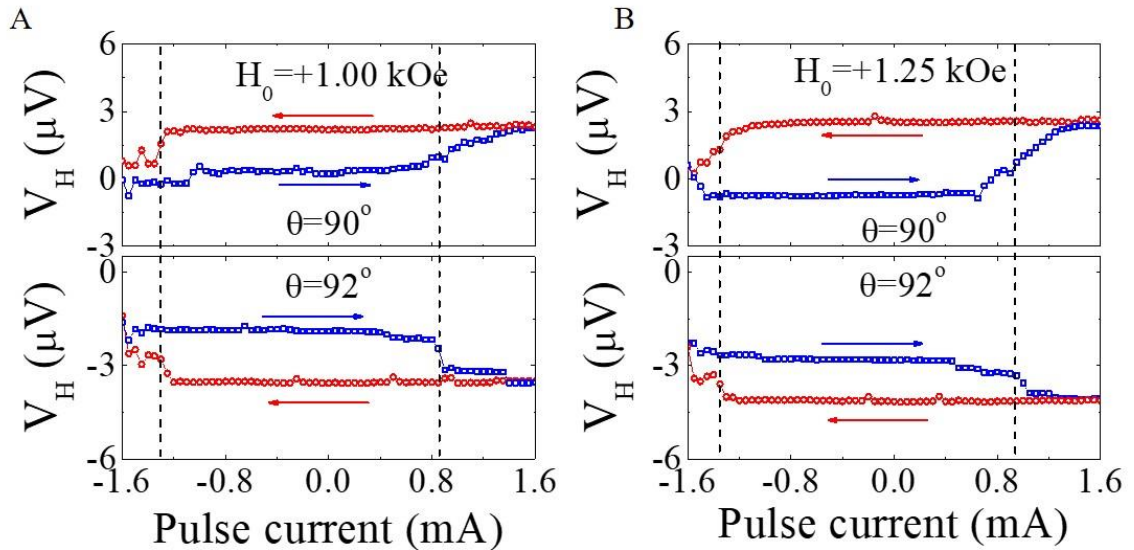
Figure 3.14. Effect of the Tilting Angle of the Magnetic Field on Current Induced Magnetization Switching. (a) Anomalous Hall signal as a function of current under the magnetic field of 1 kOe with different title angles, i.e., $\theta = 90^o$ and 92°. (b) Anomalous Hall signal as a function of current under the magnetic field of 1.25 kOe with different title angles, i.e., $\theta = 90^o$ and 92°. The experiments are performed at 180 K. The chiralities of the current-dependence loops for 90° and 92° are opposite is due to different initial magnetic states.

References:

[1]   Fei, Z.; Huang, B.; Malinowski, P.; Wang, W.; Song, T.; Sanchez, J.; Yao, W.; Xiao, D.; Zhu, X.; May, A. F.; Wu, W.; Cobden, D. H.; Chu, J.; Xu X.; Two-dimensional itinerant ferromagnetism in atomically thin Fe_3GeTe_2. *Nat. Mater.* **2018,** *17,* 778-782.

[2]   Deng, Y.; Yu, Y.; Song, Y.; Zhang, J.; Wang, N. Z.; Sun, Z.; Yi, Y.; Wu, Y. Z.; Wu, S.; Zhu, J.; Wang, J.; Chen X. H.; Zhang Y.; Gate-tunable room-temperature ferromagnetism in two-dimensional Fe_3GeTe_2. *Nature* **2018,** *563,* 94-99.

[3]   Gong, C.; Li, L.; Li, Z.; Ji, H.; Stern, A.; Xia, Y.; Cao, T.; Bao, W.; Wang, C.; Wang, Y.; Qiu, Z. Q.; Cava, R. J.; Louie, S. G.; Xia J.; Zhang X.; Discovery of intrinsic ferromagnetism in two-dimensional van der Waals crystals. *Nature* **2018,** *546,* 265-269.

[4]   Huang, B.; Clark, G.; Navarro-Moratalla, E.; Klein, D. R.; Cheng, R.; Seyler, K. L.; Zhong, D.; Schmidgall, E.; McGuire, M. A.; Cobden, D. H.; Yao, W.; Xiao, D.; Jarillo-Herrero, P.; Xu, X.; Layer-dependent ferromagnetism is van der Waals crystals down to the monolayer limit. *Nature* **2018,** *546,* 270-273.

[5]   Liu, S.; Yuan, X.; Zou, Y.; Sheng, Y.; Huang, C.; Zhang, E.; Ling, J.; Liu, Y.; Wang, W.; Zhang, C.; Zou, J.; Wang, K.; Xiu, F.; Wafer-scale two-dimensional ferromagnetic Fe_3GeTe_2 thin films were grown by molecular beam epitaxy. *2D Mater. Appl.* **2017,** *1,* 30.

[6]   Ma, Q.; Li, Y.; Gopman, D. B.; Kabanov, Y. P.; Shull, R. D.; Chien, C. L.; Switching a Perpendicular Ferromagnetic Layer by Competing Spin Currents. *Phys. Rev. Lett.* **120,** 117703 (2018).

[7]   Chen, Y.; Takahashi, S.; Nakayama, H.; Althammer, M.; Goennenwein, S. T. B.; Saitoh, E.; Bauer, G. E. W.; Theory of spin Hall magnetoresistance. *Phys. Rev. B* **2013,** *87,* 144411.

[8]   Shao, Q.; Tang, C.; Yu, G.; Navabi, A.; Wu, H.; He, C.; Li, J.; Upadhyaya, P.; Zhang, P.; Razavi, S. A.; He, Q. L.; Liu, Y.; Yang, P.; Kim, S. K.; Zheng, C.; Liu, Y.; Pan, L.; Lake, R. K.; Han, X.; Tserkovnyak, Y.; Shi, J.; Wang, K. L.; Role of dimensional crossover on spin-orbit torque efficiency in magnetic insulator thin films. *Nat. Commun.* **2018,** *9,* 3612.

[9]   Li, J.; Yu, G.; Tang, C.; Liu, Y.; Shi, Z.; Liu, Y.; Navabi, A.; Aldosary, M.; Shao, Q.; Wang, K. L.; Lake, R.; Shi, J.; Deficiency of the bulk spin Hall effect model for spin-orbit torques in magnetic-insulator/heavy-metal heterostructures. *Phys. Rev. B* **2017,** *95,* 241305 (R).

[10]   Zhang, Y.; Lu, H.; Zhu, X.; Tan, S.; Feng, W.; Liu, Q.; Zhang, W.; Chen, Q.; Liu, Y.; Luo, X.; Emergence of Kondo lattice behavior in a van der Waals itinerant ferromagnet, Fe_3GeTe_2. *Sci. Adv.* **2018,** *4,* eaao6791.

[11]   May, A. F.; Calder, S.; Cantoni, C.; Cao, H.; McGuire, M. A.; Magnetic structure and phase stability of the van der Waals bonded ferromagnet $Fe_{3-x}GeTe_2$. *Phys. Rev. B* **2016,** *93,* 014411.

[12]   Drachuck, G.; Salman, Z.; Masters, M. W.; Taufour, V.; Lamichhane, T. N.; Lin, Q.; Straszheim, W. E.; Bud'ko, S. L.; Canfield, P. C.; Effect of nickel substitution on magnetism in the layered van der Waals ferromagnet Fe_3GeTe_2. *Phys. Rev. B* **2018,** *98,* 144434.

[13]   Deiseroth, H.-J.; Aleksandrov, K.; Reiner, C.; Kienle, L.; Kremer, R. K.; Fe_3GeTe_2 and Ni_3GeTe_2—two new layered transition-metal compounds: crystal structures, HRTEM investigations, and magnetic and electrical properties. *Eur. J. Inorg. Chem.* **2006,** *2006,* 1561–1567.

[14]   Chen, B.; Yang, J.; Wang, H.; Imai, M.; Ohta, H.; Michioka, C.; Yoshimura, K.; Fang, M.; Magnetic properties of layered itinerant electron ferromagnet Fe_3GeTe_2. *J. Phys. Soc. Jpn* **2013,** *82,* 124711.

[15]   León-Brito, N.; Bauer, E. D.; Ronning, F.; Tompson, J. D.; Movshovich, R.; Magnetic microstructure and magnetic properties of uniaxial itinerant ferromagnet Fe_3GeTe_2. *J. Appl. Phys.* **2016,** *120,* 083903.

[16]   Verchenko, V.; Tsirlin, A.; Sobolev, A.; Presniakov, I.; Shevelkov, A.; Ferromagnetic Order, Strong Magnetocrystalline Anisotropy, and Magnetocaloric Effect in the Layered Telluride $Fe_{3-\delta}GeTe_2$. *Inorg. Chem.* **2015,** *54,* 8598.

[17]   Wang, Y.; Xian, C.; Wang, J.; Liu, B.; Ling, L.; Zhang, L.; Cao, L.; Qu, Z.; Xiong, Y.; Anisotropic anomalous Hall effect in triangular itinerant ferromagnet Fe_3GeTe_2. *Phys. Rev. B* **2017,** *96,* 134428.

[18]   Yi, J.; Zhuang, H.; Zou, Q.; Wu, Z.; Cao, G.; Tang, S.; Calder, S. A.; Kent, P. R. C.; Mandrus, D.; Gai, Z.; Competing antiferromagnetism in a quasi-2D itinerant ferromagnet: Fe_3GeTe_2. *2D Mater.* **2017,** *4,* 011005.

[19]   Tan, C.; Lee, J.; Jung, S.; Park, T.; Albarakati, S.; Partridge, J.; Field, M. R.; McCulloch, D. G.; Wang, L.; Lee, C.; Hard magnet properties in nanoflake van der Waals Fe_3GeTe_2. *Nat. Commum.* **2018,** *9,* 1554.

[20]   Zhang, X.; Zhao, Y.; Song, Q.; Jia, S.; Shi, J.; Han, W.; Magnetic anisotropy of the single-crystalline ferromagnetic insulator $Cr_2Ge_2Te_6$. *Jpn. J. Appl. Phys. Part 1,* **2016**, *55,* 033001.

[21]   Garello, K.; Miron, I. M.; Avci, C. O.; Freimuth, F.; Mokrousov, Y.; Blugel, S.; Auffret, S.; Boulle, O.; Gaudin, G.; Gambardella P.; Symmetry and magnitude of spin-orbit torques in ferromagnetic heterostructures. *Nat. Nanotechnol.* **2013,** *8,* 587.

[22]   Avci, C. O.; Garello, K.; Gabureac, M.; Ghosh, A.; Fuhrer, A.; Alvarado, S. F.; Gambardella, P.; Interplay of spin-orbit torque and thermoelectric effects in ferromagnet/normal-metal bilayers. *Phys. Rev. B.* **2014,** *90,* 224427.

[23]   Avci, C. O.; Quindeau, A.; Pai, C.; Mann, M.; Caretta, L.; Tang, A. S.; Onbasli, M. C.; Ross. C. A.; Beach, G. S. D.; Current-induced switching in a magnetic insulator. *Nat. Mater.* **2017,** *16,* 309.

[24]   Pai, C.; Mann, M.; Tan, A. J.; Beach, G. S. D.; Determination of spin torque efficiencies in heterostructures with perpendicular magnetic anisotropy. *Phys. Rev. B* **2016,** *93,* 144409.

Chapter 4   Probing the Antiferromagnetic Ordering of the Proximate Kitaev Quantum Spin Liquid Candidate RuCl₃

4.1   Motivation

$RuCl_3$, a layered van der Waals antiferromagnetic (AFM) insulator, has garnered a lot of interest in the field of two-dimensional material research due to its status as a Kitaev quantum spin liquid (KQSL) candidate. Below its Néel temperature, $T_N \sim 7$ K-14 K, $RuCl_3$ exhibits properties of a KQSL when its time reversal symmetry is broken by a strong external magnetic field applied parallel to its crystal plane. This has implications which are of great interest as it is predicted that the excitations of the KQSL are Majorana fermions making $RuCl_3$ a great system for studying these fractional excitations [1]. This state has been probed by neutron scattering, specific heat measurements, and thermal Hall effect measurements to name a few, in search of its KQSL properties as well as for evidence of Majorana fermions[2-4]. We report our results of spin Hall magnetoresistance (SMR) measurements which probe the antiferromagnetic (AFM) state of this interesting two-dimensional material in search of spin transport signatures of the field induced KQSL phase of $RuCl_3$.

4.2   Introduction

In this study we performed electronic transport measurements in $RuCl_3$/Pt heterostructures consisting of thin (10 nm – 50 nm) exfoliated flakes of $RuCl_3$ with both 2 nm and 5 nm sputtered Pt. From measurements of longitudinal resistivity vs. temperature we saw a significant enhancement of the low temperature resistivity in these

heterostructures compared to devices with Pt of similar thickness on a Si/SiO$_2$ substrate. We attribute the enhanced resistivity to the spin-dependent scattering at the interface between RuCl$_3$ and Pt along with the additional contribution from SMR in addition to the positive MR from the Pt layer. These results also confirmed the RuCl$_3$ flakes to be in intimate contact to the Pt films by looking at the difference in the temperature dependence of the resistivity in the cooling versus the heating cycles which show a clear strain induced hysteresis in the ~ 30K to 180K temperature range following temperature dependence of its thermal expansion coefficient [5].

Although no transport signature of the KQSL phase was realized in our measurements, we were able to probe the AFM order of RuCl$_3$ with our low temperature magneto-transport measurements. Through our transverse resistance measurements acquired with a field swept in the direction parallel to the injected current we detected a large signal which is due to the AFM spins as they rotate away from their anti-aligned ground state to a state in which all the spins were aligned with the applied field at which point the acquired signal was saturated. This signal was only present at temperatures below T$_N$ indicating that the AFM ordering in RuCl$_3$ was the responsible for the signal.

The acquired transverse resistance is strongly dependent on magnitude of the injected current density which suggests that the spin-orbit torque from the Pt layer actinf on the magnetization of RuCl$_3$ is responsible for this dynamical response [6]. These result show RuCl$_3$ coupled to Pt thin films to be an excellent system to study physics of the spin Hall effect in two-dimensional material systems.

4.3 Magnetic and Transport Properties of Bulk and Exfoliated Thin Flakes of RuCl$_3$

4.3.1 Magnetic and Structural Properties of Bulk RuCl$_3$

RuCl$_3$ is a low temperature two-dimensional AFM with its layers held together by a weak van der Waals interaction. Each layer forms a nearly perfect honeycomb structure with very small in-plane distortion of less than 0.2% [7]. For crystals which exhibit no signs of stacking faults, the crystal structure is the single layer unit cell monoclinic structure which stays consistent from room temperature down to the lowest measured temperature. Most x-ray measurements that have been performed on RuCl$_3$ were performed on crystals or powders which exhibit stacking faults which arise with ease due to its very weak van der Waals bond in which case the room temperature structure is triangular remaing in this phase until it undergoes a structural phase transition at ~ 150 K. The exact temperature of this transition depends on whether the crystal is being cooled or warmed through this transition as well as the abundance of the stacking faults in the measured sample [7,8]. There exist two possible stacking orders for RuCl$_3$ layers: the ABC-stacking and the ABAB-stacking, illustrated in figure 4.1 (a), and in almost all measured samples reported in literature, both stacking orders coexist throughout the crystals. The most energetically favorable stacking is the ABC-stacking which yields an AFM ordering of T_N = 7K determined through magnetic susceptibility measurements [7].

The low temperature spin configuration of RuCl$_3$, as is illustrated in figure 4.1 (b), is an in-plane spiral AFM with the spins rotated by an angle of 120⁰ for successive layers

and are oriented within the ac-plane. Also, within each layer the spins make an angle of $\pm35^\circ$ relative to the ab-plane.
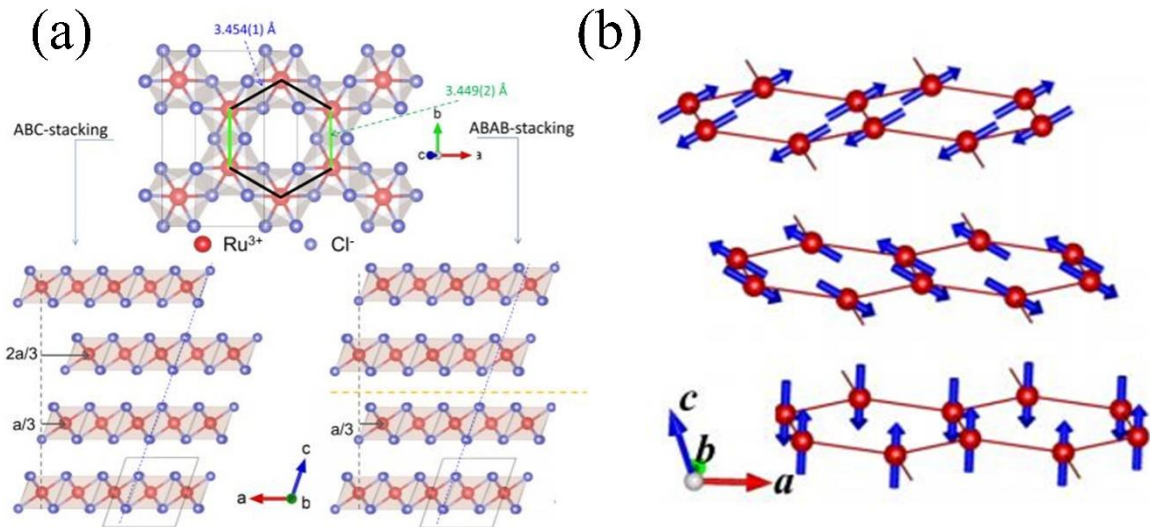
Figure 4.1. Crystal and AFM Spin Configuration of RuCl₃. (a) Atomic alignment in RuCl₃ crystal layers showing its near perfect honeycomb nature. Below are the two possible stacking configurations, ABCA-stacking and ABAB- stacking. (b) The low-temperature AFM spin configuration of RuCl₃. The in-plane spin structure is a zigzag AFM state while out-of-plane the spins are rotated by 120° in successive layers with the spins lying in the ac-plane and at an angle of $\pm35^\circ$ to the ab-plane. Adapted from H. B. Cao, et al. Low-temperature crystal and magnetic structure of α-RuCl₃. Phys. Rev. B. **93**, 134423 (2016).

Multiple measurements of the heat capacity have been performed on RuCl₃ crystals and powder [2,7,8] with inconsistent results of its low temperature structure and AFM ordering temperature. Reference [7] performed a systematic study of the heat capacity of RuCl₃ to accurately determine the source of these inconsistencies by measuring the heat capacity of an as grown crystal without any stacking faults and then remeasuring the same crystal multiple times after manually deforming it between successive measurements. They

also measured a powder sample to compare with their crystal results as well. Their results, depicted in figure 4.2 (a), shows the heat capacity for an as-grown crystal which has a single well-defined peak at T = 7 K, indicating a single magnetic phase transition at this temperature consistent with the ABC-stacking. Next, they mechanically deform the crystal through a process of bending the crystal, repeating this process after each measurement. These results are presented in the lower panel of figure 4.2 (b), ordered 1-4, where 1 is the least deformed, then increasing in the extent of deformation through 4 which is the result obtained from a powder sample. The trend starts with 1 showing a decreased intensity and broadening of the 7 K AFM transition peak and a very small, broad peak beginning to develop at T ~ 14 K which is the AFM transition associated with the ABAB-stacking order. Next, upon further deformation the 7 K peak shifts and becomes much less prominent while the 14 K peak develops further. After their final deformation step, curve 3 shows a complete suppression of the 7 K peak while the broad 14 K peak becomes the only dominate feature in the data set, and while there are some differences, this curve is very similar to curve 4 taken from the powder sample.
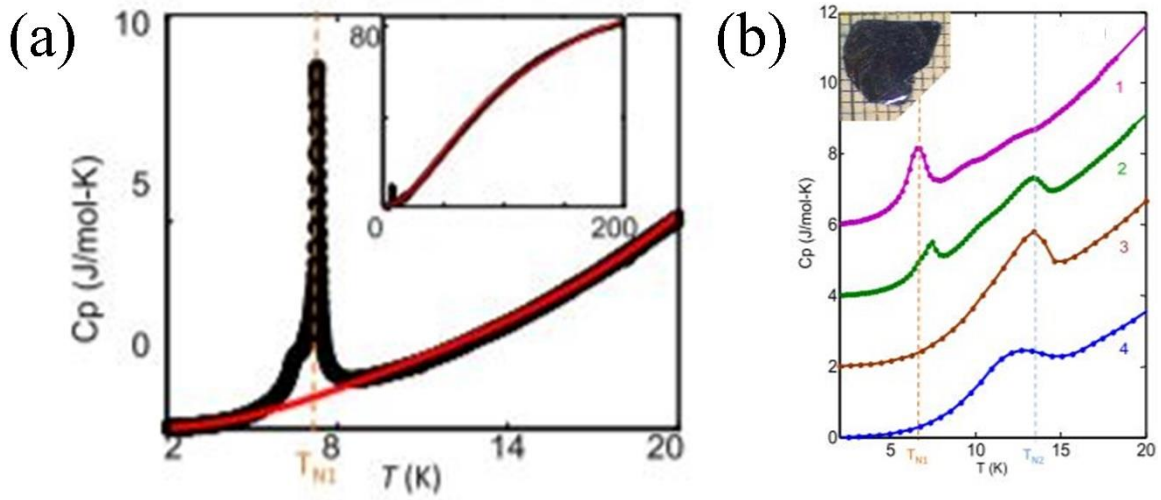
Figure 4.2. Heat Capacity Measurements of RuCl₃ Crystal and Powder. (a) Heat capacity vs. temperature of as grown RuCl₃ bulk crystal which shows no sign of any stacking faults. (b) 1-3 are heat capacity results of the same crystal in (a) after successively mechanically deforming the crystal in between each measurement to purposely introduce an increasing number of stacking faults. 4 is the heat capacity results obtained from a powders sample of RuCl₃. Adapted from H. B. Cao, et al. Low-temperature crystal and magnetic structure of α-RuCl₃. Phys. Rev. B. **93**, 134423 (2016).

4.3.2   Transport Properties of Bulk and Thin Flakes of RuCl₃

RuCl₃ is a narrow gap semiconductor with a band gap, $E_g \approx 0.25eV$, determined through STS measurements of a bulk sample [9]. At room temperature bulk and thin flake devices of RuCl₃ are conductive, and, with proper fabrication techniques, they exhibit low contact resistance with Ohmic I-V characteristics and relatively low four-terminal longitudinal resistance [10]. Figure 4.3 (a) shows the linear I-V curves obtained from a thin flake device measured in reference [10]. They also measured the resistance vs. temperature for devices which varied in thickness from 7 nm – 50 nm as shown in figure 4.3 (b). These plots reveal insulating behavior which follow a thermal activation model from room temperature down to ~ 200 K at which variable range hopping with n = 2 dominates as the temperature is lowered further causing the resistance to rapidly rise until a temperature

<100 K at which the authors were unable to measure further due to the extremely large resistivity below this temperature. The temperature at which the resistivity versus temperature switches from thermal activation to variable range hopping is plotted against the flake thickness in the inset of figure 4.3 (b) which shows that this transition occurs around T $\approx$ 170 K – 180 K.
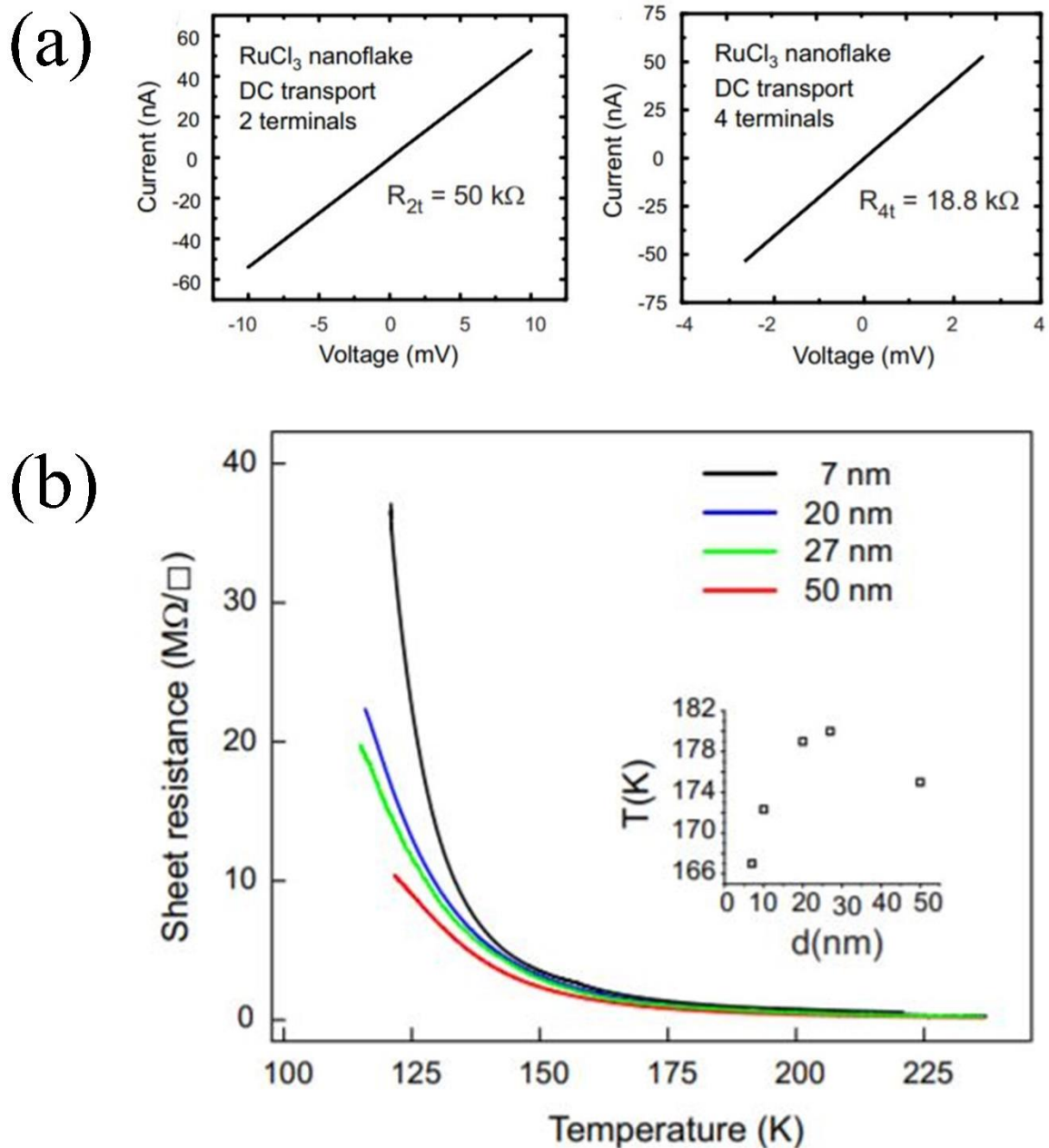
Figure 4.3. Electronic Transport Measurements in RuCl₃ Thin Flakes. (a) 2-termianl and 4-terminal I-V curves for a think flake RuCl₃ device at room temperature showing Ohmic behavior with relatively low resistance. (b) R vs. T measurement for RuCl₃ devices of thickness which vary from 7nm to 50nm. Inset is the variable range hopping transition plotted vs. the flake thickness. Adapted from S. Mashhadi, et al. Electrical transport signature of the magnetic fluctuation-structure relation in α-RuCl₃ nanoflakes. Nano. Lett. 18, 3203-3208 (2018).

4.4 Fabrication of RuCl₃/Pt Heterostructures

To fabricate the RuCl₃/Pt heterostructures, we developed a technique that minimizes the time that the flakes were exposed to ambient conditions without a capping layer. Also, this process was developed to ensure that the RuCl₃ flakes would not have to be in contact with acetone as RuCl₃ is known to quickly degrade when it is emerged in an acetone bath [10].

The process begins by mechanical exfoliation of RuCl₃ thin flakes from a bulk crystal using the scotch tape method in an argon filled glovebox with <1pmm O_2 and H_2O. The scotch tape with RuCl₃ flakes was placed onto the surface of Si/SiO₂ wafer which were put to rest on a hotplate at 100 ⁰C. After 2 minutes they were removed from the hotplate and set aside to cool for at least 5 minutes. Once cooled the tape is slowly removed from the wafer's surface leaving behind the RuCl₃ thin flakes which range in thickness from 100's of nm down to the monolayer limit. Due to the very weak interlayer van der Waals bond of RuCl₃, it exfoliates very easily leaving behind flakes which can be as larger than 100μm×100μm although the monolayer flakes tend to be much smaller. The wafers are then taped by their backside onto a larger SiO₂ wafer which is sealed in a vacuum bag and removed from the glovebox.

The second step of the process is the Pt deposition in a sputtering system. For this step the load lock of the sputtering chamber was vented and once it reached air pressure the vacuum sealed bag with the RuCl₃ thin flake samples was opened and the large SiO₂ wafer they were taped to was quickly placed into the load lock. The load lock is then evacuated of air before the samples are moved into the main chamber which is at a base

pressure of 2×10^{-7} Torr. The Pt is then deposited using a low sputtering power of 0.375W at an argon pressure of 5×10^{-3} Torr. Both 5nm and 2nm Pt thin films were deposited on $RuCl_3$ for the devices measured for this experiment. After the Pt is deposited on the flakes, they are removed from the chamber and at this point the $RuCl_3$ is protected from the air and moisture by the Pt capping layer for the remainder of the fabrication.

The third step begins with examining the films under optical microscope to identify a flake that meets the criteria that it is uniform in thickness, flat, and large enough for device fabrication. Then the wafer was spin coated with MMA/PMMA bilayer resist. Since exposure to high temperatures can cause the $RuCl_3$ flakes to degrade, the curing temperature of the resist layers was reduced from the usual 180 ⁰C to 100 ⁰C which reduces the resolution of the patterns, yet still enables the e-beam lithography (EBL) patterns to be produced. The wafers would then be patterned by EBL to define electrodes to the $RuCl_3$/Pt heterostructures and then 100 nm/10 nm Au/Ti was deposited via e-beam evaporation following the pattern development. At this point the $RuCl_3$ is still completely covered by the Pt layer; Thus, the liftoff process in acetone did not degrade the flake as it otherwise would.

The next step is defining a Hall bar structure with the heterostructure. After EBL and subsequent development, 30nm Al_2O_3 is deposited by e-beam evaporation to the defined Hall bar region to create a hard mask over the device. Once the final liftoff process is completed, the wafer is etched with argon plasma in an inductively coupled plasma chamber. After this step only the electrodes, Hall bar and the unetched remains of thick $RuCl_3$ flakes stay on the Si/SiO_2 wafer. Most importantly all of the Pt on the SiO_2 surface,

except for the desired Pt in the Hall bar region will be removed. One of the devices measured for this experiment is pictured in figure 4.4, with the inset image illustrating the material layers in the Hall bar region.
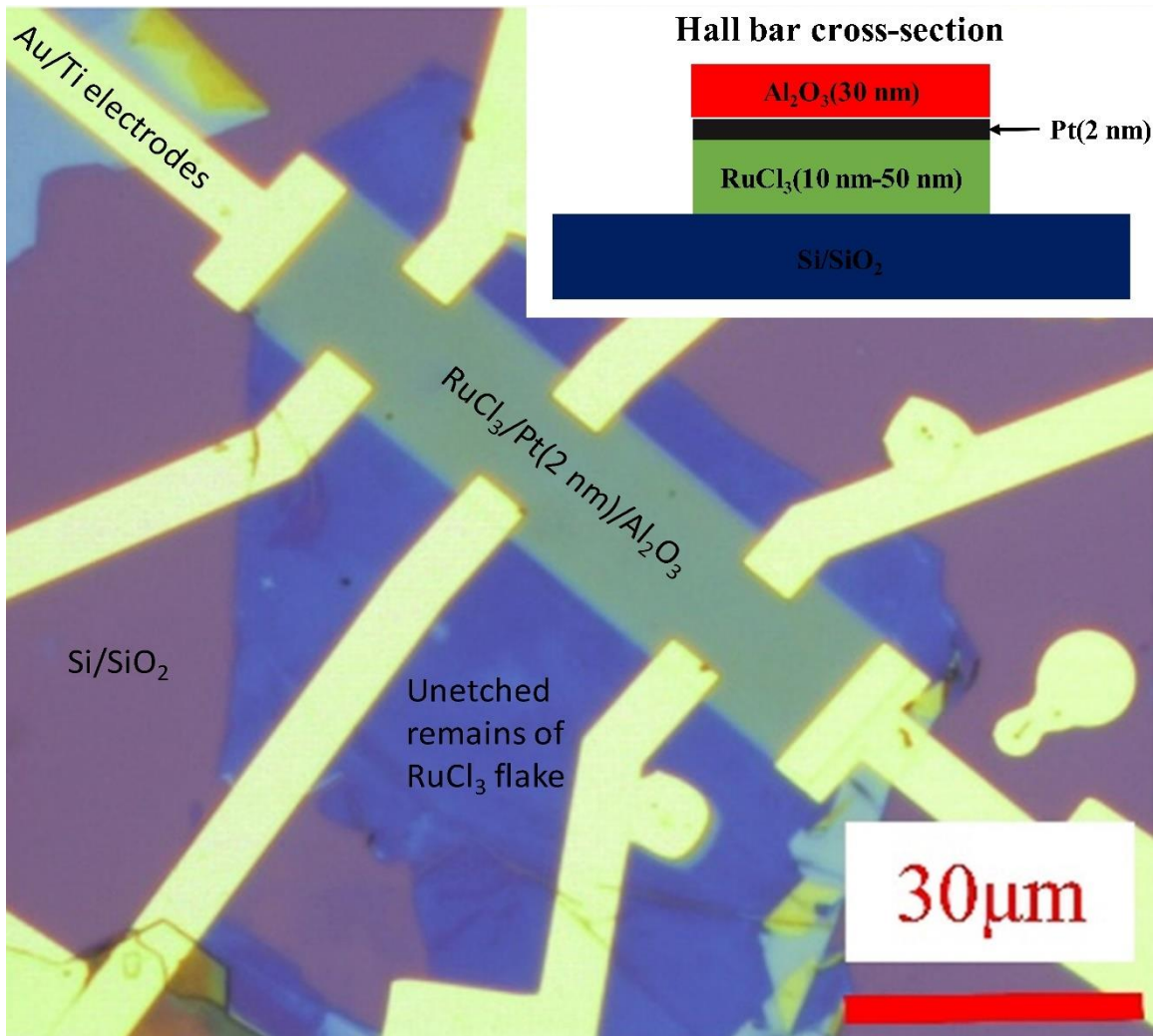
Figure 4.4. Image of Representative RuCl₃/Pt. Optical microscope image of a representative device used for the measurements in this study with a scale bar in the bottom right of the image.

4.5   Electronic Transport in RuCl$_3$/Pt Heterostructures

4.5.1   Resistivity Versus Temperature for RuCl$_3$/Pt Heterostructures with 2 nm and 5 nm Pt

Electric transport measurements were performed on many RuCl$_3$/Pt(5 nm) and RuCl$_3$/Pt(2 nm) devices as well as 2 nm and 5 nm Pt control devices in a Quantum Design physical properties measurement system. While the system was cooled from room temperature down to the base temperature of 1.6 K, we monitored the resistivity as a function of temperature with a fixed DC current ranging from 10 µA for narrow channel devices up to 100 µA for devices with the widest channels. Figure 4.5 shows the results obtained in representative devices of each type measured.

The graphs on the bottom row were obtained from devices with 5nm Pt with, (3), obtained from the Pt control device and, (4), from the RuCl$_3$/Pt heterostructure device. The temperature axis is plotted in logarithmic scale to accentuate the low temperature regime of resistivity. For the control device, the behavior is as expected for thin film Pt devices with the resistivity decreasing with temperature until the signal saturates at T ~ 25K. As for the heterostructure device it shows a similar trend at high temperatures, but instead of the signal saturating at low T, the resistivity experiences a slight upward trend at T ~ 15K which is close to the reported 14 K Néel temperature for ABAB-stacked RuCl$_3$. This enhancement of the resistivity which is only present for the heterostructure devices may arise from increased scattering in the surface layer of Pt due to the presence of magnetic impurities.

The top row of graphs was obtained from the devices with 5 nm Pt thin films. The data in, (1), was acquired from the 2 nm Pt control device which shows metallic behavior similar to 5 nm Pt except that the resistivity is almost an order of magnitude larger and the change in resistivity from its room temperature value is much less for 2 nm Pt than it was in the 5 nm Pt film. Also, instead of the resistivity just saturating below 25 K it begins to increase slightly as the temperature is lowered below ~20 K due to dimensional effects for very thin Pt films [11]. Unlike the minor difference between the 5 nm Pt control device and the RuCl$_3$/Pt(5 nm) heterostructure devices, the 2 nm Pt control device and RuCl$_3$/Pt(2 nm) device show stark differences in their resistivity versus temperature behavior. The RuCl$_3$/Pt(2 nm) heterostructure shows insulating behavior from room temperature down to ~ 180K at which point the expected metallic behavior is restored. This is due to current shunting into the relatively low resistivity RuCl$_3$ at higher temperatures. Once the temperature reaches T ~180 K, about the temperature at which the variable range hopping mechanism for RuCl$_3$ dominates its transport, current shunting away from the Pt ceases to occur as the resistivity of RuCl$_3$ rapidly increases around this point. The metallic behavior continues until T ~ 45 K at which point insulating behavior returns and the resistivity begins to increase slightly until T ~ 15 K where the resistivity begins to rapidly increase roughly linearly as a function of Log(T). This behavior suggests that the Kondo effect may be the mechanism responsible for this behavior although further investigation would be required to determine the source of this low temperature resistivity increase [12].

This graph includes the resistivity behavior when a 140 kOe magnetic field is applied in the crystal plane parallel to the injected current and perpendicular to the crystal

plane. These results show a large positive magnetoresistance for both orientations of the external magnetic field with only a slightly larger value when the field is oriented perpendicular versus parallel to the crystal plane for temperatures above ~25 K. This magnetoresistance is most prominent for temperatures below the 14 K Néel temperature of $RuCl_3$ which suggests that the dominant mechanism is magnetic impurity scattering at the Pt-$RuCl_3$ interface. The positive MR in our longitudinal resistance measurements may also arise from magnetic ordering induced in Pt through proximity magnetic exchange coupling leading to anisotropic magnetoresistance [13].

The inset of (2) in figure 4.5 is the zero-field resistivity versus temperature taken during the cooling (black curve) and warming (red curve) processes for temperatures between T = 190K and T = 30K. This shows a hysteresis in the resistivity measured during these two cycles which suggests that the $RuCl_3$ undergoes a structural transition at T ~ 170K. from this result we can conclude that the $RuCl_3$ flakes used in our heterostructures include stacking faults likely as a result of the exfoliation process as seen in other experiments with exfoliated thin flakes of $RuCl_3$. This also gives evidence that $T_N = 14$ K is t be expected for these heterostructure devices.
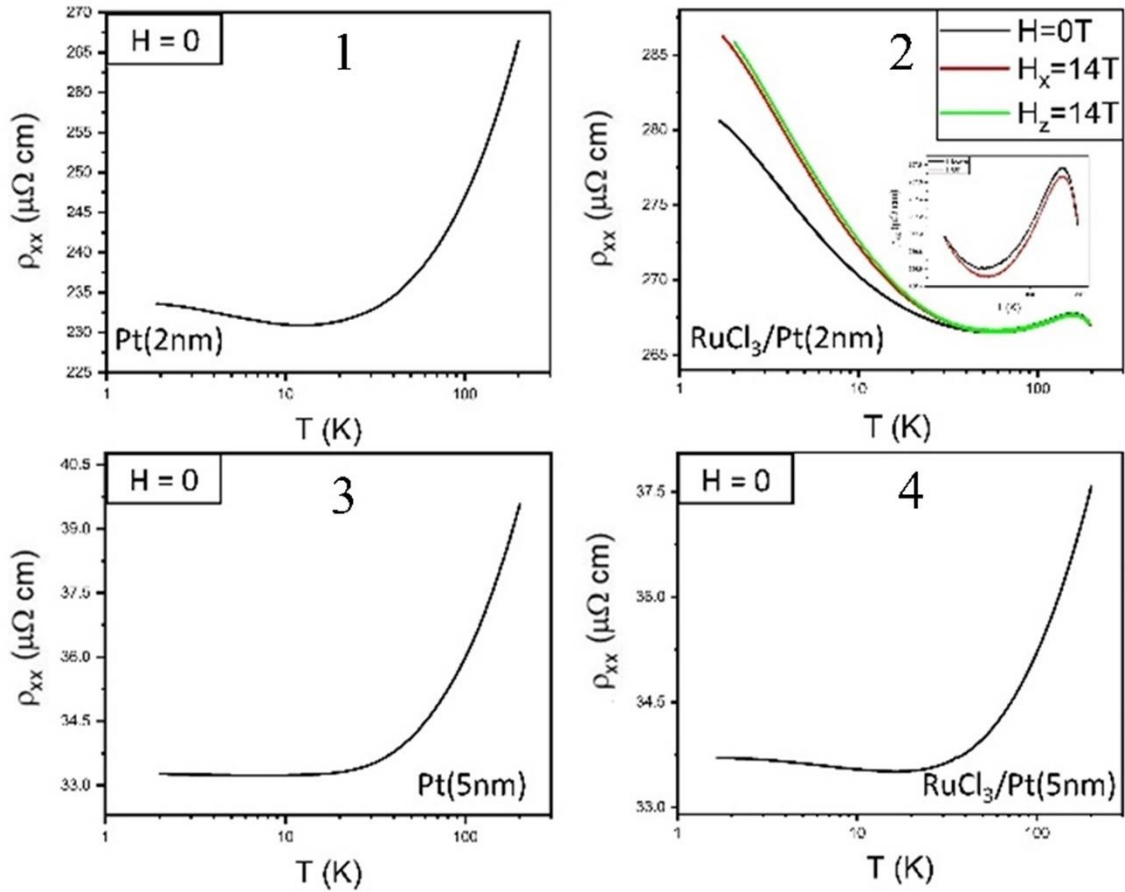
Figure 4.5. Device Resistivity Versus Temperature Measurement Results. Resistivity versus temperature in: (1) Pt(2 nm) for H = 0, (2) $RuCl_3$/Pt(2 nm) with H = 0, H_x = 140 kOe, and H_z = 140 kOe with inset the H=0 data upon the warning and cooling cycles for 30 K < T < 190 K, (3) Pt(5 nm) with H = 0, and (4) $RuCl_3$/Pt(5 nm) with H = 0.

4.5.2 Magnetoresistance in $RuCl_3$/Pt Heterostructures

We performed magnetoresistance (MR) measurements at T = 2 K for 2 nm and 5 nm Pt control devices and $RuCl_3$/Pt heterostructure devices sweeping an external field parallel and perpendicular to the crystal plane from -130kOe ≤ H ≤ 130kOe. The results are displayed in figure 4.6. Figure 4.6 (a) are the results acquired from the 2nm Pt control device and $RuCl_3$/Pt(2nm) heterostructure device plotted together to compare the MR in

the heterostructure to the Pt thin film. The most striking feature between the 2 nm Pt control device and the $RuCl_3$/Pt(2 nm) device is the enhanced positive MR in the heterostructure device which was expected from the comparison of the resistivity versus temperature with and without applied fields in figure 4.5 (2). Also, the for an in-plane field the signal begins to saturate around 50kOe to 60kOe in the heterostructure devices as can be seen from the curvature of its MR signal. This saturation is seen clearest when a second-order derivative of the data is performed as shown in the inset of figure 4.6 (a) where the red curve corresponds to the $RuCl_3$/Pt heterostructure and the black curve for the Pt control device. The red curve shows a positive value for Hx < 50kOe then goes to zero for H_x > ~50kOe although the signal to noise generated from the differentiation process makes it difficult to determine the exact value at which this value goes to zero. This contrasts with the black curve where the signal stays at zero except for in a narrow field window around $H_x = 0$ which comes from the minimum in its MR. This saturation in the heterostructure device showing up for H_x > 50kOe when it is not seen in the Pt control device suggests that the Pt layer senses the anti-ferromagnetism (AFM) in the underlying $RuCl_3$ since the AFM spins in $RuCl_3$ will completely align with the field for an in-plane external field $H_x \approx 50$kOe [3].
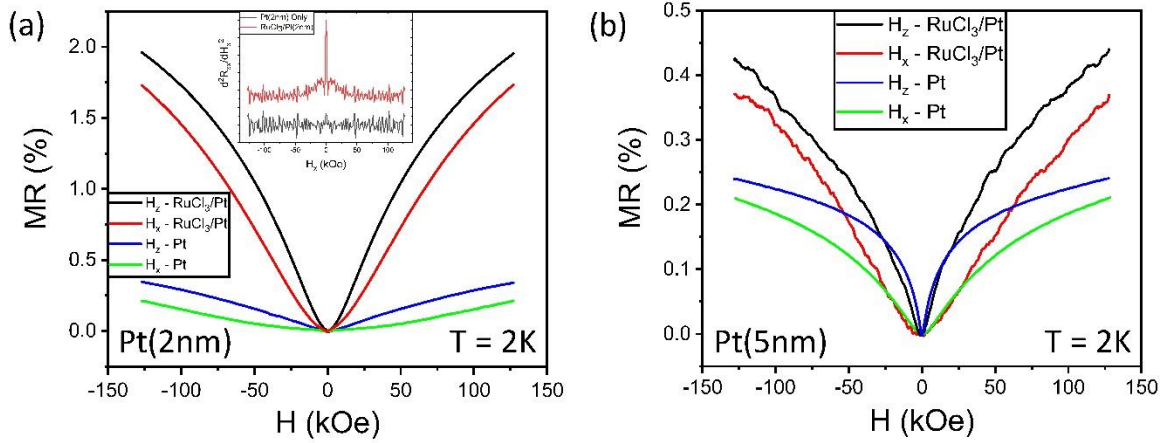
Figure 4.6. Magnetoresistance in RuCl₃/Pt Heterostructures. (a) MR in RuCl$_3$/Pt(2 nm) and Pt(2 nm) thin films with both in-plane and out-of-plane external magnetic fields. Inset is the second derivative of the MR for an in-plane magnetic field from both kinds of devices to highlight the saturation in the RuCl$_3$/Pt corresponding to the magnetic ordering field of RuCl$_3$ which in not present in the Pt only device. (b) MR in RuCl$_3$/Pt(2 nm) and Pt(2 nm) thin films with both in-plane and out-of-plane external magnetic fields.

For the heterostructure devices with 5 nm Pt thin films the differences observed in their signal in comparison to the signal from 5 nm Pt control devices are not nearly as dramatic as it was for 2nm Pt films as can be seen it figure 4.6(b). In these devices the signal for RuCl$_3$/Pt is less than twice as large as in the Pt only devices as opposed to the 2 nm devices where the difference between the heterostructure devices and the Pt control devices is up to 8 times larger for the RuCl$_3$/Pt devices. We also note the clear weak anti-localization signal in the 5 nm Pt control devices that is not present in the nearly parabolic signal obtained from the 2 nm Pt control device. We suspect that the scattering between the electrons in Pt and the phonons from the SiO$_2$ substrate is enhanced in the thinner films which increases dephasing and suppresses any quantum corrections to the zero field resistance. Due to most of the measured signal in the heterostructure devices coming from the Pt that is unaffected by the underlying RuCl$_3$ flake, it is difficult to discern the signal

that is acquired in the Pt from its proximity to the underlying RuCl$_3$, so for the rest of this study we focused on the devices comprised of 2 nm Pt.

4.5.3. Hall Effect Measurements in RuCl$_3$/Pt(2 nm) Devices

While measuring the MR in our RuCl$_3$/Pt(2 nm) devices, we also monitored the transverse resistance in our devices at the same time. In all the devices that were measured the transverse resistance was strongly mixed with the longitudinal resistance such that the largest signal present in the transverse channel was an overall symmetric signal, yet it was much different than the signal acquired in the longitudinal channel. In figure 4.7 (a), the transverse resistance obtained in response to an in-plane applied magnetic field is plotted for a set of currents applied from the source to drain at a fixed system temperature of T = 1.6 K. It's given as the change in resistance, $\Delta R_{yx} = R_{yx}(H) - R_{yx}(120\text{ kOe})$, for presentation purposes to clearly show the change in its signal as the current is increased in the device.

For large in-plane magnetic fields at relatively small currents, ΔR_{yx} displayed in figure 4.7 (a) resembles the signal measured in R_{xx}, figure 4.7 (b), but ΔR_{yx} shows much different behavior in the field range -50 kOe $\leq$ H $\leq$ 50 kOe. For this low field region there are minima in ΔR_{yx} leading to a zero-field peak which are never seen the data acquired in R_{xx}. First off, we note that this zero-field resistance maximum cannot be due to a quantum correction to the resistance such as weak localization since the field is applied parallel to the applied current which would not result in such a field response. Therefore, we attribute this in-plane field response to the AFM order in the underlying RuCl$_3$ imprinted in the Pt layer's transport properties as its spins align with the external field. Since this additional

signal is symmetric with respect the to the field, the anomalous Hall effect is not its source, but it may be generated from the spin Hall magnetoresistance detected through the ISHE in the Pt layer or from AMR due to MPE. We suspect that this response does not show up in the R_{xx} results because the multiple domains sensed by this measurement. R_{xx} is measured over a much larger distance than the signal that mixes into the transverse resistance measurement which can cause cancelations which average this signal out. Also, the coupling between Pt and $RuCl_3$ can vary across the length of the device causing some regions of the devices to not sense the $RuCl_3$. Out of all of the devices measured only two of the Hall bar pairs that we measured for this study did not exhibit a similar signal and in none of the devices did this signal appear in the R_{xx} signal.

While this data is complicated by the Joule heating along with the low Néel temperature of $RuCl_3$, the current dependent behavior of this signal is very interesting. The legend above the ΔR_{yx} plot in figure 4.7 (a) gives the magnitude of the applied current corresponding to the different curves and the legend above the R_{xx} plot in figure 4.7 (b) gives the corresponding value of the effective sample temperature, T^*, which is determined from comparing the magnitude of $R_{xx}(0)$ with the resistance versus temperature measured with the smallest applied current, $I = 5$ µA. Since we had the expectation that the temperature of the Pt layer which T^* tracks will be the same as the temperature of the surface of the $RuCl_3$ flake, we believe T^* accurately tracked the temperature of the flake during the experiment. From the trend of increasing current, it is clear that the low field signal corresponding to the AFM state increases in magnitude with increasing current even though the overall vales of R_{yx} decreases. Therefore, this cannot be due to the decrease of

96

the R_{xx} signal from the rise in the Pt temperature from Joule heating. This is clear since the decrease in magnitude of R_{xx} is much smaller than the increase in magnitude of the low field feature in R_{yx}. As the current in the device increases, the high field data of ΔR_{yx} eventually changes from negative to positive with respect to the high field background for currents, $I \geq 0.08$ mA. This corresponds to the effective temperature, $T^* \geq 8$ K, which is just above the Néel temperature, $T_{N1} = 7$ K, for RuCl$_3$ with ABAB-stacking order although the signal still increases for even larger current and retains the same overall features. This growth in magnitude continues with concave curvature up to the current, $I = 0.1$ mA, and then its curvature changes to convex for currents, $I \geq 0.2$ mA, which corresponds to, $T^* \geq$ 15.5K. For currents larger than 0.2mA, ΔR_{yx} decreases in magnitude with an inverse parabolic curvature which suggests paramagnetic behavior as has been reported in previous studies of paramagnetic insulator/Pt heterostructures [14]. This is to be expected since the effective temperature is above the highest Néel temperature, $T_{N2} = 14$ K, corresponding to the ABC-stacking order.

To remove the contribution to ΔR_{yx} from the MR in Pt, we change the data from R_{xx} to ΔR_{xx} and scaled it such that the high field matched with the high field data of ΔR_{yx} for the smallest current we measured at, $I = 0.005$ mA. To obtain the best matching between the two sets of data we had to divide ΔR_{xx} by $2.3*R_{xx}(0)/R_{yx}(0)$. The inset of figure 4.7 (a) has ΔR_{yx} and $\dfrac{\Delta R_{xx}}{\left(2.3 \times {\Delta R_{xx}(0)}/{\Delta R_{yx}(0)}\right)}$ plotted together to illustrate this high field matching of the two curves. We then applied this same scale factor to ΔR_{xx} for each current magnitude and subtracted each from the corresponding ΔR_{yx} data. The results from this are presented in figure 4.8 (c). This clearly shows that the saturation of the additional low field signal

acquired in the R_{yx} data corresponds to the spin saturation of RuCl$_3$ crystals serving as another conformation that the spin state of RuCl$_3$ is responsible for the signal we obtained in our measurements.
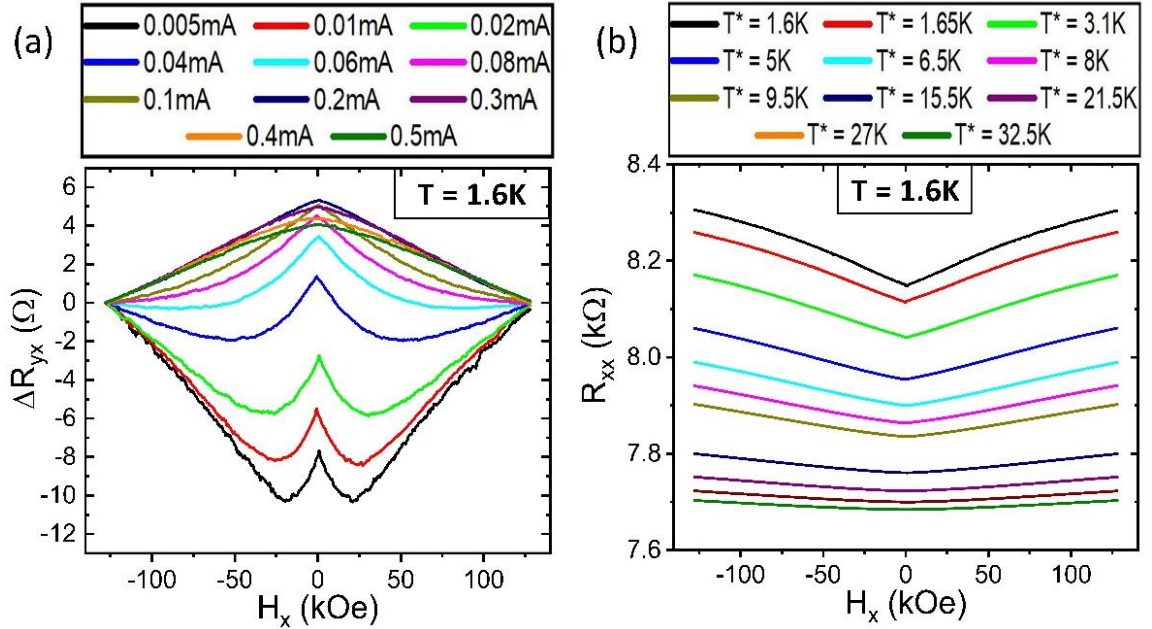
Figure 4.7. Current Dependence of the Transverse and Longitudinal Resistance at T = 1.6 K. (a) $\Delta R_{yx} = R_{yx}(H) - R_{yx}(120 \text{ kOe})$ as a function of the applied in-plane magnetic field for currents ranging from 0.005 mA to 0.5 mA. (b) R_{xx} as a function of the applied in-plane magnetic field for currents ranging from 0.005 mA to 0.5 mA. Above the graph in (a) is the legend which correlates the plot color to the magnitude of the injected current and (b) is the legend correlates the plot color to the effective temperature due to Joule heating determined by comparing $R_{xx}(0)$ to the resistance versus temperature obtained with I = 0.005 mA.

To confirm the dynamical response of the low-field signal acquired in our measurements of R_{yx}, we performed measurements of this device at different system temperatures with different fixed currents. Figure 4.8 (a) shows the results we obtained for the fixed current, I = 0.01 mA. With this small current this signal appears only for the lowest system temperature, T = 1.6 K, we measured. The data for T = 5 K shows a very small bump at H = 0, but it's too small to confirm it to be the low-field signal and not just an artifact in the measurement without several measurements to confirm it to be a true signal. Following the same procedure for a larger current, I= 0.05 mA, we see this feature persist up to a larger system temperature, T > 7.5K, as shown in figure 4.8 (b), but it does not persist up to, T = 10K. Also, as the temperature is increased, ΔR_{yx} decreases in magnitude, yet never becomes negative even though the negative ΔR_{yx} will persist up to a system temperature, T > 30 K, when the current in the device is fixed at 0.5 mA. This suggests that a sufficiently large current is required to generate enough spin orbit torque generate this dynamical response which is detected in the Pt layer.
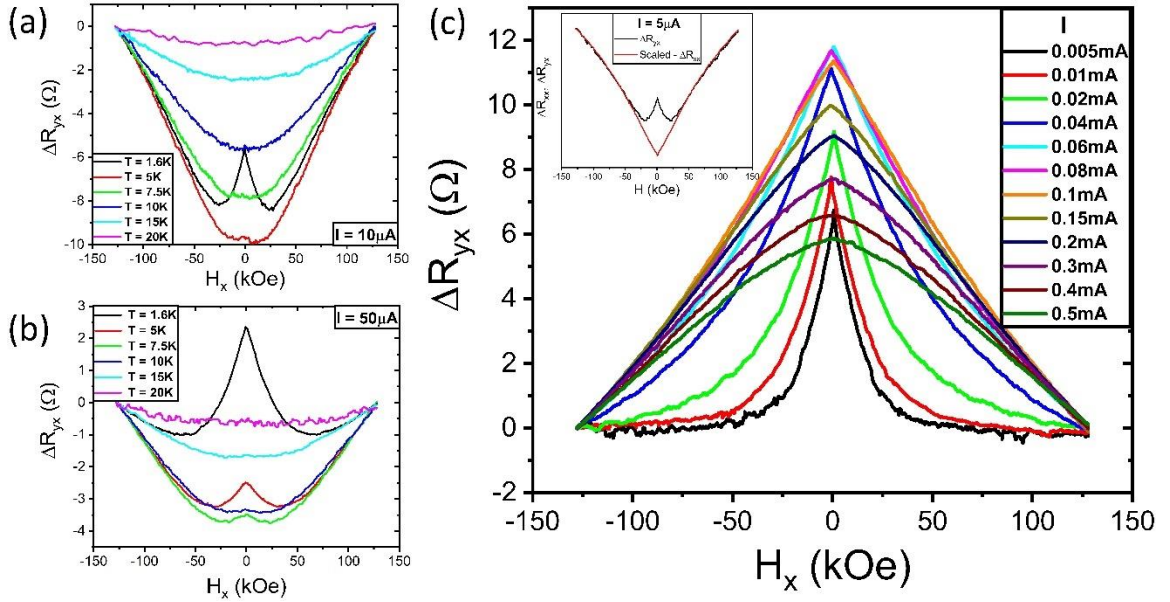
Figure 4.8. Temperature Dependence of ΔR_{yx} with Fixed Current and Magnetization Signal in ΔR_{yx} with MR from Pt Removed. (a) ΔR_{yx} measured at different system temperatures for I = 0.01 mA. (b) ΔR_{yx} measured at different system temperatures for I = 0.05 mA. (c) Magnetic signal of ΔR_{yx} after subtracting the scaled value of ΔR_{xx} for each current magnitude with ΔR_{yx} and scaled ΔR_{xx} for the fixed current I = 0.005 mA plotted together in the inset graph to show the best match obtained from the scaling.

4.6   Summary

In conclusion, we were able to probe the antiferromagnetic ordering in exfoliated thin flakes of the Mott insulator $RuCl_3$ through the first ever electronic transport measurements performed below its Néel temperature. The measurements were conducted in $RuCl_3$/Pt(2nm) heterostructures successfully fabricated with a technique we developed specifically to overcome the challenges with of the degradation of $RuCl_3$ through traditional device fabrication methods. The use of 2nm Pt thin films coupled to the surface of the $RuCl_3$ thin flakes allowed us to leverage the large spin orbit coupling in Pt to observe an anomaly in the transverse resistance in the Pt layer arising from the AFM state.

We tracked the signal of the AFM ordering in Pt up to, $T_N = 14$ K, indicating the coexistence on the ABAB-stacking and ABC-stacking orders of $RuCl_3$ due to stacking faults which normally occur through the exfoliation process of the thin flakes of $RuCl_3$. We were also able to probe the paramagnetic state which occurs above the Néel temperature in our high current measurements. A dynamical response to the injected current most likely due to the spin orbit torque acting on the magnetization of $RuCl_3$ by the spin current injected by the Pt layer was observed in our measurements.

4.7   Discussion

To conclusively determine the physical origin of the proximity induced AFM signal in our transverse resistance measurement more measurements will be required. The physical origin of the signal we acquired in our measurements can come from one or most likely a coexistence of both of the following mechanisms: spin Hall magnetoresistance (SMR) [6], which arises from spin current injected from the Pt layer into the $RuCl_3$ flake, and/or anisotropic magnetoresistance (AMR) which would arise in the Pt layer from an induced magnetic moment provided by a magnetic proximity effect arising from an exchange interaction at the Pt-$RuCl_3$ interface [13].

References:

[1]   Kitaev, A. Anyons in an exactly solved model and beyond. *Ann. Phys.* **321**, 2–111 (2006).

[2]   Banerjee, A. *et al*. Proximate Kitaev quantum spin liquid behavior in a honeycomb magnet. *Nat. Mater.* **15**, (2016).

[3]   Banerjee, A. *et al.* Excitations in the field-induced quantum spin liquid state of. *npj Quantum Mater.* **8**, (2018).

[4]   Kasahara, Y. *et al.* Majorana quantization and half-integer thermal quantum Hall effect in a Kitaev spin liquid. *Nature* **559**, 227–231 (2018).

[5]   He, M. *et al*. Uniaxial and Hydrostatic pressure effects in α-RuCl$_3$ single crystals via thermal-expansion measurements. J. Phys.: Condens. Matter. **30**, 385702 (2018).

[6]   Chen, Y. T. *et al.* Theory of spin Hall magnetoresistance. *Phys. Rev. B*. **87**, 144411 (2013).

[7]   Cao, H. B. *et al.* Low-temperature crystal and magnetic structure of α-RuCl$_3$. *Phys. Rev. B*. **93**, 134423 (2016).

[8]   Kubota, Y., Tanaka, H., Ono, T., Narumi, Y. & Kindo, K. Successive magnetic phase transitions in α-RuCl$_3$: XY-like frustrated magnet on the honeycomb lattice. *Phys. Rev. B*. **91**, 094422 (2015).

[9]   Ziatdinov, M. *et al.* Atomic-scale observation of structural and electronic orders in the layered compound α-RuCl$_3$. *Nat. Commun.* **7**, 13774 (2016).

[10]   Mashhadi, S. *et al.* Electrical Transport Signature of the Magnetic Fluctuation-Structure Relation in α-RuCl$_3$ Nanoflakes. *Nano Lett.* **18**, 3203–3208 (2018).

[11]   Lu, Y. M. *et al.* Pt Magnetic Polarization on Y$_3$Fe$_5$O$_{12}$ and Magnetotransport Characteristics. *Phys. Rev. Lett.* **110**, 147207 (2013).

[12]   Kondo, J. Resistance Minimum in Dilute Magnetic Alloys. *Progress of Theoretical Physics*, **32**, 1, (1964).

[13]   Huang, S. Y. *et al.* Transport magnetic proximity effects in platinum. *Phys. Rev. Lett.* **109**, 107204 (2012).

[14]   Lammel, M. *et al.* Spin Hall magnetoresistance in heterostructures consisting of noncrystalline paramagnetic YIG and Pt. *Appl. Phys. Lett.* **114**, 252402 (2019)